

Study of deformation-induced structures in a Zr-based bulk metallic glass via high energy x-ray diffraction

Von der Fakultät Maschinenwesen der Technischen Universität Dresden

zur Erlangung des akademischen Grades

Doktoringenieur (Dr.-Ing.)

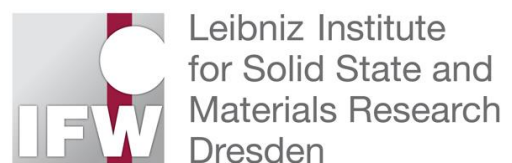
Vorgelegte

DISSERTATION

von

Hamed Shakur Shahabi

geboren am 07.04.1982 in Maragheh, Iran



Tag der Einreichung: 25. August 2015

Tag der Verteidigung: 26. Oktober 2015

1. Gutachter: Prof. Dr. J. Eckert

2. Gutachter: Prof. Dr. M. Zehetbauer

Contents

Abstract	3
Kuzfassung	6
1 Motivation and objectives	9
2 Theoretical background	12
2.1 Structure of metallic glasses.....	12
2.2 Mechanical properties and deformation behavior of metallic glasses.....	14
2.2.1 Deformation mechanisms.....	14
2.2.2 Shear banding.....	18
2.2.3 Temperature rise in shear bands.....	23
2.2.4 Strength and yield criterion.....	28
2.2.5 Parameters affecting plastic deformation in BMGs	31
2.3 Improving of plasticity of BMGs.....	36
2.3.1 Bulk metallic glass composites.....	36
2.3.2 Mechanical treatment.....	37
2.4 High energy x-ray characterization of deformed BMGs.....	39
2.4.1 Advantage of synchrotron over x-ray machines	39
2.4.2 Real and reciprocal space analysis of metallic glasses	40
2.4.3 Determination of strain from synchrotron data	41
2.4.4 Characterization of elastic response of BMGs.....	42
2.4.5 Length scale dependence of strain in metallic glasses	46
2.4.6 Short range order characterization.....	50
2.4.7 Characterization of medium range order and plastic response of BMGs.....	55
3 Experimental procedures	60
3.1 Sample preparation.....	60
3.1.1 Pre-alloy preparation	60
3.1.2 Arc melting.....	60
3.1.3 Centrifugal casting.....	60
3.2 Characterization	61
3.2.1 Scanning electron microscopy (SEM).....	61
3.2.2 Nanoindentation.....	61
3.2.3 Tensile test.....	62

3.3	High energy x-ray diffraction experiments.....	63
3.3.1	In-situ compression.....	63
3.3.2	Analysis of mechanically-imprinted structure	63
3.3.3	Single shear band analysis.....	64
3.4	Data processing	66
3.5	Calculation of strain tensor.....	67
3.6	Calculation of atomic packing density	68
4	Strain evolution during in-situ compression	69
4.1	Macroscopic stress-strain behavior.....	69
4.2	Short-range order characterization.....	69
4.3	Variation of atomic packing density.....	71
4.4	Atomic displacements during elasto-plastic deformation.....	72
4.4.1	Elastic deformation	73
4.4.2	Plastic deformation	74
4.4.3	Softening.....	77
4.5	Length scale dependence of atomic strains.....	78
4.6	Summary.....	79
5	Strain distribution in mechanically-imprinted BMG	80
5.1	Microstructural features	80
5.2	Effect of imprinting on tensile properties.....	81
5.3	Heterogeneous structure characterized by nanoindentation	82
5.4	Detection of heterogeneities via high energy x-ray diffraction	84
5.4.1	Strain tensor based on q_1 variations.....	86
5.5	Summary	89
6	Residual strain around a single shear band	91
6.1	Microstructure	91
6.2	Reciprocal space mapping.....	92
6.3	Residual strain at SRO and MRO	94
6.4	Summary	97
7	Conclusion and outlook	98
	Acknowledgement	101
	Bibliography.....	102

Abstract

This PhD thesis employed high energy synchrotron x-ray radiation to reveal atomic scale structural features occurring in plastically deformed $Zr_{52.5}Ti_5Cu_{18}Ni_{14.5}Al_{10}$ (Vit105) bulk metallic glass (BMG). The study is divided into three parts: Strain evolution during in-situ compression, strain distribution maps in mechanically-imprinted BMG, and residual strain around a single shear band.

1. Strain evolution during in-situ compression

The structural rearrangements occurring during compressive deformation of a plastically deformable BMG showed that the elastic and plastic deformation of the BMG is correlated to the structural changes at short- (SRO) and medium range order (MRO).

In the elastic regime, the atomic distances at SRO vary linearly with macroscopic stress. Analysis of the area under radial distribution function indicates that a small fraction of bonds in the first shell is broken in the loading direction whereas some new bonds are formed in the transverse direction. Atomic bonds at SRO appeared significantly stiffer than the MRO shells. Compared to the macroscopic values of the elastic strain, Young's modulus and Poisson's ratio, both SRO and MRO appeared significantly stiffer, implying that the elastic behavior of the BMG is not only ruled by simple compression of the atoms/clusters but also is aided by rearrangement of atoms/clusters.

The deviation of MRO atomic strain-stress correlation from linearity at the onset of plastic deformation was attributed to the activation of irreversible shear transformation zones. It was demonstrated by a strong shear strain value at the onset of yielding. This value is in good agreement with the reported value of the critical shear strain needed for activation of an irreversible STZ. The length scale of 12.5 Å indicated the largest shear strain and is probably the most effective length scale in the formation of STZs. The atomic pairs at SRO with smallest shear strain have the least contribution to the STZs. It was also indicated that the typical fracture

angle of this BMG can be explained by the orientation of maximum shear strain at the onset of catastrophic shear band formation.

2. Strain distribution map in mechanically-imprinted BMG

In mechanical imprinting, the BMG plate is loaded between two tools with a regular array of linear teeth and, as a result, a regular pattern of linear imprints is created on the surface of the plate. Mechanically imprinting results in considerable tensile plasticity of brittle Vit105 BMG plate. The distribution of hardness and Young's modulus values at the transverse cross section of imprinted plate probed via nanoindentation revealed oscillating soft and hard regions beneath the surface. Spatially-resolved strain maps obtained via high-energy nano-size beam X-ray diffraction exhibited that the plastic deformation during imprinting creates a spatially heterogeneous atomic arrangement, consisting of strong compressive and tensile strain fields as well as significant shear strain fields in the cross section. It was shown that the heat treatment diminishes the heterogeneous structure resulting in brittle behavior in tension. The analysis of strain tensor components based on changes in the first diffraction maximum of the structure function, q_1 , revealed that ϵ_x , the strain perpendicular to the loading direction, changes from the compressive at near to the surface to the tensile mode at the center of the imprinted plate. In contrast, the strain component along the loading direction, ϵ_y , changes from tensile near the surface to the compressive at the center. Beneath the surface, ϵ_x reaches to values about 1.5% under the imprints where there is a negligible ϵ_y . The distribution map of principal strains, ϵ_1 and ϵ_2 , indicated that large regions with compressive ϵ_1 and ϵ_2 exist under the imprints which can result in blocking of the propagating shear bands in agreement with microstructural observations of shear banding after uniaxial tension. Moreover, the region beneath the border of the imprinted and un-imprinted parts has the highest residual shear strain. Microstructural observations indicated that such regions can nucleate new shear bands upon tensile loading of imprinted BMG plate.

3. Residual strain around a single shear band

In order to probe structural changes in the shear-induced zone around a single shear band, the distribution of residual strains at short- and medium-range order around a

single shear band was determined in cold-rolled BMG plate using the nano-focused high energy x-ray diffraction. Plastic deformation results in significant residual normal and shear strains at distances of more than 15 μm around the shear band. The residual normal strains exhibit an asymmetric distribution whereas the residual shear strain is distributed symmetrically around the shear band. The large amount of residual atomic shear strain magnitude at the vicinity of the shear band triggers the nucleation of the new shear bands. The coincidence of the direction of the nucleating secondary shear bands from the main shear band with the orientation of the residual shear strain at the vicinity of the mature shear band highlight the dominant role of the shear strain in determining further plastic deformation at regions near the shear band.

Kuzfassung

Im Rahmen dieser Arbeit wird hochenergetische Synchrotron Röntgenstrahlung zum Aufzeigen der strukturellen Veränderungen in plastisch verformtem $Zr_{52.5}Ti_5Cu_{18}Ni_{14.5}Al_{10}$ metallischen Glas verwendet. Die Arbeit gliedert sich in drei Teile: Dehnungsentwicklung während in-situ Druckversuch, Dehnungsverteilung eines mechanisch geprägten massiven metallischen Glases, und Restdehnungen in der Umgebung eines einzelnen Scherbandes.

1. Dehnungsentwicklung während in-situ Druckversuch

Die während der Verformung auftretende strukturelle Neuordnung eines plastisch verformbaren metallischen Glases zeigt die Korrelation der elastischen und plastischen Verformung mit den strukturellen Änderungen in den Größenordnungen der Nah- (SRO) und mittelreichweitigen Ordnung (MRO).

Im elastischen Bereich verändern sich die Atomabstände in der SRO linear mit der makroskopisch anliegenden Spannung. Die Untersuchung der Fläche unter der Radialen Verteilungsfunktion (RDF) deutet auf ein Aufbrechen eines geringen Anteils der Bindungen der ersten Schale in Druckspannungsrichtung und deren Neubildung quer dazu. Die atomaren Bindungen in der SRO erscheinen wesentlich steifer als in den MRO Schalen. Vergleicht man die Werte von elastischer Dehnung, E-Modul und Querkontraktionszahl mit ihren makroskopischen Gegenstücken erscheinen beide, SRO und MRO, wesentlich steifer. Dies zeigt, dass die elastische Verformung von metallischen Gläsern nicht nur von der einfachen Stauchung der Atome bzw. Atomgruppen bestimmt, sondern auch durch deren Neuordnung unterstützt wird.

Das Abweichen der Dehnungs-Spannungs-Korrelation vom linearen Verhalten in der MRO am Beginn der plastischen Verformung wird der irreversiblen Bildung von Schertransformations-zonen (STZ) zugeschrieben. Dies zeigt sich zudem in den erhöhten Scherdehnungswerten am Beginn der Dehngrenze, welche mit den in der Literatur berichteten Werten für die kritische Scherdehnung zum Bilden einer STZ übereinstimmen. Bei einem Atomabstand von $12,5 \text{ \AA}$ tritt der höchste Wert der Scherdehnung auf und markiert den effektivsten Längenbereich der STZ Bildung.

Andererseits haben die atomaren Paare in der SRO mit der geringsten Scherdehnung den geringsten Beitrag an der STZ. Es zeigt sich außerdem, dass der typische Bruchwinkel dieses metallischen Glases über die Orientierung der maximalen Scherdehnung am Beginn der kritischen Scherbandbildung erklärt werden kann.

2. Dehnungsverteilung eines mechanisch geprägten massiven metallischen Glases

Eine Prägung besteht darin, eine Platte metallischen Glases mit zwei Stempel, auf denen eine regelmäßige Anordnung von geradlinigen Kerben angebracht ist, zu belasten. Dadurch wird eine ebenso regelmäßige Anordnung von geradlinigen Kerben auf der Oberfläche des metallischen Glases erzeugt. Die plastische Verformbarkeit der Vit105 Platte im Zugversuch wird durch Prägung im Vergleich zur gegossenen Probe eindeutig verbessert. Die Untersuchung der Härte und des E-Moduls über den Querschnitt der geprägten Probe zeigt die Einbringung von abwechselnd weichen und harten Regionen an der Oberfläche. Es wurden räumlich aufgelöste Dehnungskarten des geprägten metallischen Glases durch Beugung eines hochenergetischen nanometergroßen Röntgenstrahles erzeugt. Die Ergebnisse offenbaren, dass die durch Prägung eingebrachte plastische Verformung eine räumlich heterogene Atomanordnung erzeugt, welche aus starken Druck- und Zugdehnungsfeldern besteht. Zusätzlich wird eine signifikante Scherdehnung in die Probe eingebracht. Die Wärmebehandlung beseitigt diese heterogene Struktur und führt sie fast auf den Ausgangszustand zurück.

Die Analyse der Dehnungstensor-Komponenten basierend auf Änderungen im erstem Maximum des Strukturformfaktors, q_1 , zeigt, dass sich ϵ_x von der Oberfläche zur Mitte der Platte hin von einer Stauchung in eine Dehnung umwandelt. Im Gegensatz dazu wandelt sich die Komponente ϵ_y von der Oberfläche zur Mitte der Platte hin von einer Dehnung in eine Stauchung um. An der Oberfläche unter den Eindrücken, wo ϵ_y vernachlässigbar ist, erreicht ϵ_x Werte von ca. 1.5 %. Die Verteilungskarten der Hauptdehnungen zeigen, dass beide e_1 und e_2 unterhalb der Kerben als Stauchungen vorhanden sind. Daraus resultiert das Blockieren und Ablenken der sich ausbreitenden Scherbänder, was an Zugproben im REM beobachtet werden kann.

Weiterhin hat der Bereich an der Grenze der geprägten und nicht geprägten Regionen die höchste Restscherdehnung. Mikrostrukturelle Beobachtungen deuten darauf hin, dass solche Bereiche unter Zuglast Keimstellen für neue Scherbänder sind.

3. Restdehnungen in der Umgebung eines einzelnen Scherbandes

Es wurde ein einzelnes Scherband einer kaltgewalzte Platte mittels Beugung eines hochenergetischen nanometergroßen Röntgenstrahles untersucht. Die strukturellen Unterschiede in der scherinduzierten Zone um ein einzelnes Scherband werden durch die Verteilung der Restdehnungen in SRO und MRO bestimmt. Plastische Verformung führt zu signifikanten Restnormal- und Restscherdehnungen in Entfernungen von mehr als 15 μm um das Scherband. Die Restnormaldehnungen zeigen eine asymmetrische Verteilung, wohingegen die Restscherdehnungen auf beiden Seiten des Scherbandes symmetrisch verteilt sind. Der große Betrag der atomaren Restscherdehnung in der Nähe des Scherbandes führt zur Bildung von neuen Scherbändern. Das Zusammenfallen der Richtung des sich bildenden sekundären Scherbandes und der Orientierung der Restscherdehnung, in der Nähe des primären Scherbandes, demonstriert die dominierende Rolle der Scherdehnung bei weiterer plastischer Verformung in der Nähe des Scherbandes.

1 Motivation and objectives

Bulk metallic glasses (BMGs) are metastable alloys with a disordered liquid-like structure retained at room temperature. The absence of structural periodicity in their atomic arrangement leads to remarkable mechanical properties, including near-theoretical strength and an unusually large elastic limit, which makes BMGs of considerable interest for structural applications. Even though some BMGs show a small amount of plastic deformation, majority of them exhibit brittle fracture upon loading due to the lack of strain hardening mechanisms. The mostly accepted mechanism of room temperature plastic deformation in BMGs is the formation and propagation of localized shear bands nucleated from shear transformation zones (STZs). The lack of long range order also renders the detailed understanding of their deformation mechanisms a very challenging task because structural studies cannot rely on a regular crystal structure and on the dynamics of related defects, such as dislocations [1].

High energy synchrotron X-ray diffraction (XRD) is a very effective tool to disclose the details of the atomic structure of amorphous materials [2-4]. High photon energies have a high penetration power enabling investigation of bulk samples in transmission geometry and the high momentum transfer gives access to a large reciprocal space allowing studying of the pair distribution function (PDF). Moreover, the high brilliance of third generation synchrotron enables micro size focusing with high photon flux and low background [3, 4] which is ideal for precise structural characterization of BMGs during in situ mechanical tests [5, 6].

It is believed that the atomic scale events occurring upon elastic deformation of BMGs are reversible upon unloading and the average interatomic distances are not affected by room temperature plastic deformation since it proceeds via macroscopic events of shear banding [7, 8]. Consequently, the majority of the reported atomic scale analyses of BMGs using high energy XRD have been focused on the in-situ characterization of the elastic deformation. The first chapter of the results aimed to use high energy x-rays to characterize the variation of inter- atomic/cluster distances and rearrangements within both the elastic and plastic deformation of the

Zr-based BMG under uniaxial compression. The investigation tried to shed light on the evolution of shear strain and its role in plastic deformation of the BMG as well as to link the atomistic observations to the microstructural observations and the STZ theory.

When considering a network of intersecting shear bands in plastically deformed structure, it is believed that the whole monolithic structure turns into a heterogeneous array of sheared and un-deformed regions which can result in remarkable implications for the subsequent room temperature plastic deformation of BMGs [9-16]. The appearance of such heterogeneous structures in plastically deformed BMGs has been highlighted in terms of hardness gradients [15, 17-20], residual strain/stress domains [16, 21-27], and free volume variation [28, 29]. These studies have well succeeded to draw a macroscopic image of a heterogeneous structure in monolithic BMGs. However, high resolution analysis of atomic scale distances in such structures via sufficiently small probes is still missing. The second chapter of the results employs a nano-focused high energy x-ray to provide spatially-resolved strain maps of a mechanically-imprinted BMG in the MRO. The mechanism that these heterogeneities result in a tensile plasticity enhancement is also discussed in terms of the role of the strain fields.

The obtained spatial strain maps of the heterogeneous structure in mechanically-imprinted BMG indicated that the plastic deformation via macroscopic shear banding affects not only the inter-atomic/cluster distances in the sheared region, but also the virtually intact regions indicate altered atomic scale distances. This challenges the localized nature of the shear at shear bands. There have been a limited number of studies revealing the microscopic scale changes within or around the shear bands. Nanoindentation studies [30, 31] at directions perpendicular to a shear band have revealed a wide shear-induced region where the shear band has the lowest hardness and elastic modulus compared to the nearby regions. These studies had a spatial resolution of several microns and could not provide detailed knowledge on localized structural features like residual strains at the area around an individual shear band. In the frame of the third chapter of the results, high energy x-ray diffraction mapping of a single shear band formed by cold-rolling was

performed to reveal the variation of the SRO and MRO on a nanoscale resolution. For the first time, the fluctuations of the inter-atomic distances across and around a shear band established that plastic deformation results in a strong residual shear strain extending far beyond the localized region of shearing.

2 Theoretical background

2.1 Structure of metallic glasses

Glasses are obtained either by rapid solidification of their melts or by solid state amorphization processes like powder ball milling. To obtain an amorphous structure from the liquid, the melt temperature has to be reduced fast enough below the glass transition temperature, T_g , such that the liquid is frozen before the crystals can nucleate and grow. Metallic glasses are amorphous structures with at least one metallic element and which, compared to other materials, possess unique mechanical properties [32]. Since the discovery of the first metallic glass, $Au_{75}Si_{25}$, by Klement and coworkers [33], numerous metallic glass forming alloys including virtually all metallic elements in the periodic table have been discovered. The term “bulk metallic glasses”, so called BMGs, is attributed to those metallic glasses with good glass forming ability which can be cast into a fully amorphous structure with least 1 mm in the thinnest dimension [32]. Three empirical rule suggested by Inoue [34] indicate the minimum conditions required for glass formation:

- a) The alloy must have more than three elements.
- b) More than 12% difference in atomic size ratios among three main constituent elements.
- c) Negative heats of mixing among the three main constituent elements.

The atomic configuration and chemical bonding together determine the intrinsic properties of BMG materials. The structure of metallic glasses is closely related to the structure of the supercooled liquids. A pure crystalline metal undergoes a few percent of density change upon melting [32]. This indicates that atoms in liquid metals and, accordingly, in their frozen state, i.e., metallic glasses, have also dense packing. Such a kind of packing efficiency cannot be obtained by random distribution of atoms and needs certain degree of short/medium range order to fulfill topological and chemical requirements [32]. The pioneering work to understand the structure of monoatomic metallic glasses refers back to Bernal [35] who suggested a model of dense random packing of hard spheres (DRPHS). Based on this model, in order to fill the space using the same atomic type without having long

range translational order, the most efficient dense packing with the lowest level of energy is obtained by the icosahedral configuration where 12 atoms surround a central atom, as illustrated in Figure 2-1(a). Bernal's idea fits well with monatomic metals and alloys in which constituent species have comparable atomic sizes.

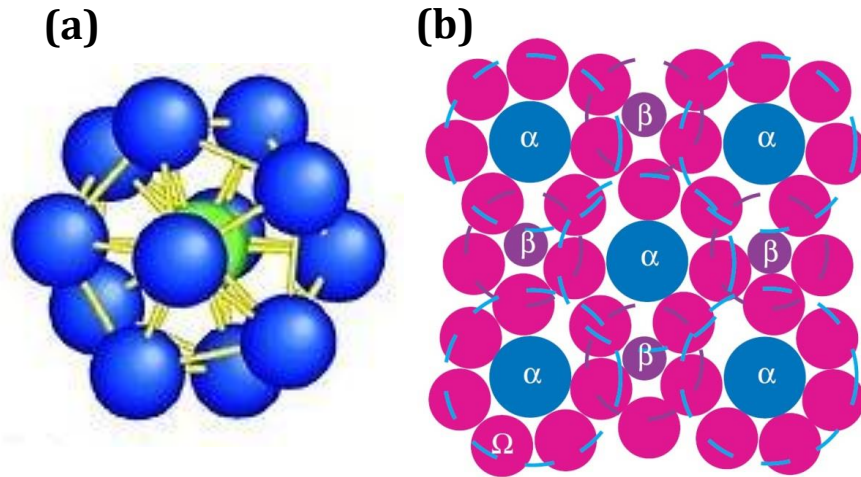


Figure 2-1 (a) Icosahedral configuration where 12 atoms surround a central atom [36], (b) A two-dimensional representation of a dense cluster-packing FCC structure in a (100) plane including solute(α)-centered icosahedral clusters with solvent (Ω) atoms in the first coordination shell and solute β atoms occupying octahedral interstices [37]

Trying to understand the atomic structure of multi component metallic glasses, where a significant difference exists between the atomic radius of elements, Miracle [38] has shown that efficient atomic packing in the nearest neighbor atoms is the fundamental aspect in the constitution of metallic glasses. Thus, structural unit of such complex glasses is based on solute-centered icosahedral clusters with solvent atoms in the first coordination shell according to Figure 2-1(b). In this assumption, an specific radius ratio, defined as the radius of the solute atom divided by the radius of the solvent atom, is energetically favored and forms the densest atomic packing [38]. This is in agreement with the empirical rule of Inoue requiring a minimum atomic radius difference of 12% for the stabilization of the supercooled liquid [34]. Miracle Confirmed proposed model with observed short range order (SRO) peaks in experimental partial radial distribution functions (RDF) and showed that the observed medium range order (MRO) of most of the metallic glasses is correlated to the solute atoms that occupy tetrahedral or octahedral interstices

between icosahedral clusters (such as β atoms in Figure 2-1(b)) [37, 39]. These icosahedral clusters form FCC or HCP unit cells as the densest possible structure [37, 39]. The order of the cluster-forming solutes is affected by internal strains due to packing frustrations and can only extend a few cluster diameters, and thus the disordered nature of the metallic glasses can be retained beyond the MRO range [37, 39]. The concept of icosahedral clustering and accompanying inter-cluster highly disordered areas has been supported by the nanoscale structural heterogeneities appeared as areas with varying stiffness in metallic glasses [40-43].

2.2 Mechanical properties and deformation behavior of metallic glasses

Mechanical properties of BMGs are far different from those of crystalline alloys. The presence of dislocations in crystals has been known as the reason for their low strength (compared to the theoretical value) and their plastic deformation behavior. Since metallic glasses are non-crystalline in nature and therefore do not contain any dislocations or grain boundaries, they are expected to exhibit high theoretical strength, but not ductility [44]. Indeed, when a BMG sample is subjected to a tensile test, it deforms elastically with a maximum elastic strain of about 2% and then experiences catastrophic fracture without appreciable plastic deformation [45, 46]. On the other hand, when a BMG sample is tested under compression, it may display catastrophic failure soon after the elastic limit [47] as well as significant plastic strain [48]. This implies an asymmetric response of BMGs under tension and compression opposed to the symmetric response of crystalline materials. Therefore, the mechanical response of metallic glasses and the corresponding deformation mechanisms are far away from what is known from crystalline materials and needs to be addressed in detail when we are to discuss the deformation-induced structures in metallic glasses.

2.2.1 Deformation mechanisms

Structural models proposed for the initiation of deformation in metallic glasses are summarized based on two main theories: a) free volume theory and b) shear transformation zone theory. They provide the atomic scale view of the deformation

mechanisms in metallic glasses, while the macroscopic mechanism for irreversible plastic deformation is based on initiation, propagation and intersection of shear bands which will be the subject of the next section.

Free volume model

Regardless of the atomic packing models, the total volume of a metallic glass can be separated into the space occupied by the dense atomic clusters and the empty space among these atomic clusters due to packing frustrations [49]. The term “Free volume” refers to the empty space and is defined as the fraction of matter having a lower atomic coordination than a reference region with a dense atomic packing [50-52]. In the free volume regions there is a weaker mechanical bonding than in the clusters and hence, local atomic rearrangements can result in a non-recoverable local relaxation. Thus, these sites may be the preferred regions for initiation of destabilization in the glassy structure induced by either heating or applied stress [49, 53, 54]. Gilman [55] and Spaepen [53] proposed that the plastic deformation of a metallic glass is coupled with the deformation-induced strain softening induced by mechanical dilatation. Shear deformation creates geometric defects with low packing density. This process is a function of the stress, temperature, and defect concentration and needs excess volume to be created. This means that displacement results in less perfect atomic packing with the creation of the free volume. This behavior is observed also in granular materials where the shear deformation of dense, randomly packed grains requires dilatation [53, 56]. Spaepen also used a single-atom model to describe how the free volume forms during squeezing an atom into a small empty space. He concluded that at ambient temperatures, where the decay rate of dilatation due to diffusion is small enough, the shear regions can keep a large component of shear-induced excess free volumes, which will ease further deformation, resulting in strain softening followed by strong shear localization [53]. More detailed behavior of free volume in metallic glasses was unveiled using positron annihilation spectroscopy [57-60]. Kanungo et al. [58] and Flores et al. [59, 60] studied deformed Cu-based and Zr-based metallic glasses and identified the distribution of sub-nanometer open-volume contents. They reported that as-quenched glasses have a high concentration of small open volumes, with a size comparable to the interstitial sites of dense atomic packing. On the other hand,

deformed samples have lower concentration of larger open volumes, named flow defects, created during plastic flow in the shear bands that coalesce to form larger nanovoids after additional deformation.

Despite the ability of the free volume model to explain deformation behavior of metallic glasses and some confirming experimental observations, this model has some deficiencies. It has been shown by computer simulations, creep tests and nanoindentation measurements that deformation of metallic glasses is necessarily related with the movement of group of atoms instead of single atom movement which is used by the free volume theory [1].

Shear Transformation Zones

Shear Transformation Zones, so called STZs, were introduced by Argon [54] in 1979. He defined an STZ as the fundamental unit of plasticity of metallic glasses considering of a small group of randomly close-packed atoms (about 5 atom diameters) that can reorganize spontaneously and cooperatively under an applied shear stress, which in turn create larger atomic displacement than in the surrounding matrix (see schematic in Figure 2-2) [49, 54]. Different from dislocations in crystals, STZs are not recognizable prior to loading as obvious defects with a different structure from the matrix. They are simply local groups of atoms that respond to specific level of applied load to produce shear strains [32]. To indicate detailed arrangement of STZs in metallic glasses, Argon and Kuo [61] made a connection to the Eshelby model. According to this model, when an inclusion is confined inside another linear elastic matrix with different elastic constant, the induced strain on the whole system can change the shape and size of the inclusion [62]. Using this model, Argon and Kuo proposed that STZs are confined and deformed as “inclusions” within an elastic matrix [61]. They also assessed the effect of elastic matrix confinement on the energy barrier between an initial and deformed STZ and argued that the elastic matrix confinement of an isolated transformed STZ causes reversible elastic energy storage in the STZ-matrix system, inferring that transformed STZs have a memory of their original untransformed state [63, 64]. A support for this scheme is the computer simulation of Li et al. [65] which showed

that the icosahedral clusters of Cu–Zr connect with each other, forming strings and networks which act as the elastic backbone of metallic glass under the loading [65].

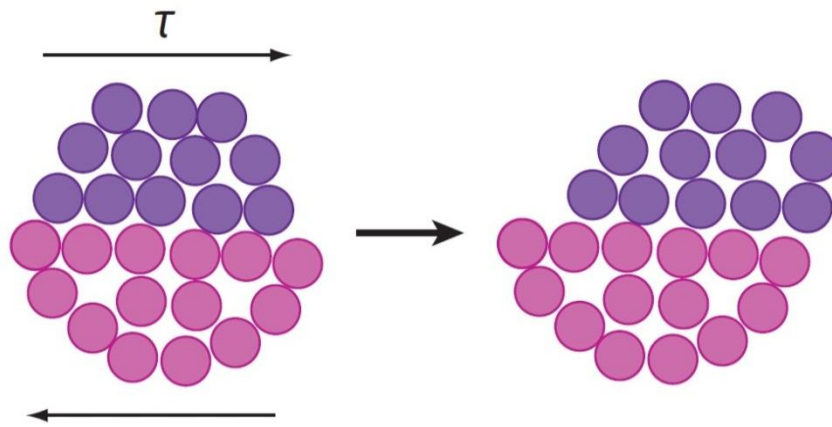


Figure 2-2 Schematics of the activation of an STZ under an induced shear stress [66]

The activation of the STZ-based deformation mechanism is necessarily connected to their nucleation in the amorphous structure upon loading. Recent studies suggest that STZs are more likely to be found in local regions with certain structural features, such as areas with more structural disorder [67], larger free volume [68], and under higher atomic-level stresses [69]. Based on reported nanoscale stiffness heterogeneities [40-43] Cheng et al. modeled the Cu–Zr–Al metallic glass system and reported that the icosahedral order corresponds to higher local stiffness and more stable regions while STZs nucleate from more disordered regions with lower stiffness and stability [70]. Once the shear stress is applied, the high elastic strain at the nucleating sites promotes the formation of thermally activated STZs. Similar to the free volume model, such shearing transformations can push apart the involved surrounding atoms resulting in dilatation and local strain softening [54]. Shimizu et al. [71] simulated the yielding of metallic glasses and indicated that processing imperfections in metallic glasses act as the stress concentrators. These may favor preferential nucleation of STZs under local high stresses, resulting in the creation of rejuvenated and softened regions.

The dynamics of deformation in amorphous structures through STZs was investigated via a model by Falk [72] and Langer [73]. They assumed that STZs undergo stress-driven transitions between two different states: jammed and flowing. By “jammed” state they mean those STZs that are not able to move anymore

in the direction that they have been already transformed and relieved a certain amount of induced shear stress. The attempt frequency of the transitions is tied to the strain rate driven random fluctuations of atoms. They defined these transitions by mean-field equations of motion for the number density of STZs and by the irreversible rearrangements of atoms in the STZs. The plastic flow occurs only when the rate of formation of new zones (“flowing” or “unjammed”) is as fast as existing transformed zones. This rate is strongly affected by the applied stress [72, 73].

Moreover, activation of potential STZs depends on their size. In 2005, based on theoretical analysis, Johnson and Samwer [74] reported that an STZ size of about 100 atoms has the minimum activation energy and yielding occurs when the applied stress turns a critical number of such STZs into an unstable state. Using molecular dynamics simulation, Mayr [75] injected energy into atomic clusters and monitored the activation of potential STZs under an external stress. He found that the minimum energy necessary to initiate observable plastic flow is about 0.35eV which is obtained when the activated size is about 140 atoms. This is consistent with the results of Zink et al. [76] who found out that the macroscopic shear deformation of amorphous CuTi, and presumably other metallic glasses is mediated by STZs of 15Å (about 120 atoms). Later in 2008, Pan et al [77] experimentally measured the STZs activation volume in six different BMGs by employing nanoindentation test at different loading rates. They reported that the ductility of BMGs is correlated with their STZ volumes and STZs with higher volumes promote the formation of multiple shear bands. Using the same method, Pan and coworkers studied the effect of structural relaxation on STZs size in a $Zr_{70}Ni_{16}Cu_6Al_8$ glassy alloy and observed that annealing results in atomic densification by the increase of the icosahedral short range order leading to the decrease of the STZ volume along with the degradation of ductility [78].

2.2.2 Shear banding

The deformation behavior of metallic glasses has been categorized as inhomogeneous and homogeneous. Homogeneous deformation occurs at high temperatures (higher than about $0.5T_g$ where T_g is the glass transition temperature) and low stresses. In this regime, metallic glasses undergo viscous flow in which

plastic strain is distributed continuously between different volume elements within the material. Therefore, each volume element of the specimen contributes to the deformation and prevents premature failure of the BMG under loading. Therefore, metallic glasses can display extraordinarily amount of plastic deformation in this regime. For example, a tensile elongation of 20,000% has been reported in a $\text{La}_{55}\text{Al}_{25}\text{Ni}_{20}$ alloy in the supercooled liquid region. The homogeneous flow of metallic glasses is of direct application-relevance in shape-forming operations as it is possible to achieve net-shape forming capability by working the metallic glass in this temperature regime [44, 79]. It has been observed that at high temperatures and low applied stresses, the flow is Newtonian; that is, strain rate is proportional to stress. However, with increasing applied stresses, the stress sensitivity of deformation drops rapidly and the flow is non-Newtonian [44].

Inhomogeneous deformation occurs at temperatures lower than about $0.5T_g$, and at high stresses and strain rates. Deformation is localized in a few very thin “shear bands” that form approximately on the planes of maximum resolved shear stress (i.e. close to 45° to the loading axis). The transition temperature between the inhomogeneous and homogeneous deformation can be thought of as a brittle-to-ductile transition, and is strongly dependent on the applied strain rate [44]. Inhomogeneous type of deformation in the metallic glasses is responsible for the mechanical instability at high stresses which results in catastrophic failure under loading [44]. In this regime, yielding and plasticity of metallic glasses at room temperature is controlled by the formation and propagation of shear bands and catastrophic failure of metallic glasses is mainly due to prompt propagation of a dominant shear band [1]. This indicates the significance of the shear banding phenomenon for the room temperature deformation of metallic glasses which has been the topic of very extensive research over the last decade [80-87]. In this context, a shear-band is defined as a form of plastic instability that localizes large shear strains in a relatively thin band [1]. To understand the mechanism of shear banding, one needs to correlate this phenomenon to structural models of deformation. Since the STZ model is widely accepted by many researchers [32, 49, 77], further discussions is based on this model.

Shear banding is correlated to the STZ theory using the Eshelby model that was introduced in the previous section. Yang et al. [88] pictured an STZ as a part carved out from a sheared matrix, and then put it back into the glassy matrix. The matrix has to elastically accommodate the changed shape of the STZ, resulting in an overall macroscopic strain of the sample [88]. When a metallic glass is sheared elastically, the local inelastic deformation of individual STZs is confined. The scattered STZs are supported by the elastic matrix. As long as these STZs have not reached a critical size, their deformation is reversible and by unloading, they will recover their initial form under the Eshelby back-stress from the elastic matrix [89]. Once the metallic glass is loaded plastically, the deformation mechanism is carried by shear bands. There are three scenarios for shear bands formation [1]:

(1) The plastic deformation of metallic glasses occurs when the deformation of a critical number of STZs turns from reversible in irreversible state. This occurs when the shear stress is large enough to activate a high number of unstable STZs that connect with each other along the plane of maximum shear stress. Then, they will form a critically unstable band which will penetrate into the elastic backbone and create irreversible macroscopic strain. Such a plastically deformed local regions become softer than the surrounding undeformed area due to dilatation. Once their size exceeds a critical value, the localized deformation will lead to instability in the form of a shear band [1, 32, 89]. This means that the shear banding occurs via cooperative slipping event of aggregated STZs with different length scales in different time scales [32].

(2) Another scenario, more realistic in the laboratory scale, was proposed by Shimitzu et al. [71]. They have employed molecular dynamics computer simulations to demonstrate that processing flaws of metallic glasses including voids and surface notches can act as local stress concentrating regions [1, 71]. Such highly stressed region creates an embryonic shear band by locally activating a group of STZs, and when the embryonic shear band reaches an estimated critical length of about 100 nm, it would propagate and develop into a mature shear band. Such propagation happens alongside a needle-like region as indicated in Figure 2-3. There exist four zones, so called "ARGL", representing aged glass (not sheared), rejuvenated glass,

glue and liquid (or near-liquid), respectively. The temperature increases from room temperature in aged glass region to above T_g in the liquid region. The temperature in the glue region is below T_g . The adhesive strength offered over the length of the glue zone provides the main resistance against shear band propagation. Such a model of propagation was partly confirmed by the experimental observation of Yang et al. [90, 91], who employed an infrared camera to monitor the temperature profile during compression of a pre-notched sample. They observed higher temperatures at the initiation point of the shear band. However, these experimental results correspond only to the very early stages of shear-band initiation and are not able to confirm the entire process of propagating a mature shear band.

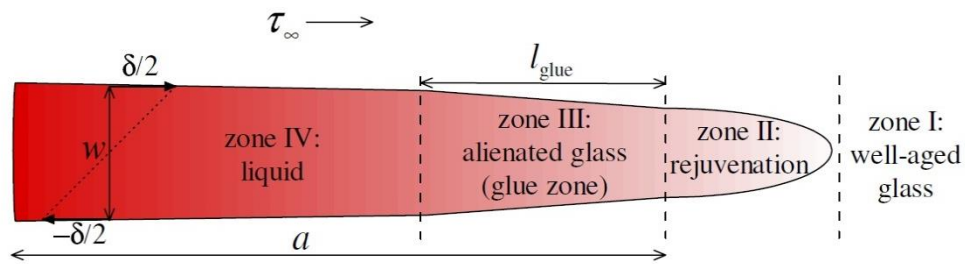


Figure 2-3 Aged-rejuvenation-glue-liquid (ARGL) model of shear band in BMGs. The shading represents temperature [71]

(3) The third scenario covers more aspects of shear band formation and is in good agreement with the experimental observations. It has two consecutive stages [92]. In the first stage, a band with a disordered structure is created by activation of STZs. The band is locally softened and includes mobilized atoms. Similar to the first scenario, STZs propagate heterogeneously from stress concentrators and form a band which crosses the sample. However, the band remains cold and there is no considerable temperature increase along it. The rejuvenating front propagates in the form of a shear wave at a speed of sound and leaves a very limited total shear offset in the sample [93]. The second stage is the simultaneous sliding and shear-off along the rejuvenated plane. With increasing shear offset, the shear band experiences large plastic strains resulting in significant local heating and thickening of the shear band. In Figure 2-4 schematics of such two-stage scenario have been depicted.

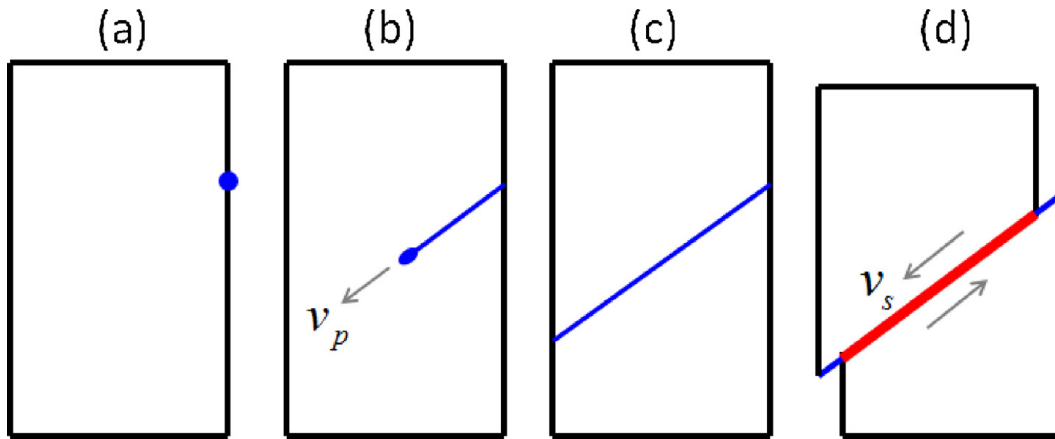


Figure 2-4 Schematics of a shear band formation in a metallic glass under compression; (a) A stress concentrator causes higher local stress, (b) Structural disordering (rejuvenation) propagates at shear-wave speed, (c) Reaching the other end of the sample, the propagating front leaves a rejuvenated plane with small strain and cold temperature, (d) Cooperative shearing/sliding and growth of the shear offset on both ends with much slower velocity [1]

This scenario has been confirmed by the computer simulations of Cao et al. [94], where they have indicated that the rejuvenating front propagates with a speed of about the sound velocity from the corner of the sample to create a path with disordered structure and negligible local heating. This is then followed by slow propagation of shear band in the second stage which is accompanied by the decrease of the fraction of icosahedra inside the shear band. The broken icosahedra in the shear band are transformed into more unstable, fragmented clusters [94]. The destruction of the short range order into a more disordered structure inside the shear bands was also verified by preferential etching of deformed metallic glasses which is an indicator of difference of the chemical potential of the material within the bands with respect to the undeformed bulk [95-97]. Such an altered structure inside the shear bands has lower flow stress which favors further deformation within the shear bands [98].

With respect to the first and second scenarios of shear band formation, the third two-stage scenario is in better agreement with the experimental observations. Packard and Schuh [99] observed that a shear band does not initiate from locations with the highest local shear stress, but forms only when the minimum stress along

an entire plane exceeds a critical value [1]. In agreement with this observation, Song et al. [100] used high-speed camera photography during several compression tests and demonstrated that the shear offsets at the two ends of a shear band proceeds simultaneously. Additional evidence of this scenario was provided by scanning electron microscopy (SEM) observations of the fracture surface by Han and Li [101]. They observed a smooth region on both ends of the fracture surface corresponding to the shear offsets developed in the cold early stage of sliding followed by vein patterns created by material melting due to temperature rise in the hot second stage of shear propagation [101].

Finally, it is worth mentioning that the localized softening in shear bands is reflected in mechanical tests as “serration” behavior. Each serration is a relaxation event associated with the formation of a shear band, reflected as a load drop in displacement-controlled load–displacement curves of compression test, or as a displacement burst at load-controlled nanoindentation experiments. When the shear band forms and propagates, the surrounding material recovers elastically and arrests the shear-band propagation. This is reflected as a sudden rise of the load. In general, lower deformation rates promote more obvious flow serration. At low rates a single shear band may operate to swiftly accommodate applied strain while at high deformation rates, a single shear band apparently cannot keep up with the applied strain and the formation of multiple shear bands with smaller shear offset is not observed in load-displacement curves [44, 79].

2.2.3 Temperature rise in shear bands

Compared to crystalline materials, metallic glasses have up to 30% of lower values of Young’s modulus and much higher values of elastic strain limit. This means that the amount of stored elastic energy per unit volume will be considerably higher than other crystalline materials. With starting of the yielding, one can expect that this stored energy has to be dissipated mainly in the shear band and result in significant heating [1]. This is proved by the observation of sparking at the moment of fracture of many metallic glasses as well as by the observation of liquid droplets in their fracture surface [102-104]. Nano-crystals detected in or around shear bands are also other indications of heating during shear [105-107]. The knowledge of temperature

rise in shear bands is significant due to its importance for the analysis of the temperature dependence of mechanical properties [108] or for the control of shear-banding in order to improve the mechanical properties [109]. Since the thickness of a shear band is very small compared to the bulk of sample and the whole process of shear banding occurs in a very short time-scale, the direct probing of temperature inside a shear band is virtually impossible. Therefore, most of the experiments have focused on the measurement and analysis of the temperature profile in the area around the shear band which is presumably affected by dissipated heat generated in the shear band. However, there is a significant discrepancy in the reported temperatures rise of the shear band area, varying from less than 0.1 K to a few thousand kelvin [44, 103, 110-115]. In this context, infra-red (IR) tomography was used to monitor the heat affected zone in a range of about 0.15 mm around a shear band during loading. The investigation indicated a negligible increase of temperature (0.4 K) which can be attributed to the poor spatial resolution of the method [115, 116]. A smart way with a much better resolution of temperature probing was conducted by Lewandowski and Greer [81] who coated notched bending samples of a Zr-based BMG (Vitreloy1) with a thin layer of tin and detected molten tin particles around the shear band offsets after deformation, signifying that the temperature has exceeded 232 °C, the melting point of Tin. They argued that for a shear band with a given heat content H , the temperature in the center of the shear band at the end of shear is given by [81]:

$$\Delta T_{center} = (H/\rho C \sqrt{\pi \alpha})(1/\sqrt{\delta t}) \quad \text{Equation 2-1}$$

where δt represents the shear duration at the relative velocity V resulting in a shear offset of $y = V\delta t$. The maximum value of V is $0.9c_t$ where $c_t \approx 2.47 \times 10^3 \text{ ms}^{-1}$ is the speed of a transverse sound wave. Taking this maximum V with $y = 0.5\text{--}2.6 \text{ }\mu\text{m}$, results in an estimate of $\delta t = 0.2\text{--}1.2 \text{ ns}$. ρ is the density of the BMG, C is the specific heat and α is the thermal diffusivity. Substituting the values for the Vitreloy 1 metallic glass from literature and experiments, they obtained a temperature increase of 3100–8300 K. They also reported that the thermal diffusion length calculated from this equation is 100-240 nm which is much broader than the reported shear band thickness of 10-20 nm [117]. This indicates that shear banding

is not an adiabatic process and the temperature rise does not control the thickness of the shear band [81]. The same method of temperature measurement was used later by Zhang et al. on three different BMGs with different base element [118].

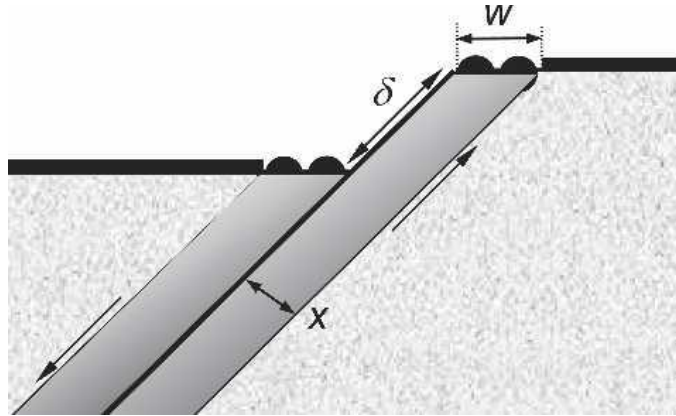


Figure 2-5 Schematic of a cross section through a metallic glass coated with a fusible layer (black) [118].

For a given glass, the half-width, x (see Figure 2-5), of the hot zone around a shear band (within which a given temperature, such as the melting temperature of the coating, is exceeded) is linearly proportional to the shear offset on the band. When different metallic glasses are compared, the half-width for a given shear offset, appears to be linearly proportional to the materials parameter, $\sigma_y/\rho C$, where σ_y , ρ and C are macroscopic uniaxial yield stress, density, and specific heat capacity of the metallic glass, respectively. For a given shear offset, local heating is more easily detected in glasses with higher $\sigma_y/\rho C$. The minimum shear offsets necessary to observe local melting in a fusible coating was also calculated and is in the order of a few hundred nanometers [118].

The shear band velocity is a significant parameter for the estimation of the local heating during shear band propagation. According to Eq. 2-1, higher shear band velocity results in increased predicted maximum temperature because the produced heat is dissipated from the shear band in shorter times [119]. The above mentioned studies take a shear band speed (velocity of one side of a band relative to the other side) of 0.9 of the sound velocity (corresponding to shear duration of 0.2–1.2 ns) for the calculation of maximum temperature in shear bands. Miracle et al. indicated that the maximum possible shear velocity is only $\sim 10\%$ of the velocity of transverse

sound wave and the actual shear velocity must be at least 50% of this value to observe molten tin in the shear offset region [120]. A similar result was reported by Georgarakis et al., who calculated the time for stress redistribution in a Zr-based metallic glass sample under compression test. The calculated shear time was of the order of 10 ns for a shear offset of one micron and they argued that assuming a shear speed of the order of sound velocity would result in unrealistic values of the temperature rise [121]. Wright et al. used four strain gauges during quasi static compression test of Pd₄₀Ni₄₀P₂₀ BMG and measured elapsed time during shear band propagation. They proposed two scenarios for shear banding; if shear happens along the entire length of the shear band simultaneously, the relative displacement rate of material on either side of the shear band is approximately 0.002 ms⁻¹. Alternatively, if the shear displacement occurs in a localized front that propagates across the specimen, the shear band velocity is approximately 2.8 ms⁻¹. Temperature estimation based on these velocities predicts maximum temperature increases of only 65 K in a shear band during serrated flow while predicts sufficient temperature increase for melting of the glass in the case catastrophic failure by major shear band [119].

Considering such a controversy in determining the temperature rise in shear bands, Cheng et al. [93] studied the dynamics of shear banding in uniaxial compression test. By using continuum-mechanics modeling they suggested that the shear offset in one serration is given by:

$$\Delta x = (2\Delta\sigma/E) \cdot L (1 + S) \quad \text{Equation 2-2}$$

where $\Delta\sigma$ represents the difference between the stress required to initiate yielding and the stress needed to maintain the running shear band. E is the Young's modulus, L is the sample height and S ($=k_s/k_M$) is the ratio of the sample stiffness to machine stiffness. The parameter $L(1+S)$ is introduced as an instability index and is important in determining the effect of the test conditions on shear banding. With a small instability index, heating is negligible and typical "arrest and go" behavior is seen in the loading curve. In contrast, with larger $L(1+S)$, obtained for example with bigger samples (as it is indicated in Figure 2-6) or a less stiff machine, there is considerable heating in the shear band and stable serrated flow is prevented by

thermal runaway of the major shear band [93]. Miracle et al. have reported for several BMGs that the division between these two regimes (negligible versus significant heating) for bending of a plate occurs at shear offset of 1 micron in a plate with thickness of 100 micron[120]. Cheng et al. in 2009 derived a critical value of instability index, λ_{crit} , for a given glass and sample aspect ratio based on the experiments reported in the literature. This critical instability index divides the regimes of cold (stick-slip) and hot (runaway) shear bands (Figure 2-7) according to sample size and machine stiffness [93].

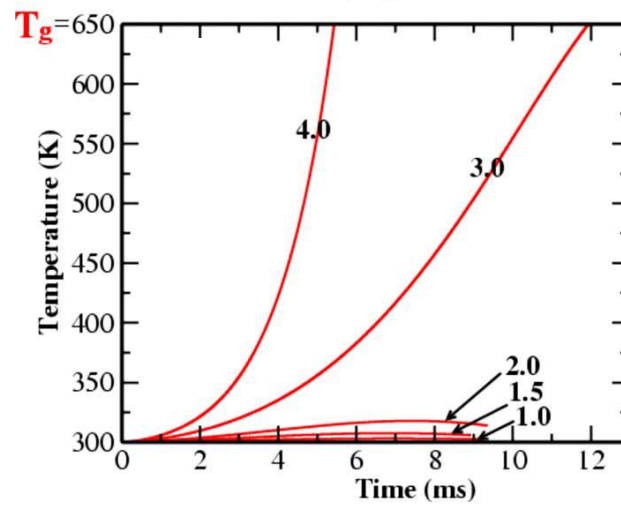


Figure 2-6 Modeling of size dependence of temperature profile versus elapsed shearing duration in a shear band obtained for different sample lengths [93]

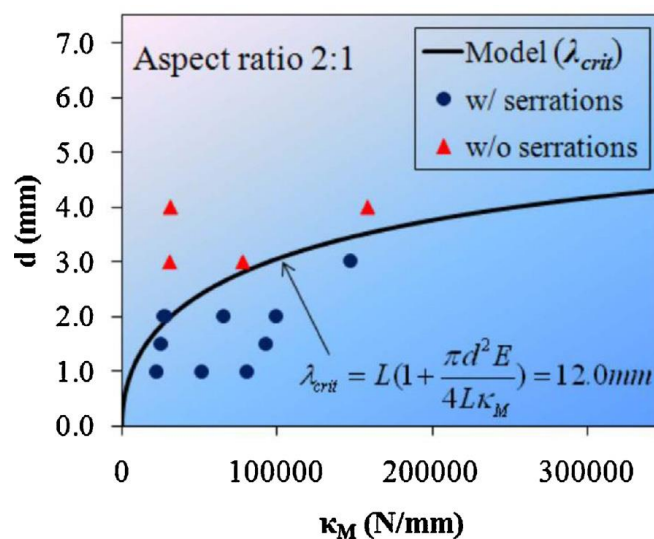


Figure 2-7 The Predicted λ_{crit} separates stick slip regime from runaway instability [93]

2.2.4 Strength and yield criterion

Metallic glasses possess very high strength and hardness at temperatures far less than their glass transition temperature. Their strength exceeds 1 GPa for most of BMGs, reaching values of up to about 5 GPa in Fe-based BMGs [44]. Johnson and Samwer [74] have investigated the room temperature elastic constants and compressive yield strengths of about 30 different metallic glasses and revealed that plastic yielding of metallic glasses at room temperature can be roughly described by an average elastic shear limit criterion:

$$\tau_c = \gamma_c \cdot G \quad \text{Equation 2-3}$$

where γ_c , critical shear strain, is 0.0267 ± 0.0020 , and G is the shear modulus. Their closer analysis, inspired by the cooperative shear model of Frenkel [122], indicated that the γ_c values for individual glasses are correlated with dimensionless temperature T_r/T_g where T_r is the room temperature and T_g is the glass transition temperature. In addition, γ_c for a single glass follows the same correlation (vs T/T_g) according to following equation:

$$\gamma_c = \gamma_{c0} - \gamma_{c1} \cdot (T/T_g)^{2/3} \quad \text{Equation 2-4}$$

where $\gamma_{c0} = 0.036 \pm 0.002$ and $\gamma_{c1} = 0.016 \pm 0.02$ [74]. Yang et al. [123] also evaluated the room temperature strength of 27 metallic glasses from 11 different alloy systems from the “free volume” point of view and linked the strength values to the glass transition temperature and molar volume. They found out that the yield strength values can be predicted by a unified parameter as:

$$\sigma_y = 50 (T_g - T_0)/V \quad \text{Equation 2-5}$$

where σ_y is the yield strength, T_g is the glass transition temperature, T_0 is the ambient temperature and V is the molar volume [123].

Metallic glasses display different yield strengths in compression and tension, the so called strength asymmetry [124]. Correspondingly, the fracture angles of BMG specimens under uniaxial tension and compression are different: The tensile fracture angle is about 56° , whereas under compression BMGs break at angles of 42° –

43° with the loading axis [45, 103, 125, 126]. This asymmetry of fracture properties suggests that the yield criterion of metallic glasses is different from traditional yield criteria of polycrystalline materials, which predict symmetric yield strength and fracture angles. In addition, the features in the fracture surface of BMGs indicates radiating vein-like patterns with round cores for tension, which are attributed to the effect of normal stress on the shear plane [127]. Donovan [114] suggested that yielding of metallic glasses follows the Mohr-Coulomb criterion instead of the Tresca or Von-Mises criteria. He proved that the sign of the normal stress acting across the slip-plane has a significant effect on the yield strength. Therefore, the yield strength in compression is substantially higher than in tension. According to the Mohr-Coulomb criterion for uniaxial tension [114, 127]:

$$\tau = \tau_0 - \mu \cdot \sigma \quad \text{Equation 2-6}$$

where τ_0 is the critical shear fracture stress, and μ is the coefficient reflecting the effect of the normal stress. This equation has been depicted in Figure 2-8 as a dashed red line. The Mohr circle (shaded in green) indicates the state of the stress for uniaxial tensile loading. The point at which the M-C line is tangent to the Mohr circle is the yield point of BMG.

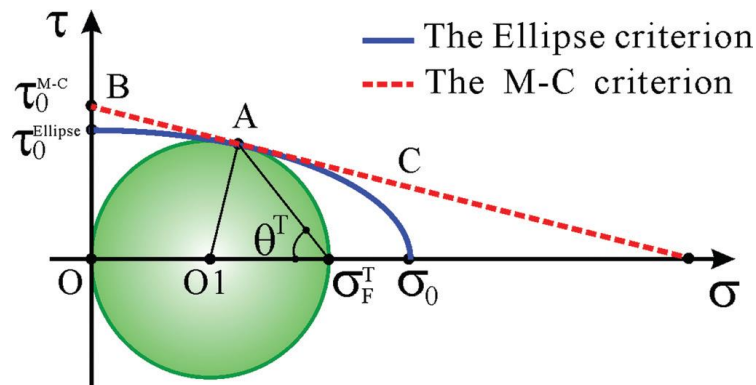


Figure 2-8 Mohr- Coulomb and Ellipse yield criterion of metallic glass with uniaxial tensile Mohr circle [127]

The parameters τ_0 and μ can be calculated from the measured fracture stress and the shear fracture angle under uniaxial tension [124].

Despite that the M-C criterion is in good agreement with many of the available experimental data on fracture of metallic glasses, it cannot explain why a BMG specimen fails sometimes along a plane perpendicular to the stress axis, i.e., $\theta_T=90$ [128]. That was the motivation for Zhang and Eckert [128] to collect fracture data of variety of metallic glasses to introduce a unified yield criterion, the Ellipse criterion, which can also interpret the perpendicular fracture of metallic glasses under uniaxial tension. They consider that the ratio $\alpha= \tau_0/\sigma_0$ in metallic glasses reflects the effect of the normal stress on the shear fracture, which varies in the range 0.384–0.625. At the atomic scale, it reflects the difference in the bonding property between atoms of different materials that, in turn, controls the macro scale fracture modes of the materials [128]. Then, the Ellipse criterion is defined as:

$$\sigma^2/\sigma_0^2 + \tau^2/\tau_0^2 \geq 1 \quad \text{Equation 2-7}$$

illustrated as a blue line in Figure 2-8. The ratio α can be also obtained from the value of the fracture angle as:

$$\alpha = \sqrt{\frac{1}{2}(1 - \cot^2 \theta_T)} \quad \text{Equation 2-8}$$

The Ellipse criterion is capable to describe all the different contributions of normal stress on the tensile fracture of a large number of compositionally different metallic glasses. However, the Ellipse criterion only interprets the cases of tensile stress states and lacks to fit to compression fracture data. To solve this, Qu and Zhang [129] modified the Ellipse criterion and suggested a new form as follows:

$$\tau^2 + \alpha^2 \beta \sigma^2 = \tau_0^2 \quad \text{Equation 2-9}$$

where the new parameter β describes the differences between the effects of tensile and compressive normal stresses. As illustrated in Figure 2-9, the new criterion is able to predict the yielding of metallic glasses in tension, pure shear and compression. At room temperature and under tensile quasi-static strain rate ($\beta=1$), the above equation turns to the Ellipse criterion. For compressive loading, the parameter β can be derived from the fracture angles in compression and tension as follows:

$$\beta_c = \frac{1 - \cot^2 \theta_c}{1 - \cot^2 \theta_T}$$

Equation 2-10

For different metallic glasses α changes with composition while β is constant at $\beta_c = -0.5$. In a microscopic view, similar values of β_c for different metallic glasses may reflect the similar atomic mechanism of cooperative shearing of STZs for shearing plastic flow. The normal stress acting on the shear plane of STZ influences the behavior of the individual STZ and eventually affects the yield and fracture behavior of BMGs [129].

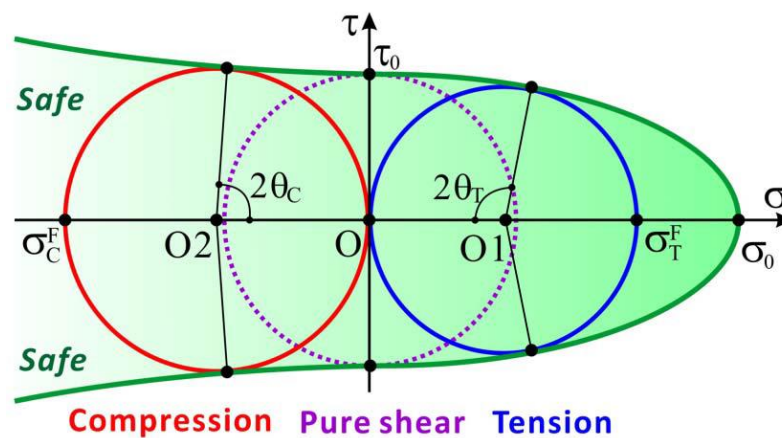


Figure 2-9 Modified Ellipse yield criterion of metallic glasses for compression, pure shear and tension [129]

2.2.5 Parameters affecting plastic deformation in BMGs

The limited plastic deformation is one of the major drawbacks of metallic glasses. There has been extensive research in the last years to explore intrinsic and extrinsic parameters that might affect the deformation ability of BMGs. In this section, the most important parameters that control plastic deformation are reviewed.

2.2.5.1 Sample shape

The aspect ratio (ratio of sample height to its diameter) of metallic glass samples can affect the shear banding behavior and consequently the plastic deformation of metallic glasses. For standard compression tests, an aspect ratio of 2 is usually chosen. For smaller aspect ratios, the interfaces between the sample and cross-heads will confine many of the propagating shear bands, preventing their catastrophic shear. Additionally, lateral frictional forces at these interfaces confine

the specimen more effectively and, consequently, multiple shear banding of metallic glass may occur easier, leading to larger total plastic deformation [130]. A study reported by Wu et al. also indicated that a BMG compression sample with tilted angle in one end becomes more plastic due to multiple shear bands concentrated at the two corners in closest contact with the cross-head [131].

2.2.5.2 Testing method

In order to characterize the mechanical properties of metallic glasses, different methods can be used. While shear banding is strongly affected by stress fields in the amorphous structure, different testing methods create different stress fields and consequently a different shear banding behavior is observed depending on the applied method [1]. In addition to strength and fracture angle asymmetry, BMGs appear to be asymmetric in terms of plasticity. While most of them are extremely brittle under tensile loading, they show limited plasticity under compression due to the confined conditions of the test [124]. In addition, when subjected to multiaxial or complicated stress field, BMGs exhibit higher strength and enhanced plasticity which originate from the suppression of the catastrophic shear-banding, and from the promotion of multiple shear banding. For example, improved plasticity under complex modes of confined stress has been reported for brittle BMGs subjected to bending [132-134], indentation [99, 135, 136] and rolling [12, 137, 138].

2.2.5.3 Effective machine stiffness

The stiffness of the testing machine, including machine and frame, can influence the observed plasticity of metallic glasses. A machine with low stiffness can store a high amount of elastic energy. During a uniaxial compression test, due to strain softening within the initial shear bands, this elastic energy can be released in a spring back way in the compression direction and can result in catastrophic shear failure without significant plasticity. Murata et al. designed a tensile testing machine made from stainless steel with high effective stiffness. With this device they reported promoted elongation and the successful prevention of the catastrophic failure of metallic glasses [139]. Later on, Han et al. developed a model which considers testing machine, frame and sample as behaving like a spring. Using elastic energy

balance they indicated that the plasticity of the BMG sample can be improved through increasing the stiffness of the machine or frame [140].

2.2.5.4 Sample size

As already discussed using Eq. 2-2, the smaller height of the sample reflected in the instability index leads to the smaller shear offsets which favors the “arrest and go” behavior instead of the catastrophic failure related to the uncontrolled propagation of the major shear band. Moreover, as illustrated in Figure 2-6, in larger samples, the temperature in shear band tends to be much higher. In the case of a bent plate, the spacing between shear bands is proportional to the plate thickness and the shear offset on each band scales with the square of the thickness. Therefore, increasing of sample size localizes the flow more effectively. This is coupled with more heating at shear bands, causing the sample to fail catastrophically [120]. Han et al. [141] proved that with a constant machine stiffness value, the observed compressive plasticity of BMG is increased with decreasing the size of the samples (Figure 2-10).

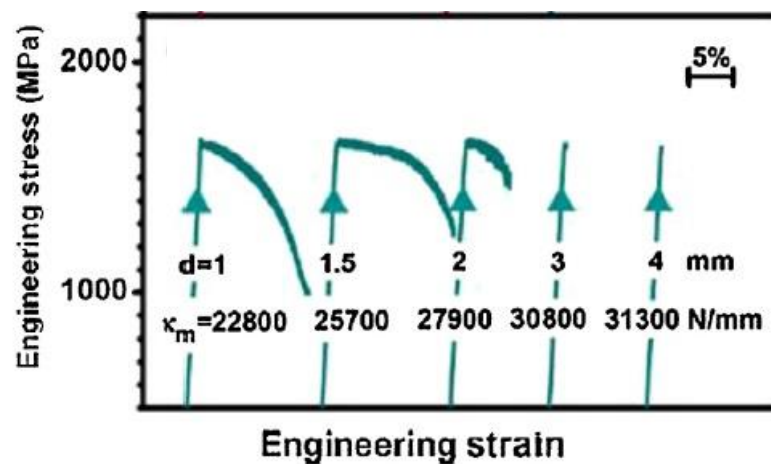


Figure 2-10 Increasing the height of BMG sample deteriorates the plastic deformation ability (in an almost constant machine stiffness value) [141]

It has also been shown that sub-micrometer samples exhibit some degrees of distributed (not localized) plastic strain. In nanoscale samples where stress concentrators (like casting flaws or stress fields) are minimized, the homogeneous nucleation of shear bands from structural fluctuations becomes important and more difficult with decreasing sample size. The required stress can increase towards the ideal strength, promoting homogeneous plastic deformation in the form of

distributed STZs [1]. In this context, Shan et al. [142] proposed the following scaling relationship between the sample size and the distributed plastic strain:

$$\varepsilon_p \propto (L/L_0)^{-3/A} \quad \text{Equation 2-11}$$

where L denotes the sample length-scale, L_0 is the length-scale of an STZ, and A is the critical number of STZs for percolation, above which a shear band forms [142].

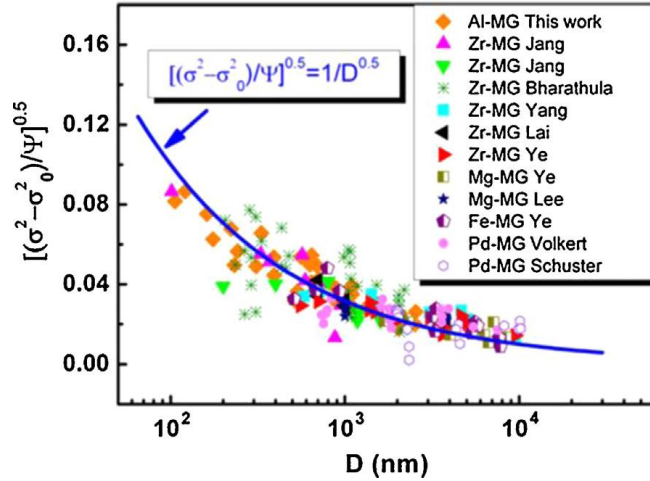


Figure 2-11 Size dependance of strength of BMGs with size in the micro- and nanoscale [143]

In addition to plastic deformation, the strength of BMGs is also sample size dependent. After extensive studies on the size dependence of the mechanical properties of BMGs, it is now widely accepted that “smaller is stronger”. Wang et al. [143] summarized recent experimental results on metallic glasses with size in the micrometer and sub-micrometer length scales (Figure 2-11) and observed that the strength of metallic glasses increases with decreasing the size from micrometer to sub-micrometer scale. They deduced the following equation for the size dependence of the strength of metallic glasses:

$$[(\sigma^2 - \sigma_0^2) \cdot r_a / 2\sqrt{2}E \cdot U]^{0.5} = 1/D^{0.5} \quad \text{Equation 2-12}$$

where σ is the stress needed to initiate the shear band, σ_0 is the stress needed to maintain the shear-band sliding, D is the sample diameter, E is the Young’s modulus,

U is the energy per area needed to create a shear band, and r_a is the aspect ratio [143].

2.2.5.5 Poisson ratio

In 1975 Chen et al. [144] noted that “it is the high Poisson’s ratio which is responsible for the ductile behavior of many metallic glasses.”. For polycrystalline materials, it has been shown by Pugh [145] that the resistance to plastic shear is proportional to the shear modulus μ , and that the resistance to dilation and cracking is proportional to the bulk modulus B. Therefore, small values of μ/B favor plastic flow. The Poisson’s ratio ν shows inverse proportionality with μ/B , such that reduced μ/B will raise ν towards its upper limit of 0.5 [145]. Schroers and Johnson showed that a Pt-based metallic glass with a very high ν of 0.42 plastically deforms in compression up to 20% strain and has very high fracture toughness (80 MPa $m^{1/2}$). They argued that the high Poisson ratio causes the tip of a shear band to extend rather than to initiate a crack [48]. According to the analysis of Conner et al. [132] and Wei et al. [146] for a bent plate with a given ratio of plate thickness to radius of curvature, the shear-band spacing and shear offset depend on the Poisson ratio.

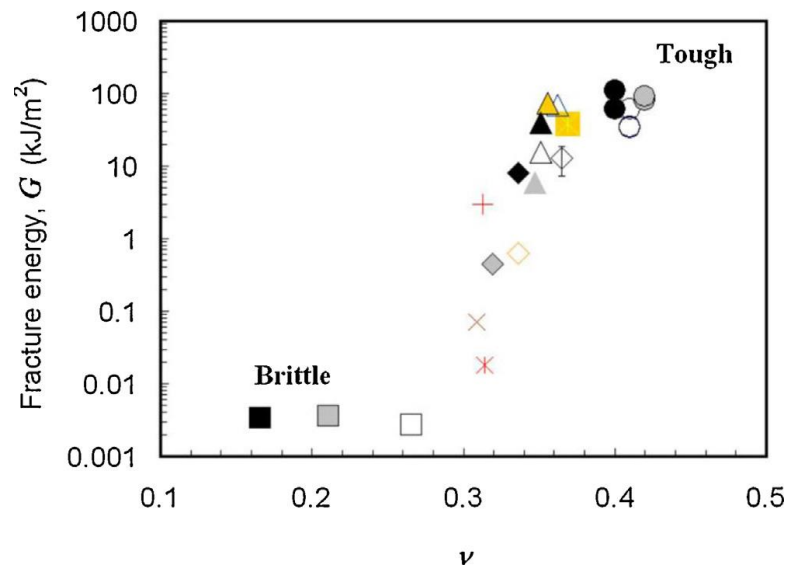


Figure 2-12 Fracture energy of metallic glasses increases with increasing of Poisson ratio dividing metallic glasses into two regimes of brittle and ductile [147]

Lewandowski et al. collected the data of several metallic glasses and provided a graph (Figure 2-12) indicating that the fracture energy of metallic glasses increases with increasing of the Poisson ratio. This divides metallic glasses into two categories of brittle and ductile with a critical value of Poisson's ratio at 0.31–0.32 [147]. Zhang and Greer remarked that the elastic properties of metallic glasses can be estimated from the properties of the constituent metallic elements using the rule-of-mixture. This means that in order to have higher plasticity and toughness, one has to choose compositions that have higher contents of elements with high ν [148].

2.3 Improving of plasticity of BMGs

The limited macroscopic plastic deformability of BMGs originates from the highly localized strain within the shear bands. This hinders the ability of using different kinds of forming techniques for making desired shapes out of BMGs [81]. Within the past decade, this issue has been the motivation for many researchers to develop techniques to improve the plasticity of these materials. In this section, the different approaches to enhance the plastic deformation of metallic glasses are reviewed with particular focus on the developed mechanical methods.

2.3.1 Bulk metallic glass composites

A main progressing area of enhancing plasticity of metallic glasses have been the development of BMG-composites, where a second phase of different length scale (from millimeter- to nano-sized phases) is incorporated in the amorphous matrix [149-158].

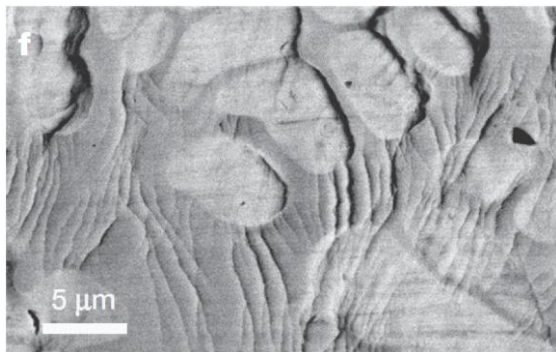


Figure 2-13 Propagating shear bands in a BMG composite are blocked at the interface with the second phase [149]

The principal mechanism that leads to multiple shear banding in BMG-composites is based on the hindrance or blockage of the propagating shear by the second phase

(Figure 2-13). This causes the activation of new shear bands and consequently higher amount of global plasticity [149]. There are two main categories of BMG composites based on the method of production: in-situ and ex-situ composites. The ex-situ composites can be produced by sintering of powder mixtures consisting of glassy powders and second-phase particles. They can also be prepared by the introduction of second phase(s) (in the form of particle or fibers reinforcements) into the glass-forming melt during processing. The in-situ BMG composites are formed either from their melts during appropriate solidification processing or by a secondary treatment of the amorphous structure (e.g. partial crystallization) [46].

2.3.2 Mechanical treatment

Besides a wide range of published works on developing composite BMGs, another set of techniques to attain enhanced room temperature plastic deformation, which can be categorized as mechanical treatment, have been reported in the recent years. In these techniques, the composition of BMG remains unchanged. Alternatively, the mechanical treatment alters the structural characteristics of the as-solidified amorphous material, such as by introducing residual stress or stress gradients. To name the most important treatments, one can list reduced contact friction [159], mechanical imprinting [9], cold rolling [12, 14, 137, 160, 161], channel-die compression [17], shot peening [25, 162], sand blasting [163], laser surface treatment [164], rapid defect printing [165], elastostatic pre-loading [166, 167] and creation of notched structure [168]. The first three techniques have been used in this thesis and are summarized here as following.

2.3.2.1 Reduced contact friction

Scudino et al. used Cu foils between the loading platens and the $Zr_{41.2}Ti_{13.8}Cu_{12.5}Ni_{10}Be_{22.5}$ BMG specimen in uniaxial compression tests. Their results revealed that the Cu foil acts like a solid lubricant which leads to a reduced contact friction between loading platens and sample. Reduced frictional restraints lead to the formation of several shear bands on the lateral surface of the compression specimen and strongly affects plastic deformation of the glass, which increases from 0.15% for the specimen with normal testing conditions to about 8% for the sample lubricated with the Cu foil [159].

2.3.2.2 Cold rolling

Cold rolling has been used by several groups as a mechanical method to enhance the compression and tensile plasticity of BMGs [12, 14, 137, 160, 161]. Yokoyama et al. in 2008 used cold rolling to induce 10% of area reduction in $Zr_{50}Cu_{30}Ni_{10}Al_{10}$ BMG sheets and achieved 0.5% of tensile plasticity with enhanced multiple shear banding in the rolled samples [137]. Later in 2010, Scudino et al. studied the effect of cold rolling on the mechanical behavior of the $Zr_{60}Ti_5Ag_5Cu_{12.5}Ni_{10}Al_{7.5}$ BMG and noticed that a small size reduction of only 5% by rolling creates a high density of shear bands and remarkably improves the compressive strength and plastic deformation by about 20 and 40%, respectively. They attributed this to the creation of a heterogeneous microstructure which consists of shear softened regions surrounded by hard undeformed regions [161]. Moreover, in 2010, Cao et al. studied the effect of pre-existing shear bands created via rolling on the tensile properties of the $Zr_{64.13}Cu_{15.75}Ni_{10.12}Al_{10}$ BMG. They stated that since the shear band and corresponding affected zone generally have a lower density and hardness compared with the amorphous matrix, such soft regions are preferential places for initiation of new shear bands. They indicated that the appropriate density and distribution of shear bands can efficiently inhibit shear band propagation, resulting in the formation of multiple shear bands and tensile ductility. In addition, they found out that an efficient intersection of shear bands in conjugated directions results in a work-hardening behavior [14]. Song et al. [160] examined cold rolling of the $Cu_{47.5}Zr_{47.5}Al_5$ BMG to attain improved mechanical properties and reported 0.7% of tensile plasticity together with work-hardening and larger fracture strength. Using microhardness test, they detected an increase in the hardness of the as-rolled specimens with a more heterogeneous distribution. In addition, their SEM images revealed a large number of pre-existing shear bands with different morphologies distributed on the surface of the as-rolled sample. Moreover, using density measurements, they reported a 0.28% of increase in the density of as-rolled sample with respect to the as-cast specimen which was attributed to an increase in the free volume produced in the shear bands [160].

2.3.2.3 Imprinting

In 2011, Scudino et al. treated brittle plates of $Zr_{52.5}Ti_5Cu_{18}Ni_{14.5}Al_{10}$ metallic glass with imprinting technique (details are shown in Figure 2-14) and achieved about 1% of tensile plasticity through the proper control of shear band formation and propagation. Using microhardness maps, they observed that the treated microstructure has a cross section that consists of alternating soft and hard regions. Morphology of the imprinted samples after fracture is affected by these heterogeneities through the formation of a high density of branched shear bands which results in a more homogeneous distribution of the plastic strain [9].

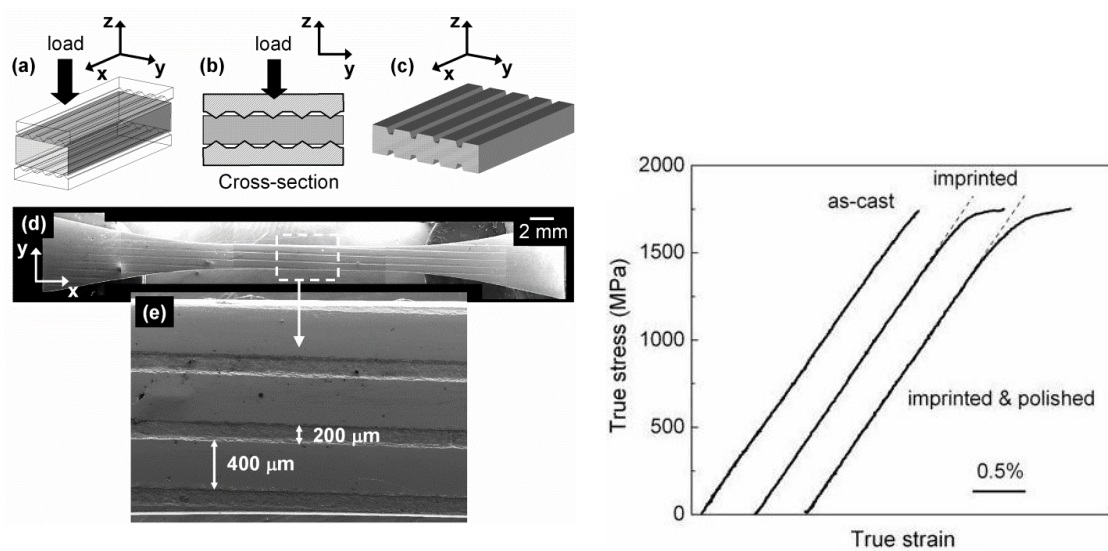


Figure 2-14 Schematic of imprinting method with stress-strain curves illustrating enhanced tensile ductility of imprinted BMG versus as-cast sample [9]

2.4 High energy x-ray characterization of deformed BMGs

2.4.1 Advantage of synchrotron over x-ray machines

Typically, the structure of metallic glasses is studied using conventional laboratory x-ray diffraction (XRD) and transmission electron microscopy (TEM) [38]. However, conventional XRD has some limitations. They are not able to distinguish ultra-fine crystallites in an amorphous structure while synchrotron radiation operated in the transmission mode could help in identifying fine crystalline features, of the length scale of the order of 10 nm [169, 170]. Laboratory XRD has larger wavelength which means a limited range in reciprocal space while a range of wavelengths over a wide

energy range can be used with hard x-rays, which are typically around an order of magnitude lower than for conventional XRD [171]. In addition, high-energy x-rays provided by synchrotron radiation sources have the advantage of high penetration into most materials and have received extensive attention due to high resolution in real-space, which is desirable for disordered materials. Moreover, the sample radiation time is extremely rapid in comparison with conventional XRD due to provided high flux and produces very high signal-to-noise ratio [172].

2.4.2 Real and reciprocal space analysis of metallic glasses

The direct information achieved from diffraction of metallic glasses is the scattering intensity, $I(q)$, as a function of the scattering vector, $q = 4\pi \sin \theta/\lambda$, where θ is the half of scattering angle and λ is the radiation wavelength. $I(q)$ is defined as the scattering intensity from an arbitrary collection of atoms averaged over all orientations. This is given by Debye scattering equation [173]:

$$I(q) = \sum_m \sum_n f_m f_n \frac{\sin qr_{mn}}{qr_{mn}} \quad \text{Equation 2-13}$$

where the summations run over all individual atoms and r_{mn} is the distance between atoms m and n . For an amorphous solid, the knowledge of all atomic positions is not accessible due to the lack of periodicity. However, as Ehrenfest pointed out, the scattering from amorphous materials can be treated in an approximate way by applying Eq. 2-13 to a diatomic gas, for which coherent scattering between molecules can be neglected. If the atoms are identical,

$$I(q) = \sum_m \sum_n f_m f_n \frac{\sin qr_{mn}}{qr_{mn}} = 2f^2 \left(1 + \frac{\sin qd}{qd}\right) \quad \text{Equation 2-14}$$

where f is the scattering factor of an individual atom, and d is the distance between two atoms. Supposing that f is independent of q , the maximum intensity occurs at $q_{\max}=1.23(2\pi)/d$. One can use this equation in the case of amorphous materials with different constant:

$$q_{\max} = \frac{K}{d} \quad \text{Equation 2-15}$$

where K is a constant that depends on the arrangement of atoms. This constant cannot be determined for amorphous materials due to lack of information on the atomic positions. However, it can be accurately used to follow the variations of d [173].

The structure factor is defined as:

$$S(q) = I(q)/N\langle f(q) \rangle^2 \quad \text{Equation 2-16}$$

where N is the number of atoms, $f(q)$ is the atomic-scattering factor for x-rays, and the angular brackets indicate averaging over the composition of the material. The real space structural information is obtained via the pair distribution function (PDF), $g(r)$, in which r is the distance from an average atom located at the origin. It can be obtained by Fourier transforming $S(q)$ according to the following equations [173]:

$$\rho(r) - \rho_0 = \frac{1}{8\pi^3} \int_{q_{min}}^{q_{max}} 4\pi q^2 (S(q) - 1) \frac{\sin(qr)}{qr} dq \quad \text{Equation 2-17}$$

$$g(r) = \rho(r)/\rho_0 \quad \text{Equation 2-18}$$

where ρ_0 is the average atomic density. In addition, the reduced pair distribution is defined as:

$$G(r) = 4\pi r [\rho(r) - \rho_0] \quad \text{Equation 2-19}$$

Another function related to PDF is the radial distribution function (RDF), which is defined as $4\pi r^2 \rho(r)$. With this function, the coordination number of a particular atomic shell can be calculated by integrating the RDF over a chosen range of r [173].

2.4.3 Determination of strain from synchrotron data

A significant application of high energy synchrotron x-ray has been the characterization of the atomic-scale lattice strain in metallic glass composites [174, 175] as well as the estimation of the deformation-induced free volume in metallic glasses [28, 176]. The measurement of the atomic-scale strain tensor in metallic glasses by high energy synchrotron x-ray was implemented for the first time by Poulsen et al. [5] who converted 2D diffraction patterns into 24 integrated divided angular segments (representing 24 different directions). The peak position of each

segment was found by fitting mathematical peak functions to the experimental data. In order to study the strain in real space, the peak positions of the PDFs are extracted with the same method. As it was shown in Eq. 2-15, the shift in the measured peak position corresponds to changes in interatomic distances and is converted into strain values using the following equation (in reciprocal space):

$$\varepsilon = q_0 - q_\sigma / q_\sigma \quad \text{Equation 2-20}$$

In the real space, the strain is calculated from peak positions of the PDFs according to following equation:

$$\varepsilon = r_\sigma - r_0 / r_0 \quad \text{Equation 2-21}$$

Then, the angular variation of the strain is fitted to the following equation to obtain the strain tensor elements ε_{11} , ε_{12} , ε_{22} [5]:

$$\varepsilon_\theta = \varepsilon_{11} \cos^2 \theta + \varepsilon_{12} \cos \theta \sin \theta + \varepsilon_{22} \sin^2 \theta \quad \text{Equation 2-22}$$

2.4.4 Characterization of elastic response of BMGs

The majority of the reported strain analysis of metallic glasses using high energy x-ray have focused on the characterization of the elastic deformation. This is mainly because most of metallic glasses exhibit limited plasticity. In this context, using Poulsen's approach, Stoica et al. [6] studied in reciprocal space the behavior of the $\text{Zr}_{64.13}\text{Cu}_{15.75}\text{Ni}_{10.12}\text{Al}_{10}$ metallic glass at different stages of tensile deformation and found a linear shift of the peak position of the first diffraction maximum with the applied load. The peak position shifts toward lower q values with increasing the tensile stress, as illustrated Figure 2-15(a). In the real space, this means that the tensile stress increases the average atomic distances along the loading direction and results in a linear correlation in both longitudinal and transverse direction as it is clear from Figure 2-15(b) [177]. A similar linear relationship in the range of elastic deformation was also reported for longitudinal and transverse strain under uniaxial tensile deformation for $\text{Cu}_{50}\text{Zr}_{50}$ and $\text{Cu}_{65}\text{Zr}_{35}$ glassy ribbons [178], $\text{Zr}_{62}\text{Al}_8\text{Ni}_{13}\text{Cu}_{17}$ and $\text{La}_{62}\text{Al}_{14}(\text{Cu}_{5/6}\text{Ag}_{1/6})_{14}\text{Co}_5\text{Ni}_5$ [179], $\text{Zr}_{64.13}\text{Cu}_{15.75}\text{Ni}_{10.12}\text{Al}_{10}$ [180], $\text{Ti}_{40}\text{Zr}_{25}\text{Ni}_3\text{Cu}_{12}\text{Be}_{20}$ [181], and under uniaxial compression for $\text{Zr}_{57}\text{Ti}_5\text{Cu}_{20}\text{Ni}_8\text{Al}_{10}$ [173] and $\text{Cu}_{64.5}\text{Zr}_{35.5}$ [7].

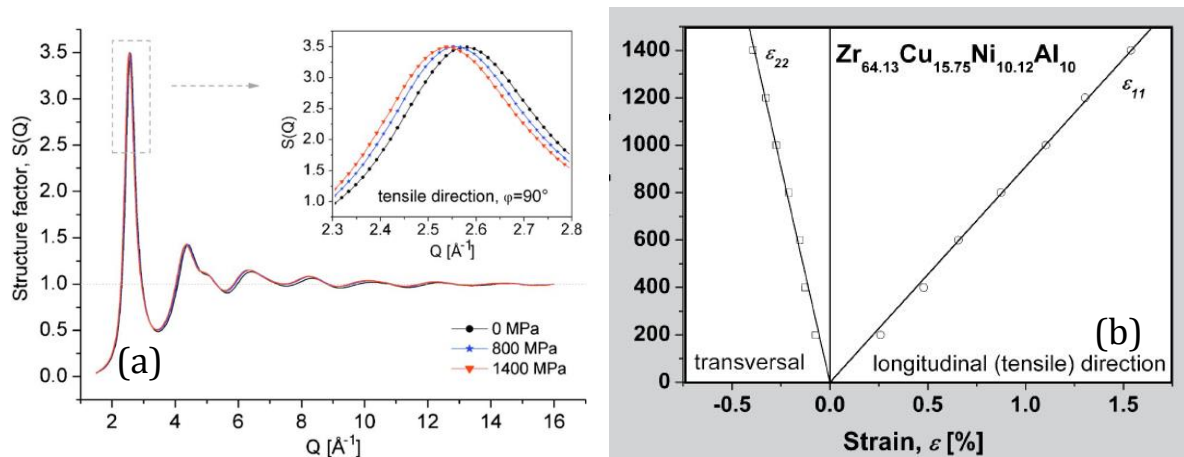


Figure 2-15 (a) Peak position change in the structure factor of a BMG with increasing tensile loading [6] (b) The longitudinal and transverse strain measured from peak positions of the structure function in $Zr_{64.13}Cu_{15.75}Ni_{10.12}Al_{10}$ BMG in tensile test [177]

An interesting behavior was reported by Das et al. [182] who measured by x-ray synchrotron radiation the atomic-scale elastic strain of $Zr_{55}Cu_{20}Ni_{10}Al_{10}Ti_5$ and $Cu_{47.5}Zr_{47.5}Al_5$ BMGs at room temperature under uniaxial compression (Figure 2-16).

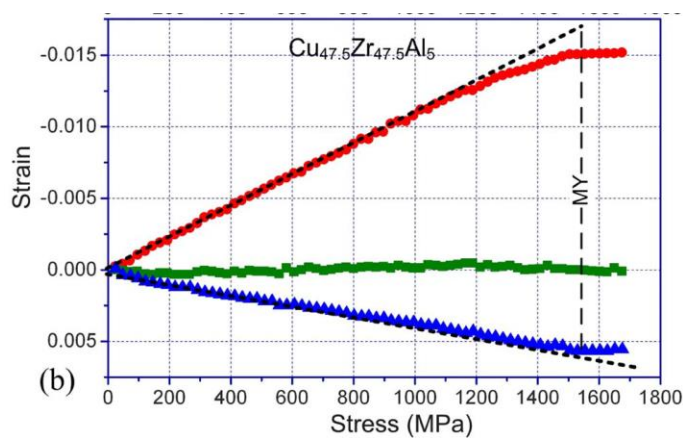


Figure 2-16 Deviation of longitudinal and transverse atomic scale strain from linearity in the range of elastic stresses [182]

While the linear correlation between atomic scale strain and macroscopic stress was recorded for brittle $Zr_{55}Cu_{20}Ni_{10}Al_{10}Ti_5$ BMG, in the case of slightly plastically-deformable $Cu_{47.5}Zr_{47.5}Al_5$ BMG a deviation from the linear stress-strain relationship at the onset of macroscopic flow was observed. They attributed this nonlinear elastic behavior to the deformation of topologically unstable short-range ordered clusters at the onset of the activation of STZs below plastic yielding [182].

Interestingly, they also investigated the change of the full width at half maximum (FWHM) of the first peak of the scattering intensity at different applied stresses (Figure 2-17). With increasing stress, the FWHM decreases in the loading direction and increases in the transverse direction. The change in FWHM under the stress is significantly higher in the plastic $\text{Cu}_{47.5}\text{Zr}_{47.5}\text{Al}_5$ than in the brittle $\text{Zr}_{55}\text{Cu}_{20}\text{Ni}_{10}\text{Al}_{10}\text{Ti}_5$. They argued that the decrease of FWHM means that more SRO clusters participate during elastic deformation, redistributing the strain in the transverse direction. With increasing stress, the higher numbers of such entities are activated and realign themselves under the applied stress. This will result in more redistribution of free volume, averaging of the local hydrostatic stress. This will lead in turn to a homogenous activity of the STZs and larger plasticity. On the other hand, in the case of the brittle glass, the change of the peak width is rather slow due to the piled up STZs, which interact with the locally quenched-in stress resulting in a more inhomogeneous strain distribution, hampering the dynamics of the STZs in carrying plasticity [182].

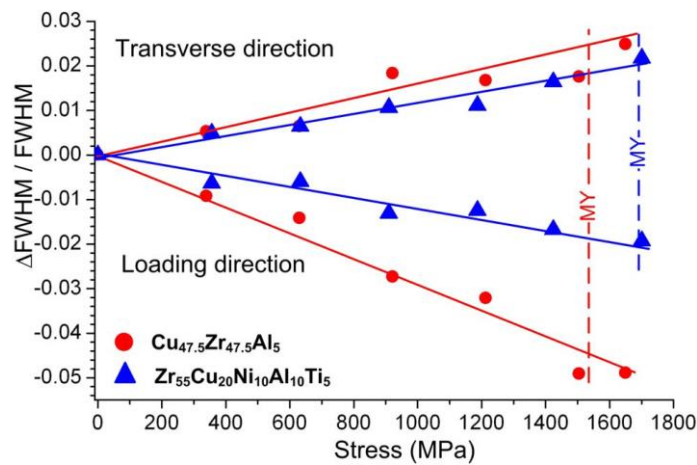


Figure 2-17 Variation of FWHM in loading and perpendicular direction for two brittle and ductile BMGs [182]

In addition to the strain values, the change in the shape of the peaks in the real space functions can bear some valuable information. It was shown by Srolovitz et al. [183] that the width and height of the peaks of the pair distribution function are related to the second moment of the atomic-level hydrostatic stress distribution. They defined the atomic level hydrostatic pressure as follows:

$$p = -\frac{1}{3} (\sigma_1 + \sigma_2 + \sigma_3) \quad \text{Equation 2-23}$$

where σ_1 , σ_2 , σ_3 are the principal stresses. The increase of the height and the decrease of the width (sharpening) of the PDF peaks decrease the variance of the atomic level hydrostatic pressure and means more uniform distribution of the atomic-level strain. Inversely, the decrease of height and the increase of width of the peaks (broadening) imply more fluctuation of the atomic level strain [183, 184]

The elastic constants of the coordination shells of metallic glasses can be accurately determined by characterizing the atomic scale elastic behavior during uniaxial deformation. The Young's modulus is obtained from slope of the macroscopic stress versus atomic strain and the Poisson's ratio can be calculated by dividing transverse strain by longitudinal strain. Stoica et al. [6, 177] compared their results with results of similar tests on $\text{Zr}_{62}\text{Al}_8\text{Ni}_{13}\text{Cu}_{17}$ and $\text{La}_{62}\text{Al}_{14}(\text{Cu}_{5/6}\text{Ag}_{1/6})\text{Co}_5\text{Ni}_5$ glasses reported by Wang et al. [179] and $\text{Cu}_{50}\text{Zr}_{50}$ and $\text{Cu}_{65}\text{Zr}_{35}$ BMGs reported by Mattern et al. [178]. They demonstrated that the elastic constants calculated from the atomic scale strain tensor of the different atomic shells are different from those measured by ultrasonic techniques which measure the average of elastic constants of different atomic shells as a bulk property. They categorized the investigated BMGs into non-deformable and deformable. In the case of "non-deformable" or intrinsically brittle BMGs, the bulk elastic constants are almost similar to those obtained from the strain tensor analysis. In the case of plastically deformable BMGs each atomic shell has a different stiffness, as revealed from the large differences of the elastic constants from ultrasonic and tensor analysis. They believed that such an anisotropy can induce local shear transformations which result in macroscopic plasticity [6, 177].

Very recently, Chen and coworkers investigated the atomic scale mechanisms of the tension-compression asymmetry of $\text{Zr}_{46.5}\text{Cu}_{45}\text{Al}_7\text{Ti}_{1.5}$ metallic glass and reported that the specimen has a similar macroscopic elastic modulus during tension and compression. However, the elastic modulus calculated based on the strains determined from $S(q)$ and $G(r)$ are 105 and 112 GPa, respectively, which are higher than the value of 92 GPa measured by ultrasonic measurement. They concluded that the apparent elastic deformation in metallic glasses involves micro-plastic events. The atomic bonds are not only compressed or stretched, but are also possibly switched during loading in the apparent elastic deformation region [185].

2.4.5 Length scale dependence of strain in metallic glasses

Based on the proposed structural models for the deformation of metallic glasses introduced earlier in this chapter, each peak in the pair distribution function of metallic glasses represents an atomic coordination shell around a given central atom. Any movement in the peak position (or a defined point near the maxima) of these shells can be translated to the atomic scale strain of the corresponding shell. In recent years, several groups have focused on the characterization of the atomic structure of different shells using synchrotron analysis under different loading modes and have compared it with the macroscopic strain.

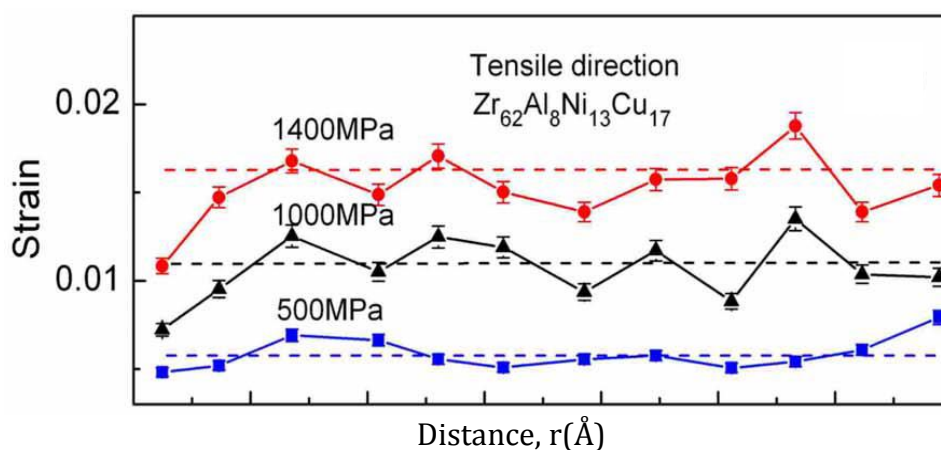


Figure 2-18 Length scale dependence of $Zr_{62}Al_8Ni_{13}Cu_{17}$ under different tensile stresses [186]

In this context, Wang et al. reported the tensile behavior of $Zr_{62}Al_8Ni_{13}Cu_{17}$, $Cu_{46}Zr_{46}Al_8$, $Zr_{48}Cu_{43}Al_7Ag_2$, and $La_{62}Al_{14}(Cu_{5/6}Ag_{1/6})_{14}Co_5Ni_5$ BMGs investigated using high energy x-ray. They found that the local strain, measured from different peaks of the PDFs, is homogeneously distributed over the shells at low stress. However, heterogeneity appears when the stress is close to the fracture strength (Figure 2-18). The largest fluctuation of strain was reported in the range of 10–14 Å that seems to be the boundary between superclusters, where excess open volume may accumulate [186].

Wilson and coworkers [187] performed in-situ neutron scattering on $Zr_{57}Nb_5Cu_{15.4}Ni_{12.6}Al_{10}$ BMG under compression test. They measured the atomic scale strain based on the shift in the center of mass as well as the variance of each

coordination shell in the pair distribution function curve. They stated that strain values calculated from the center of mass are less noisy than those of the peak position or intercept of the coordination shells. 29% difference between the elastic modulus value calculated from the atomic scale curve and the macroscopic value was reported. They attributed such a discrepancy to anelastic deformation occurring in low density regions that are not reflected in the atomic strain curves but can cause the decrease of shear and Young's modulus. They reported that the length scale dependency (

Figure 2-19) indicates a sharp rise around the inter-atomic distance of 10 Å. This size corresponds interestingly to the diameter expected for STZs or roughly 3 or 4 atoms in diameter corresponding to the size of one local cluster of atoms [187].

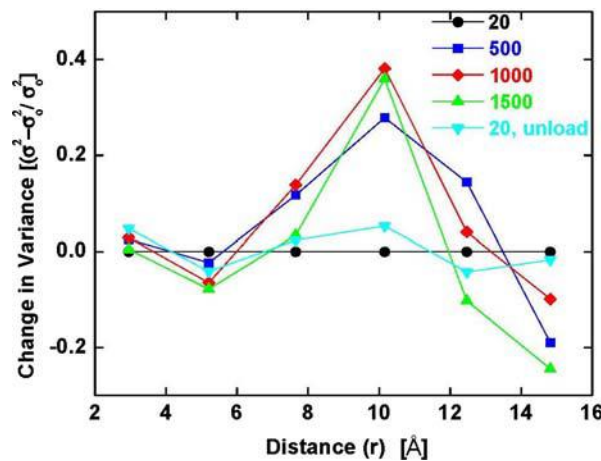


Figure 2-19 Length scale dependence of change in variance for $Zr_{57}Nb_5Cu_{15.4}Ni_{12.6}Al_{10}$ BMG in different compressive loads [187]

Hufnagel et al. [173] studied the $Zr_{57}Ti_5Cu_{20}Ni_8Al_{10}$ BMG under uniaxial compression up to stresses of approximately 60% of the yield stress and found that the strain values extracted from real and reciprocal space are in good agreement with each other for length scales greater than 4 Å. Interestingly, instead of using the peak position shift in order to calculate strain in real space, they tracked the point in each coordination shell where the PDF function equals 1, arguing that these crossing points are less sensitive to asymmetry effects which might result in scattered strain values when calculated from peak positions. They report that the strain measured for atoms in the nearest-neighbor shell (2-3 Å), is smaller than that for more distant shells (4-10 Å). Moreover, as it is clear from Figure 2-20, the strain in the region around $r=13-14$ Å is consistently larger than that at other values of r . They argued that the compliance of the glass in this length scale has an additional contribution

from atoms in the fifth or sixth atomic shell around an average atom, probably due to a redistribution of free volume [173].

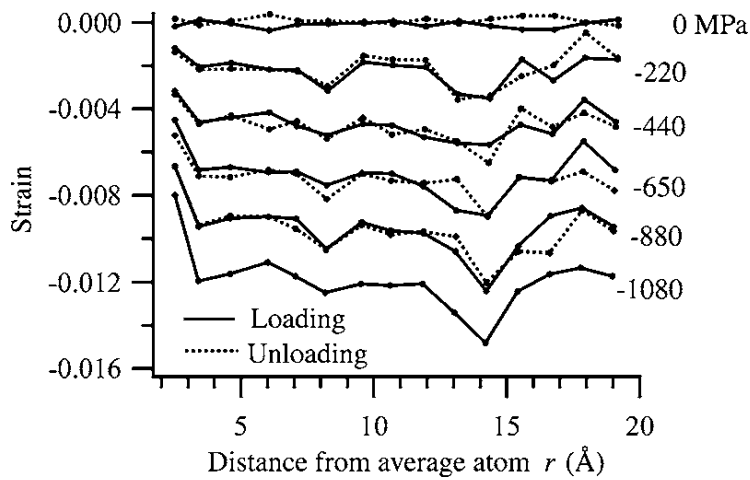


Figure 2-20 Length scale dependence of the $Zr_{57}Ti_5Cu_{20}Ni_8Al_{10}$ BMG under uniaxial compression at different stresses [173]

Later on, Vempati and coworkers [188] performed a comprehensive study on the same $Zr_{57}Ti_5Cu_{20}Ni_8Al_{10}$ BMG, under different loading modes: uniaxial compression, uniaxial tension and pure shear. They reported a length scale dependence of the atomic scale strain in all three loading modes. The atomic strain approaches the macroscopic strain value with increasing the distance from average atom. More importantly, contrary to the approach of Suzuki et al. [189] which state that the calculation of the strain without the supposition of an anisotropic solid can lead to wrong strain values, Vempati et al. indicated that the apparent length-scale dependence of elastic strain is not an artifact of the assumption of structural isotropy in the data analysis. This is proved by their molecular dynamics simulations as well as diffraction experiment for a loaded body under uniaxial tension which reproduced qualitatively the same length scale dependence behavior. They also showed that in the simulations under hydrostatic loading, the length-scale dependence of the elastic strain is reduced. They argue that the length scale dependence might be related to nonaffine atomic displacements in which each atom has access to a range of different environments and the collective motion in the same direction is impossible due to disorder. Non-affine atomic displacements are smaller under hydrostatic loading (due to lack of shear strain) than under uniaxial loading (where there is a strong shear component) and may play the main role in the length-scale dependence of elastic strain. Therefore, the shear strain drives the

exchanges of atomic neighbors resulting in the apparent length-scale dependence of elastic strain calculated from $g(r)$ [188].

In order to prove the correlation between length scale dependency and nonaffine atomic displacement, Vempati et al. extracted the fraction of atoms versus the angle of displacement with respect to the loading axis using simulation model (Figure 2-21). The nonaffine displacements are isotropically distributed for hydrostatic loading while under uniaxial loading they are preferentially oriented along the loading axis [188]. In summary, the inhomogeneity of elastic deformation of a metallic glass is most pronounced in the presence of a resolved shear stress and this leads to the observed length-scale dependence of elastic strain in the few near-neighbor shells.

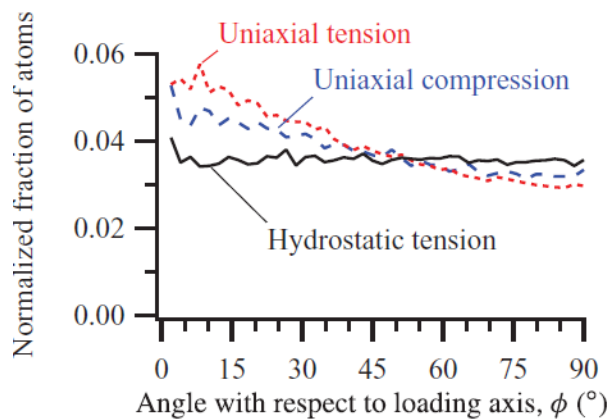


Figure 2-21 Nonaffine displacements are isotropically distributed for hydrostatic loading while under the uniaxial loading, they are preferentially oriented along the loading axis [188]

In 2013, Huang et al. studied the strain profile in notched and un-notched tensile $\text{Ti}_{40}\text{Zr}_{25}\text{Ni}_3\text{Cu}_{12}\text{Be}_{20}$ BMG samples using synchrotron XRD and SEM. They reported that the strain calculated from the peak shifts of the scattering intensity patterns for the notched sample shows a clear gradient along the direction perpendicular to the tensile axis. Moreover, the strain calculated from the PDFs showed a strong dependence on atomic coordination shells, being the smallest for the first near neighbor shell and increases for the shells at higher r , approaching the strain calculated from peak shifts in scattering intensity. In the final stage of deformation, they also observed a sudden increase of strain calculated from the PDFs and attributed it to shear-induced dilatation of the randomly close-packed atomic

configuration resulting from the shear band formation due to the local stress concentration [181].

2.4.6 Short range order characterization

In order to get information on the chemical and topological arrangement of the first coordination shell one has to analyze the data in real space. This has been done by several research groups for different metallic glasses [6, 173, 177]. Normally, in the case of multi-component metallic glasses the first maximum includes contributions from existing atomic pairs, which overlap to form the main broad maximum. In order to track the peak position shift of the individual atomic pairs, one has to deconvolute the first main maximum in the pair distribution function to have separated contribution of each atomic pair. Then by comparing the peak position with the interatomic distance of atomic pairs (sum of atomic radii of two elements), one can determine which peak belongs to which atomic pair. The contribution of each atomic pair to the PDF is weighted by the atomic scattering factors of the elements and by their concentration. Therefore, with a good approximation, it is possible to neglect the influence of elements that have low scattering factor with relatively low concentration. In addition, it should be noted that contributions of atoms with the same sizes are indistinguishable due to overlapping [173]. In this context there is considerable number of studies that used this approach to investigate chemical arrangement of elements in the SRO region with applied stress [6, 173, 177].

Hufnagel and Ott studied the $Zr_{57}Ti_5Cu_{20}Ni_8Al_{10}$ BMG under uniaxial compression. Based on the analysis of the radial distribution function in the SRO region (Figure 2-22) they attributed the first peak at $r=3.133 \text{ \AA}$ to Zr-Zr pairs. The measured modulus is $93 \pm 1 \text{ GPa}$, which compares well with the elastic modulus of polycrystalline Zr (about 96 GPa). The second peak at $r=2.661 \text{ \AA}$ is an overlapping of (Cu,Ni)-(Cu,Ni) and Zr-(Cu,Ni) pair correlations. The reported modulus of $149 \pm 8 \text{ GPa}$ for this peak is of the same order of magnitude of the average elastic moduli of polycrystalline Cu (115 GPa) and Ni (204 GPa). Moreover, the width of the second peak is approximately half as large as that of the first peak, indicating that the second peak has contributions from two distinct types of pair correlations. In

addition to the shift of the peak position, the width and amplitude of the two contributions to the first peak in the radial distribution function change during loading. These changes together are counterbalanced resulting in a constant calculated coordination number of 11.5 atoms during loading [173]. With a similar approach, detailed analysis of Stoica and coworkers on $Zr_{64.13}Cu_{15.75}Ni_{10.12}Al_{10}$ BMG revealed that the atomic bonds Zr-Zr, Zr-Cu, and Zr-Ni are the dominant atomic pairs constituting to the first coordination shell of the PDFs [6, 177].

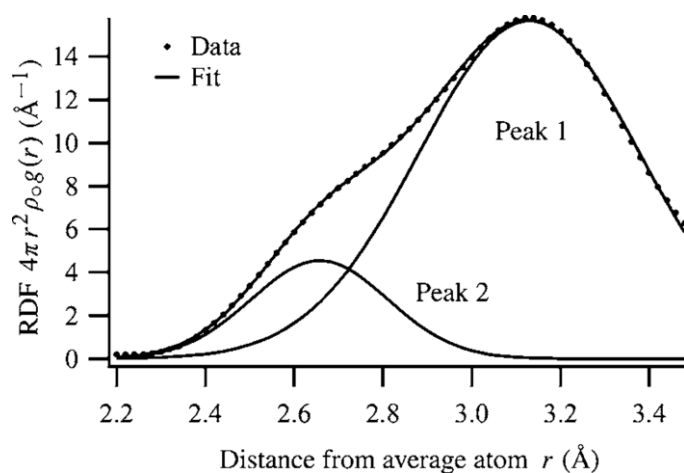


Figure 2-22 Characterization of the short range order peaks in the radial distribution function [173]

The sine Fourier transformation of the structure function in order to switch to real space analysis assumes that the structure behaves isotropically under stress. However, in the presence of stress, the structure might turn into an anisotropic state. In this case, the use of the sine Fourier transformation approach is claimed to introduce errors in the measurement of strain [190]. This has been the motivation for Suzuki et al. [189] to use an alternative method to investigate short-range order of metallic glasses based on the spherical harmonics transformation. Using this transformation, the structure factor is divided into two main components, $S_0(q)$ and $S_2(q)$, respectively denoted as isotropic and anisotropic contributions, according to following equations:

$$S_0(q) = \frac{\sqrt{4\pi}}{3} (S(q, \varphi = 0^\circ) + 2S(q, \varphi = 90^\circ)) \quad \text{Equation 2-24}$$

$$S_2(q) = \sqrt{\frac{16\pi}{45}} (S(q, \varphi = 0^\circ) - S(q, \varphi = 90^\circ)) \quad \text{Equation 2-25}$$

The angles $\varphi = 0$ and $\varphi = 90$ correspond to the directions parallel and perpendicular to the tensile direction, respectively. The isotropic component exhibits negligible change with increasing stress while the anisotropic contribution is more sensitive to stress. The isotropic atomic density function is given by the sine Fourier transformation of isotropic structure function as follows:

$$\rho_0(r) = \rho_{mean} + (1/2r\pi^2) \cdot \int (S(q) - 1) \cdot q \cdot \sin(q \cdot r) \cdot dq \quad \text{Equation 2-26}$$

while the anisotropic component is obtained using Bessel transformation of anisotropic structure function as follows:

$$\rho_2(r) = -\frac{1}{2\pi^2} \cdot \sqrt{(45/16\pi)} \int S_2(q) \cdot J_2(qr) \cdot q^2 dq \quad \text{Equation 2-27}$$

in which, $J_2(qr)$ is the spherical Bessel function and is defined as following:

$$J_2(qr) = \left(\frac{2}{(qr)^3} - \frac{1}{qr} \right) \sin(qr) - \frac{2}{(qr)^2} \cos(qr) \quad \text{Equation 2-28}$$

Therefore, the atomic density of any direction, φ , is given by:

$$\rho(r, \varphi) = \rho_0(r) \sqrt{\frac{1}{4\pi}} + \rho_2(r) \sqrt{\frac{5}{16\pi}} (3 \cos^2 \varphi - 1) \quad \text{Equation 2-29}$$

There is an important point about the above equations. It was proven by Suzuki et al. that the anisotropic structure factor of a solid under a shear strain is proportional to the derivative of the isotropic structure function. However, from the experimental results, this condition is satisfied only in the q range below about 3 \AA^{-1} . In a similar way, mathematically, the anisotropic atomic density scales with the first derivative of the isotropic atomic density. This is, however, valid only in the coordination shells beyond the first shell. Suzuki et al. [189] argued that this deviation is indicative of an atomic rearrangement in the short range order length scale. According to Figure 2-23, they suggested that with increasing the uniaxial load, the isotropically formed bonds in the first coordination shell are stretched along the loading direction (Figure 2-23 (b)). This will cause the rearrangement of the atomic bonds in a way that some atoms from the second coordination shell will join the first coordination shell in the transverse direction, while in the loading direction some atoms from the first shell will jump into the second coordination shell (Figure 2-23 (c)). This

phenomenon, described as “deformation-induced bond orientational anisotropy” in metallic glasses, has been also reported by other studies [189, 191-193] and is effective in the short range order length scale.

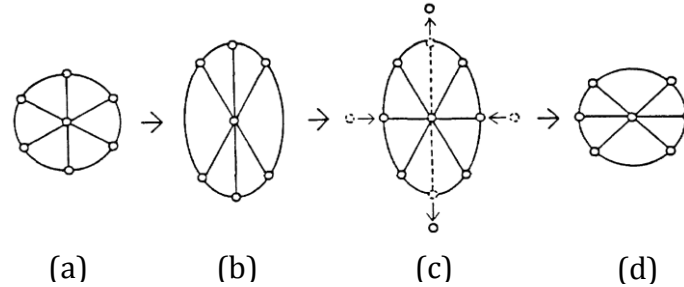


Figure 2-23 Deformation induced bond orientational atomic anisotropy by rearrangement in the first coordination shell [189]

Based on this analysis, Mattern and coworkers studied $\text{Cu}_{50}\text{Zr}_{50}$, $\text{Cu}_{65}\text{Zr}_{35}$ glassy ribbons under uniaxial tensile stress [178]. As it is illustrated in Figure 2-24, the difference in the isotropic structure function, $S_0(150\text{ N}) - S_0(0\text{ N})$, is small with maximum of about 1%, occurring at the first maximum.

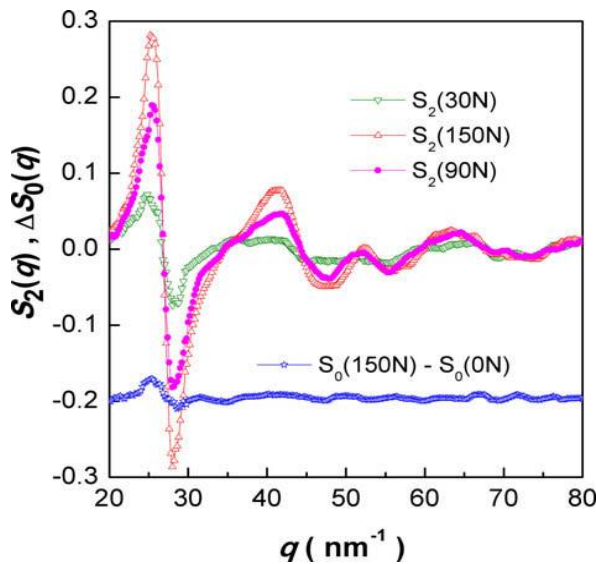


Figure 2-24 Variation of the isotropic and anisotropic components of the structure function with increasing tensile stress [178]

The amplitude of the anisotropic part of the structure factor, $S_2(q)$, increases gradually as a function of the applied stress and reaches values up to 10% at the first maximum. Similarly, the variations of the anisotropic component of the atomic density in the first coordination shell along the tensile and perpendicular directions revealed that some anelastic topological and chemical changes occur in the short

range order well below the yield strength. Overall, it was concluded that the number of Zr–Zr pairs increases along the tensile direction, whereas Cu–Zr pairs decreases with increasing the applied stress. The opposite behavior occurs for the perpendicular direction [178].

Wang et al. [7] also studied the $\text{Cu}_{64.5}\text{Zr}_{35.5}$ BMG under uniaxial compression and reported similar results based on the bond orientational anisotropy approach. They stated that for the (Cu, Zr)-Cu pair the coordination number increases in the loading direction but decreases in the transverse direction (an opposite behavior occurs for the Zr–Zr pairs). The total coordination numbers in the two directions for the Cu–(Zr,Cu) and Zr–Zr pairs remain almost constant, which means that, for the Zr–Zr pair, the bond reorientation is governed by breaking the bonds in the loading direction and making new bonds in the transverse direction (With opposite behavior occurring for the Cu–(Zr,Cu) pair). More importantly, they reported that the observed structural changes in the elastic range are completely reversible. The PDF of BMGs after unloading from the yield stress did not show significant difference compared to the as-cast state [7]. With the bond orientational anisotropy approach, they claimed that due to the atomic rearrangements upon stress, the strain values cannot be correctly determined using nearest neighbor distances.

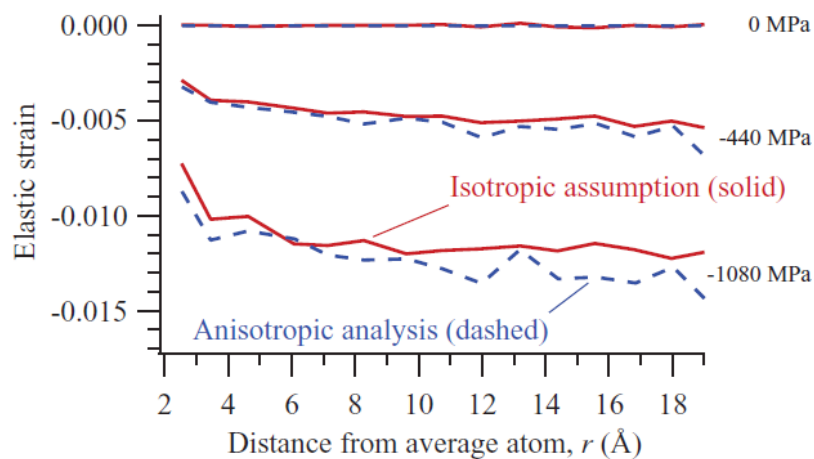


Figure 2-25 Agreement in elastic strain values between the isotropic assumption and the full anisotropic analysis is good at all values of r for three conditions of no load, -440 MPa, and -1080 MPa [188]

Vempati et al. [188] have recently demonstrated in their studies on the $Zr_{57}Ti_5Ni_8Al_{10}Cu_{20}$ BMG under uniaxial tension that the agreement in the elastic strain values between the isotropic assumption and the full anisotropic analysis is good at all values of r for the conditions of zero load, -440 MPa, and -1080 MPa (Figure 2-25). Therefore, they conclude that although uniaxial elastic loading introduces a measurable structural anisotropy, the observed strain as well as the length-scale dependence of elastic strain are almost similar in both isotropic and full anisotropic treatment [188].

2.4.7 Characterization of medium range order and plastic response of BMGs

As mentioned in the previous sections, the strain evaluated from the coordination shells at larger r values or correspondingly from the first peak in the scattering intensity approaches the macroscopic value of strain. Ma and coworkers [194] summarized the experimental values of the first peak position, q_1 , for a variety of metallic glasses, determined from neutron and x-ray diffraction. Besides, they also collected atomic volumes (V_a) determined from mass density measurements. By plotting q_1 versus V_a on a logarithmic scale, they found out a scaling relationship according to following equation:

$$q_1 \cdot V_a^{0.433 \pm 0.007} = 9.3 \pm 0.2 \quad \text{Equation 2-30}$$

According to the Ehrenfest relationship, a power of $1/3$ is expected when scaling $1/q_1$ with V_a for crystalline metals with long-range order and for molecular gas with SRO. In contrast, in the case of metallic glasses the above equation yields a power of 0.433 . Ma et al. interpreted this discrepancy as the evidence of a MRO arrangement consisting of a fractal network including connecting icosahedral clusters. As it is illustrated in

Figure 2-26, for the $Cu_{64.5}Zr_{35.5}$ glassy alloy the MRO coordination shells in the pair distribution function are in very good agreement with the following equation in the range of $r > 6.5$ Å:

$$g(r) - 1 = (A/r^D) \exp(-r/\xi) \sin(q_1 r + \varphi) \quad \text{Equation 2-31}$$

where q_1 is the first peak position in the structure function, ξ is the cutoff length, φ is the phase shift and D is reported to be 0.67 ± 0.06 for six Zr-Cu glasses and two Zr-based BMGs [194].

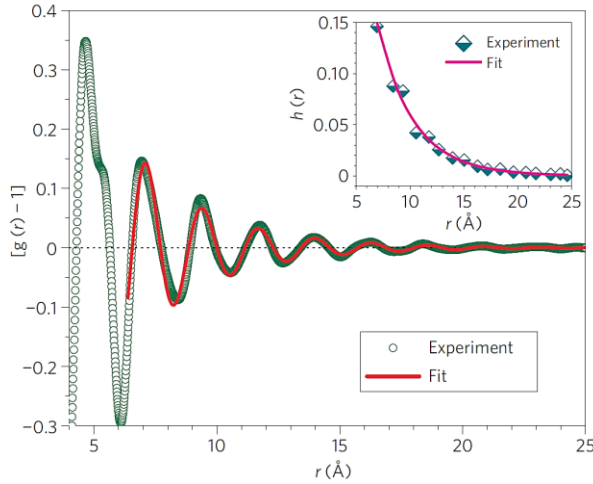


Figure 2-26 Very good agreement of fractal structure equation with reduced PDF of $\text{Cu}_{64.5}\text{Zr}_{35.5}$ in the range of $r > 6.5 \text{ \AA}$ [194]

Wang and colleagues [195] selected $\text{Ni}_{62}\text{Nb}_{38}$, $\text{Cu}_{50}\text{Zr}_{50}$, $\text{Cu}_{64.5}\text{Zr}_{35.5}$, $\text{Cu}_{50}\text{Zr}_{45}\text{Al}_5$, and $\text{Cu}_{50}\text{Zr}_{45}\text{Ti}_5$ metallic glasses with significantly different mechanical properties (elastic moduli, plasticity and yield strength). Using the structure factor obtained from synchrotron scattering intensity, they calculated the atomic volume of the samples as a function of stress according to Eq. 2-30 and showed that with increasing stress, the atomic volumes of all samples decrease by 3.3% in the loading direction and increase by 1.2% in the transverse direction. They also reported that after yielding, the strain value in the first nearest neighbor shell of PDF does not indicate significant change with further increasing of plastic strain and returns back to zero after unloading.

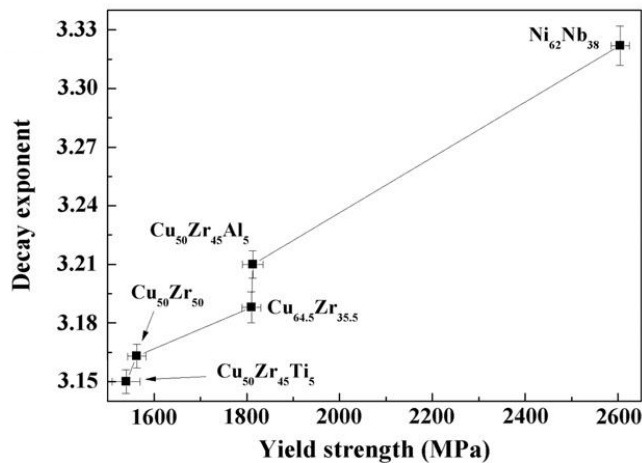


Figure 2-27 Decay exponent, ξ , of five different metallic glasses is proportional with their yield strength values [195]

Despite the change in both loading and transverse direction during the elastic stage, the calculated coordination numbers do not change in the plastic regime and the total coordination numbers of the atomic pairs in the loading and transverse direction remain constant with increasing stress in both elastic and plastic region. By fitting the experimental PDFs to the MRO correlation proposed by Ma et al. (Eq. 2-31) they found out that, the PDFs are in good agreement with this equation in the range of $r > 6 \text{ \AA}$. They indicated that the decay exponent, ξ , is proportional to the yield strength of metallic glasses (Figure 2-27) [195]. In addition, they correlated the anisotropic structural evolution from the atomic re-orientation in the first nearest neighbor shell to the macroscopic behavior of metallic glasses. They argued that the reorientation relaxes the internal stress of the system and, accordingly, it shifts the surrounding atoms to counterbalance the energy change. During this process, the activation energy increment in the shifted region increases with increasing stress, which determines the yield strength [195].

Qu et al. [196] reported on the synchrotron analysis of the $\text{Zr}_{53}\text{Cu}_{18.7}\text{Ni}_{12}\text{Al}_{16.3}$ BMG under uniaxial compression with 4% plasticity. They indicated that the amplitude of the longitudinal compressive strain from both short range order and medium range order increases rapidly and saturates in the plastic deformation region, while the transverse strain increases further in the plastic stage, even after the longitudinal compressive has reached saturation. The in-plane shear strain remains zero in the elastic stage but exhibits a slight deviation from zero strain in the plastic stage, implying that a shear deformation is created during plastic deformation region (Figure 2-28).

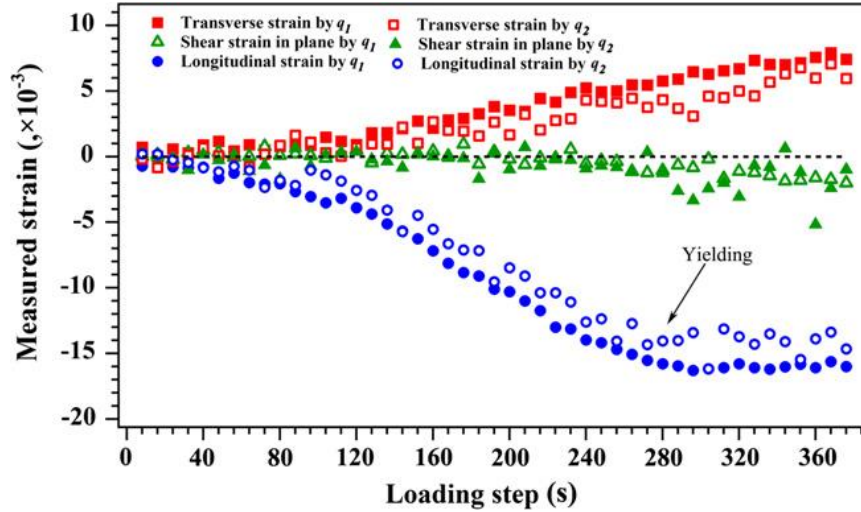


Figure 2-28 Evolution of atomic scale strain in longitudinal and transverse direction for $Zr_{53}Cu_{18.7}Ni_{12}Al_{16.3}$ BMG [196]

Assuming that in the plastic stage the constituent atoms of the BMG behave analogously to ideal hard-spheres, the authors correlated this behavior (increasing transverse strain despite saturated longitudinal strain in plastic deformation range) to the bond reorientation where some atoms are pushed away to flow in the direction perpendicular to the loading direction in order to have plastic deformation. They linked this lateral flow to the flow dilatation which correlates with the frustration of the icosahedral short-range order [196].

In addition, the bond orientational anisotropy analysis indicated that the isotropic part of the structure factor exhibits small changes in the deformation process while the anisotropic part increases proportionally with the elastic strain, and it is almost independent of the plastic strain in the plastic stage. They reported a similar behavior in the case of anisotropic atomic density. Both the positive and negative amplitudes of anisotropic structure function increase gradually, though at different rates, in the elastic stage. In the plastic stage, the negative amplitude continues to grow, while the positive amplitude approaches saturation (Figure 2-29) [196].

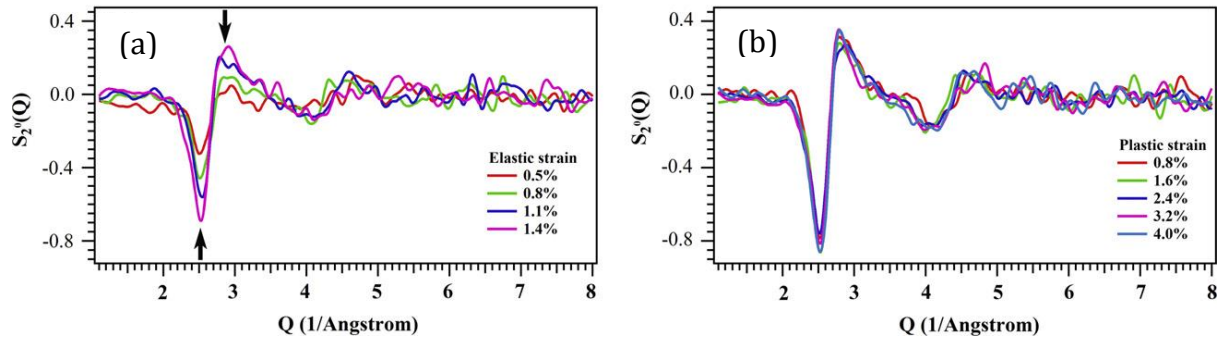


Figure 2-29 Variation of anisotropic structure function in different amounts of elastic and plastic strain [196]

They interpreted this observation such that in the elastic stage the anisotropic behavior of the atomic structure is primarily dominated by one mechanism, the affine change in the interatomic distance, while in the plastic stage the mechanism is likely related to the directional atomic level flows. Overall, they tried to prove that, in addition to the shear band interactions, abundant homogeneous flow at the atomic level contributes significantly to the plastic strain [196]. The asymmetry of the deformation under tensile and compression loading discussed in the past sections was also investigated from the atomic point of view using high energy synchrotron by Chen et al. [185] in 2013 for a $Zr_{46.5}Cu_{45}Al_7Ti_{1.5}$ BMG under uniaxial compression and tension. They extracted the change in the width of all coordination shells in the PDFs and reported the sharpening of the peaks under the compressive stress as an indication of more uniform distribution of atomic level strain which can facilitate the nucleation of multiple shear bands. In contrast, the atomic-level strain becomes more fluctuating during tensile loading (broadening of the peaks), which may result in a dominant shearing and catastrophic failure [185].

3 Experimental procedures

3.1 Sample preparation

3.1.1 Pre-alloy preparation

The BMG studied in this thesis, the so called Vit105, has a nominal composition of $Zr_{52.5}Ti_5Cu_{18}Ni_{14.5}Al_{10}$. In order to produce it, commercially pure elements (purity $\geq 99.99\%$) were cut in small pieces and ground using a grinding paper with the number 600. The weight of the constituting elements was measured using a Mettler Toledo AT200 with the accuracy of about 0.001 g. The pieces were then cleaned with Acetone in an ultrasonic bath for 15 minutes, followed by washing with distilled water and drying with air jet for 15 minutes.

3.1.2 Arc melting

Arc melting was used to produce master alloy ingots. The device uses an electrode in an argon atmosphere to heat the elements. The prepared elements (with weight of about 30 g) are placed inside the cavities in a water-cooled copper die. The temperature is adjusted via the machine current which varies from 0 to 280 A. The chamber is vacuumed to 10^{-5} - 10^{-6} mbar before being filled with Argon. A titanium getter ingot is also placed in one cavity and is melted, prior to the melting of elements, to absorb any oxygen present in the chamber. Each ingot was re-melted three times to ensure homogenous elemental distribution.

3.1.3 Centrifugal casting

The master alloy ingots produced via arc melting were cast into rectangular plates with the dimension of $30 \times 40 \times 1.6 \text{ mm}^3$ using centrifugal casting equipment. The machine is made of a large chamber with a rotating shaft. The shaft includes a small chamber with the copper mold and a graphite crucible in one end and an adjustable counter weight in the other end. The master alloy is placed inside the crucible and is heated via an induction coil. Two vacuum pumps of mechanical and molecular type are used to create a vacuum in the chamber with a pressure of 3×10^{-5} mbar. The chamber is then filled with argon with the pressure of 100 mbar. The master alloy is melted via increasing the current in the coil where its temperature is monitored via

an infrared-spectral pyrometer. The casting temperature was 1523 ± 15 K. The rotation is then started at 500 rpm which pushes the molten alloy into the rectangular cavity in the copper mold. The sample is cooled down in the argon atmosphere for 10 minutes. The produced samples were tested via differential scanning calorimetry and x-ray diffraction to assure that their structure is amorphous.

3.2 Characterization

3.2.1 Scanning electron microscopy (SEM)

The SEM uses a focused beam of high-energy accelerated electrons to generate a variety of signals upon hitting the surface of a conductive specimen. The typical signals used for imaging include back-scattered electrons and secondary electrons. Secondary electrons give information about the surface topography, while back-scattered electrons reveal contrast in composition in multiphase samples. The micro-structural features of the deformed BMG were observed using a high-resolution Gemini 1530 (Zeiss) SEM. Images were taken in the secondary electron mode, using an acceleration voltage of 5-20 kV, working distance of 10 mm and an aperture of $120\ \mu\text{m}$.

3.2.2 Nanoindentation

The nanoindentation technique is based on indenting the mirror polished surface of the specimen with a diamond indenter with defined shape and known hardness and Young's modulus. The indenter tip is usually a Berkovich type which has three-sided pyramid geometry. The test provides data points of indentation force versus indentation depth which includes loading and subsequent unloading stages. The hardness and reduced Young's modulus of the material can be extracted from these curves. The Hardness, H , is obtained by dividing the maximum force, F_{max} , by indentation area, A :

$$H = \frac{F_{\text{max}}}{A} \quad \text{Equation 3-1}$$

The maximum force used in this study was 8 mN. The reduced Young's modulus is calculated using following equation:

$$E_r = \frac{1}{\beta} \frac{\sqrt{\pi}}{2} \frac{(dF/dh)}{\sqrt{A(h_c)}} \quad \text{Equation 3-2}$$

where dF/dh is the slope of the unloading curve, β is a geometrical constant on the order of unity for a Berkovich type, and $A(h_c)$ is the projected area of the indentation at the contact depth, h_c [197]. An UMIS device from Fischer-Cripps Laboratories equipped with a Berkovich pyramidal-shaped diamond tip was employed in this thesis. The set-up includes an optical microscope in order to select a suitable site for indentation. The area in the cross section of the imprinted sample was scanned with 1500 indentations and had a size of $500 \times 1220 \mu\text{m}^2$. The test was performed at the Autonomous University of Barcelona (UAB) by Prof. J. Sort and Prof. M.D. Baro.

3.2.3 Tensile test

The drawing of the tensile sample used in this study is shown in Figure 3-1. The samples were made via spark wire cutting. The uniaxial tensile tests were carried out at room temperature using an INSTRON 5869 device under quasistatic loading with a strain rate of $1 \times 10^{-4} \text{ s}^{-1}$. The strain was measured by a computerized laser extensometer (Fiedler Optoelektronik GmbH) which measures the distance change between standard stripes being attached on the sample in the gauge length area.

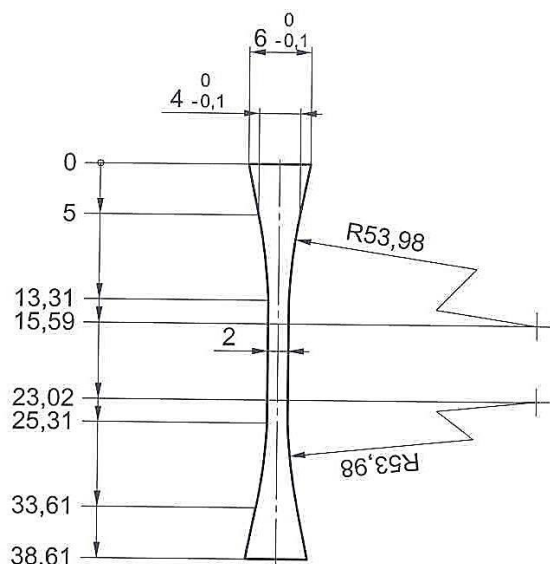


Figure 3-1 Drawing of the dog-bone shape tensile sample used in this study

3.3 High energy x-ray diffraction experiments

3.3.1 In-situ compression

In-situ x-ray diffraction during uniaxial compression of current BMG was performed at the P07 beam line at PETRA III (DESY, Hamburg, Germany) at ambient temperature using a Kammrath & Weiss GmbH mechanical test system with a maximum load of 5 KN at a nominal displacement rate of 1 $\mu\text{m/s}$. The XRD measurement was carried out in transmission mode with photon energy of 100 keV and a beam size of $250 \times 250 \mu\text{m}^2$. The sample with dimensions of $1.2 \times 1.15 \times 2.27 \text{ mm}^3$ was cut from the BMG plate. Sides of the sample were ground to remove surface defects. Both ends of the sample were carefully polished to make them parallel to each other prior to the compression tests. To support the plastic deformation, an Al foil was used as lubricant material between the loading platens and the sample as proved by Scudino et al. [159]. The measured force-displacement curve was corrected for the effect of foil and machine displacement. The XRD patterns were recorded every 5 seconds.

3.3.2 Analysis of mechanically-imprinted structure

In the imprinting method, a glassy sample (light-grey parallelepiped in Figure 3-2(a)) is placed between two imprinting hardened steel tools with a regular array of linear teeth with rounded profile (Figure 3-2 (b)). The load is then applied at room temperature along the Y-direction. As a result, a periodic pattern of linear imprints is created on the surface of the glass (Figure 3-2 (c)).

In order to perform the high energy x-ray diffraction test, the sample was cut along the cross-section of the imprinted plate (i.e. X-Y surface) and carefully ground to give a uniform thickness of 100 μm . A distance of 100 μm beneath the imprint line was chosen as the starting point of the diffraction patterns and marked with a Pt cube using FIB. The structure of the thin slice was investigated by XRD (see schematic representation of the XRD setup in Figure 3-2 (d)) in transmission using a high-energy monochromatic synchrotron beam ($E=63.32 \text{ keV}$) at the ID11 beamline of the European Synchrotron Radiation Facilities (ESRF). Diffraction patterns were collected every 10 μm along the X- and Y-directions using a rectangular beam with

size $5\ \mu\text{m} \times 150\ \text{nm}$, covering an area of about $800 \times 700\ \mu\text{m}^2$, which extends to about the midline of the imprinted plate. A total number of 5751 diffraction patterns, each with an exposure time of 1 second were recorded from the selected area. The first patterns were collected at a distance of about $100\ \mu\text{m}$ from the imprinted surface. The accurate position on the sample was ensured by the use of computer-controlled positioners with sub-micron precision encoders. For comparison purposes, as-cast homogeneous and heat treated samples were analyzed by XRD using the same parameters as used for the imprinted sample.

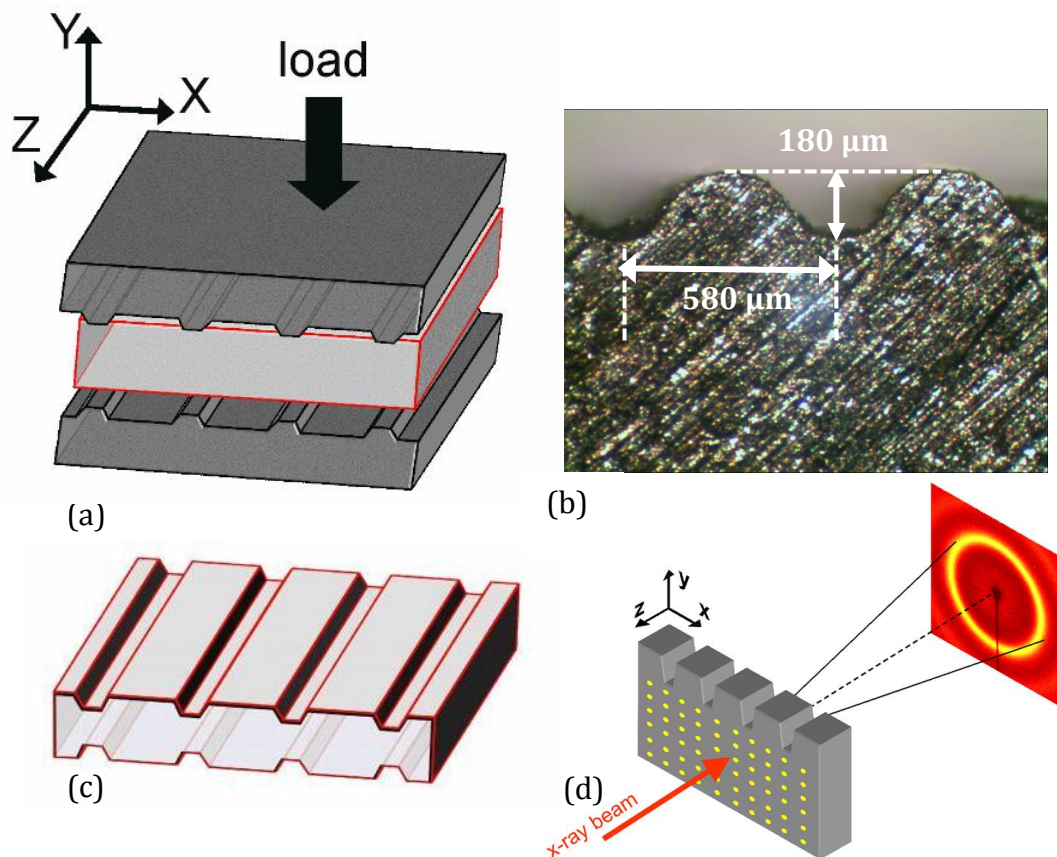


Figure 3-2 (a) Schematic representation of the imprinting method (b) Optical micrograph showing the details and dimensions of the imprinting tools (c) The regular array of wrenches after mechanical imprinting (d) x-ray diffraction experiment on the cross section of the imprinted sample

3.3.3 Single shear band analysis

The BMG sample used for shear band analysis had a thickness of 1.4 mm and a width of 3 mm. A laboratory hand operating rolling mill was used to roll the plate

continuously in one direction in very small steps to reach 5% of reduction in the thickness. Before rolling, one transverse side of the plate was mirror-polished. After rolling, the plate was ground from the opposite side to a thickness of $\sim 100 \mu\text{m}$ with twofold aim: i) to make it transparent for the nano-focused x-ray beam and ii) to have just one shear band on the x-ray passway.

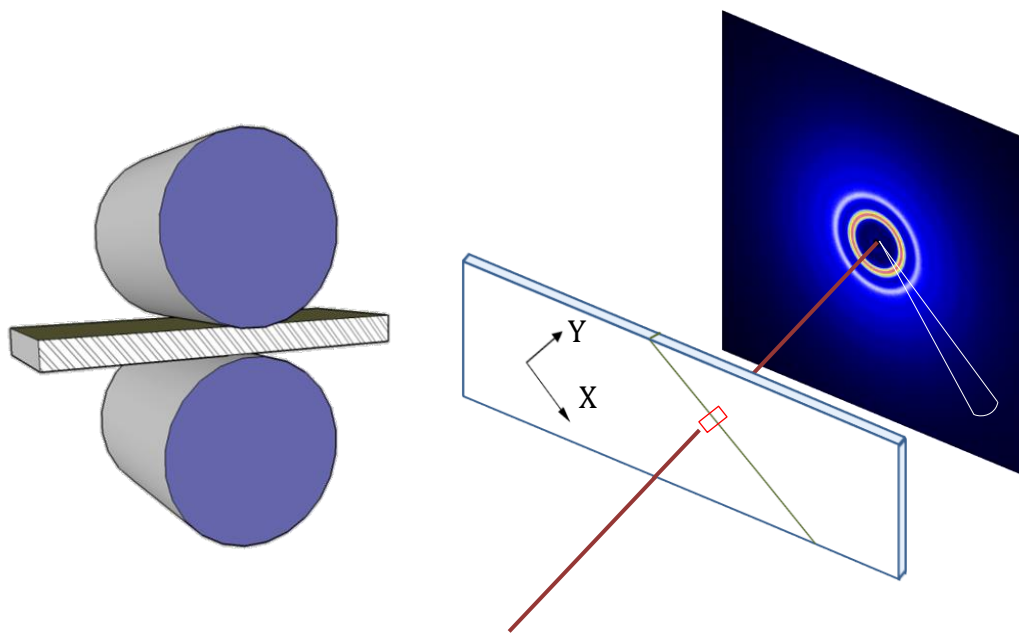


Figure 3-3 Schematics of the sample rolling and the x-ray diffraction experiment including alignment of the beam, sample, and the two-dimensional detector; the X and Y axis were chosen parallel and perpendicular to the shear band.

The schematic of the experiment is shown in Figure 3-3. Properly spaced shear bands in the cold rolled sample were chosen on the polished side using SEM. An area of $25 \times 45 \mu\text{m}^2$ was selected for the x-ray diffraction investigations and was marked with platinum dots of about $5 \mu\text{m}$ size deposited by a Focused Ion Beam (FIB). These dots were found with a fluorescence detector and were used as the guide points to limit the area of the XRD scan. The x-ray beam had a width of 150 nm , a height of $5 \mu\text{m}$, and a wavelength of 0.189 \AA . The exposure time for each diffraction pattern was 5 seconds. The selected area across the shear band was scanned with sample holder movements of 1.0 and $0.5 \mu\text{m}$ in the directions parallel and perpendicular to the shear band, respectively. A total number of 4538 diffraction patterns were obtained from the selected area.

3.4 Data processing

The collected data from 2D detector of high energy x-ray apparatus have to be processed for further analysis. In the first step, they have to be converted into $I(q)$ functions, which is the intensity of diffraction versus wave vector, q . For this purpose Fit2D package [198] was employed. The plane-parallel geometry of the samples enabled using the same data-treatment procedure for all azimuthal directions. The original diffraction data were calibrated by proper calibrant (CeO_2 for compression sample and platinum for other samples) measured at the sample position in order to: 1) refine the sample to detector distance, 2) correct the detector spatial distortion, 3) refine coordinates of beam center. The dead pixels of the detector were identified via accurate observation of a diffraction pattern and a proper mask was defined to eliminate their effect. In order to integrate the diffraction patterns, a macro was defined for processing the high number of patterns. It was used in two modes: 1) the data were integrated in the whole 2D diffraction pattern (360°) which gives the information on average structure in all directions, 2) each diffraction file was caked into 36 slices, each with angular width of 10° which has the advantage of supplying structural information in each desired direction. The reciprocal data were extracted from structure function, $S(q)$. For real space analysis, reduced pair distribution functions (PDFs), $g(r)$, were used. Transforming $I(q)$ functions into $S(q)$ and $g(r)$ was performed through PDFgetX3 package [199, 200]. The software uses ad-hoc approach to convert $I(q)$ into normalized structure function, $S(q)$, followed by sine Fourier transformation to obtain reduced pair distribution function (PDF) (see section 2.4.2). Before batch processing of whole data, the optimized parameters in order to get smooth structure function and reduced PDF with minimum termination ripples were obtained using PDFgetX3 package.

In order to compare the diffraction data obtained in in-situ compression test, the scripts were written in gnuplot software to fit the peak positions in the reciprocal space to Pseudo-Voigt function. This function is a combination of Gaussian and Cauchy functions. For real space analysis, the peak positions were identified via fitting to Gaussian functions. In the case of real space analysis of the data obtained

for the imprinted sample and the single shear band, the center of mass of peaks were obtained for strain calculations.

3.5 Calculation of strain tensor

In the reciprocal space, the corresponding strain values based on q_1 changes, \mathcal{E} , were calculated for each cake according to the following equation:

$$\mathcal{E} = \frac{q_1^{undeformed} - q_1^{deformed}}{q_1^{deformed}} \quad \text{Equation 3-3}$$

In real space, the strain was calculated from following equation:

$$\mathcal{E}_i = \frac{r_i^{deformed} - r_i^{undeformed}}{r_i^{undeformed}} \quad \text{Equation 3-4}$$

where r_i is the peak positions of i^{th} shell at reduced PDF.

In order to calculate the strain tensor components, the angular variation of the strain, obtained from 36 cakes is fitted to the following equation to obtain the \mathcal{E}_{xx} , γ_{xy} , \mathcal{E}_{zz} [201]:

$$\mathcal{E}_\theta = \mathcal{E}_{xx} \cos^2 \theta + \gamma_{xy} \cos \theta \sin \theta + \mathcal{E}_{yy} \sin^2 \theta \quad \text{Equation 3-5}$$

The maximum shear strain of each shell, γ_{max} , and its angle with the x axis, $\theta_{\gamma_{max}}$, were calculated according to the equations [202]:

$$\gamma_{max} = 2 \sqrt{\left(\frac{\mathcal{E}_x - \mathcal{E}_y}{2}\right)^2 + \left(\frac{\gamma_{xy}}{2}\right)^2} \quad \text{Equation 3-6}$$

$$\theta_{\gamma_{max}} = \theta_{\mathcal{E}_p} \pm 45^\circ \quad \text{Equation 3-7}$$

where $\theta_{\mathcal{E}_p}$ is the principal strain angle, obtained via following equation [202]:

$$\tan 2\theta_{\mathcal{E}_p} = \frac{\gamma_{xy}}{\mathcal{E}_x - \mathcal{E}_y} \quad \text{Equation 3-8}$$

3.6 Calculation of atomic packing density

In order to calculate the atomic packing density in a corresponding direction, the radial distribution function is calculated from reduced PDF according to the following equation [203]:

$$\text{RDF}(r) = r \cdot G(r) + 4\pi r^2 \rho_0 \quad \text{Equation 3-9}$$

where r is the atomic distance, $G(r)$ is the reduced PDF, and ρ_0 is the average atomic number density. The latter is obtained according to:

$$\rho_0 = \frac{\rho_{\text{BMG}} \cdot N_A}{M_{\text{BMG}}} \quad \text{Equation 3-10}$$

where ρ_{BMG} is the density of the BMG (measured as 6.68 gr/cm³ by archemidos experiment), N_A is the Avogadro constant (6.23×10^{23}) and M_{BMG} is the molecular weight of the BMG which is the weighted average of the molecular weights of elements in the BMG. The resulting average atomic density by replacing the corresponding values is 0.0551 atom/Å³.

4 Strain evolution during in-situ compression

4.1 Macroscopic stress-strain behavior

The room temperature macroscopic stress-strain behavior of the $Zr_{52.5}Ti_5Cu_{18}Ni_{14.5}Al_{10}$ BMG is shown in Figure 4-1. The sample displays an elastic strain of about 2% and yields at ~ 1450 MPa. The stress then increases with increasing strain to ~ 1650 MPa. The strain hardening-like regime is followed by a stress plateau up to about 22% strain, where strain softening occurs due to formation of a dominant shear band. As illustrated in the inset of Figure 4-1, the surface of the sample after fracture includes a high number of shear bands as the main cause of the large plastic deformation of this BMG [1].

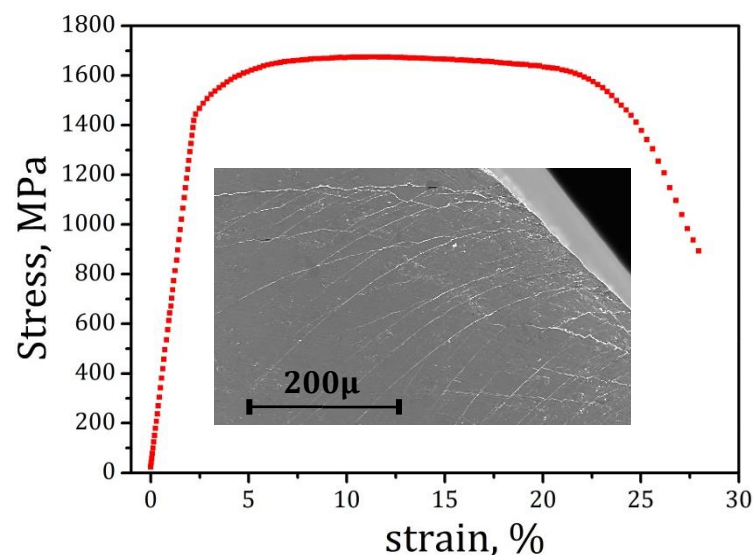


Figure 4-1 Macroscopic engineering compression stress-strain curve of the $Zr_{52.5}Ti_5Cu_{18}Ni_{14.5}Al_{10}$ BMG under elastostatic uniaxial compression. Inset is the image of the sample side after fracture, revealing the formation of a high density of shear bands.

4.2 Short-range order characterization

Principally, pair distribution function obtained by Fourier-transformation of a normalized scattering intensity gives information on the distribution of atoms around a given atom in real space in only one-dimension. However, by structural studies of isotropic non-crystalline materials, PDFs are used for description of the

spatial atomic distribution considering it as spherically symmetrical. Therefore atomic order in non-crystalline materials is characterized in terms of co-ordination shells, their radii and co-ordination numbers. This way, the short-range order is identified as composed by the atoms in the first nearest neighbor shell and is reflected by the main peak with a maximum probability in the PDFs at small r [203]. The higher coordination shells represent so-called medium range order (Figure 4-2(a)). The detail of atomic arrangement and chemical order at SRO for multicomponent Zr-based BMGs has not yet been fully understood. The direct observations with high resolution transmission electron microscopy (HRTEM) report that icosahedral-type atomic clusters exist in the structure of Zr-based BMGs [204, 205]. These observations were also confirmed by analysis of partial coordination numbers obtained via neutron and x-ray diffraction [206, 207] and simulations [37, 208] who suggested densely packed icosahedral clusters with solute atoms in the center as a model of atomic arrangement in multi-component BMGs.

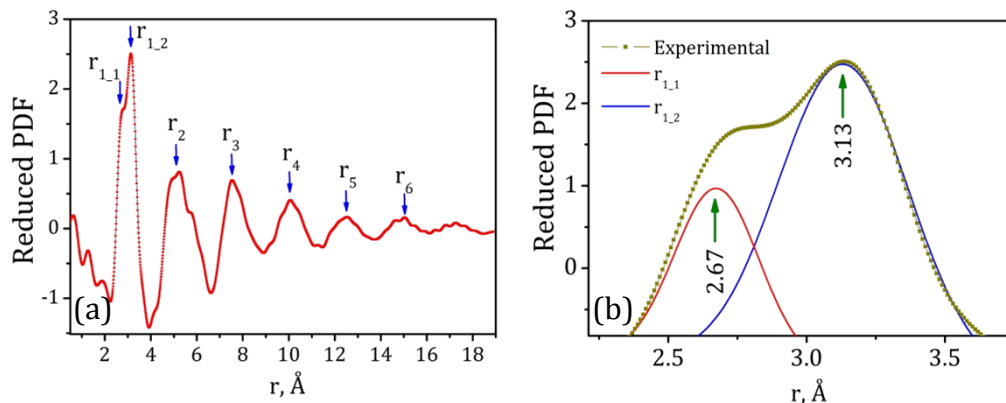


Figure 4-2 (a) Total reduced PDF for undeformed $Zr_{52.5}Ti_5Cu_{18}Ni_{14.5}Al_{10}$ metallic glass (b) The first main maximum of the PDF with fitted sub-peaks.

A part of the PDF corresponding to the SRO of the present BMG at $\sigma = 0$ is shown in Figure 4-2 (b). After fitting, it is evident that there are two sub-peaks with positions at 2.67 Å and 3.13 Å contributing to the main peak. A similar splitting of the first peak has also been reported by for multi-component Zr-based BMGs [209, 210] and binary systems [178]. Since this BMG contains five different elements (Zr, Cu, Ni, Ti and Al), ten types of atomic pairs between dissimilar atoms and five types of atomic

pairs between similar atoms exist. Al and Ti (metallic atomic radii of 1.43 and 1.46 Å, respectively, [211]) as well as Cu and Ni (1.28 Å and 1.25 Å, respectively, [211]) cannot be distinguished due to their very similar atomic radius. Due to the low scattering of Al and Ti [212], the (Cu,Ni)-Zr, Zr-Zr, and (Cu,Ni)-(Cu,Ni) atomic pairs make the dominant contribution to the PDF. The value of $r_{1,1} = 2.67$ Å is close to the average distance expected for (Cu,Ni)-Zr and (Cu,Ni)-(Cu,Ni) atomic pairs (2.69 Å). This means that (Cu,Ni)-Zr and (Cu,Ni)-(Cu,Ni) atomic pairs might contribute to the peak at $r_{1,1}$. The second sub-peak on the PDF at $r_{1,2} = 3.13$ Å is in good agreement with the length of the Zr-Zr bond, 3.10 Å [211] and it obviously reflects the Zr-Zr pairs.

4.3 Variation of atomic packing density

It is clear that the coordination number cannot be calculated by integration of the RDF function for an anisotropic material as the assumption of spherical symmetry is not valid there. This is also true for uniaxially-deformed metallic glasses. However, the area under the first peak of a RDF might give useful information on the atomic packing in a corresponding direction.

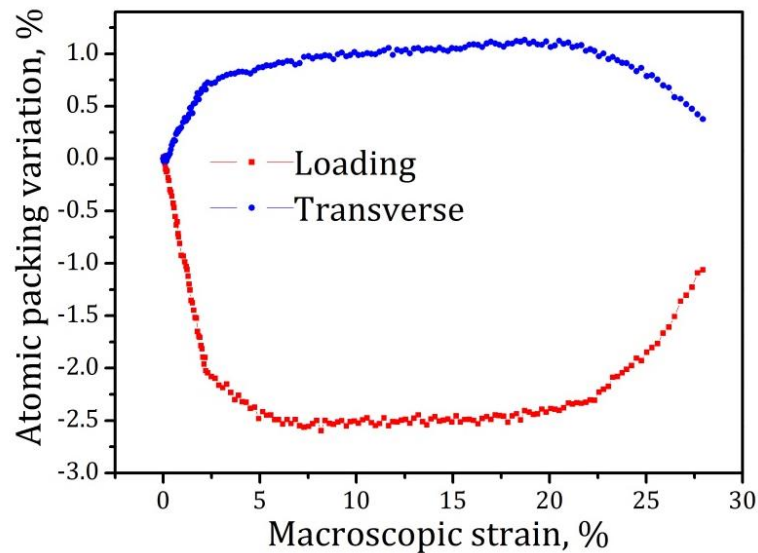


Figure 4-3 Variation of the area under the first peak of the radial distribution function versus macroscopic strain in the transverse and loading directions.

Figure 4-3 shows the relative change of atomic packing for the present BMG as a function of the macroscopic strain along the loading and transverse directions. In the transverse direction it increases by about 0.7% within the elastic regime and then continues to increase with slower rate up to the beginning of the macroscopic softening (compare with Figure 4-1). Afterwards, it starts to decrease until the fracture occurs. In contrast, at loading direction the atomic packing indicates a linear decrease of about 2% up to the elastic limit, followed by a moderate decrease until macroscopic strain of 7%. Afterwards, it stays constant until the beginning of softening and finally increases upon approaching fracture.

Although the changes in the atomic packing values are small, they clearly indicate atomic rearrangement during deformation. Since the values start to approach to the initial points after the beginning of softening, these rearrangements seem to be mainly reversible. The opposite trend of the changes in two directions in the elastic regime indicates that upon compressive deformation, a small fraction of bonds in the first neighborhood atoms are broken at the loading direction and inversely, some new bonds are formed in the transverse direction. This is in agreement with structural rearrangements reported in two directions for the Cu-Zr BMGs under compressive loading [7, 195]. It is also worth to note that this experiment does not measure the atomic rearrangements in the direction parallel to the beam. However, it is reasonable to suppose that the changes in the plane perpendicular to the loading direction are isotropic. Considering this point, one can realize that the atomic packing changes in the transverse direction are smaller than in the loading direction.

4.4 Atomic displacements during elasto-plastic deformation

In Figure 4-4(a), the atomic strain values extracted from $r_{1,1}$ and $r_{1,2}$ (i.e. the SRO) and r_5 as a representative peak of the MRO are displayed versus macroscopic engineering stress for the loading and transverse directions. In addition, in order to show how the atomic strains are changing in the different stages of elastic and plastic (hardening, plateau and softening) deformation, the evolution of atomic-scale strain along the loading and transverse directions are plotted in Figure 4-4(b)

versus the macroscopic strain for the $r_{1,2}$ and r_5 shells as representatives of SRO and MRO, respectively.

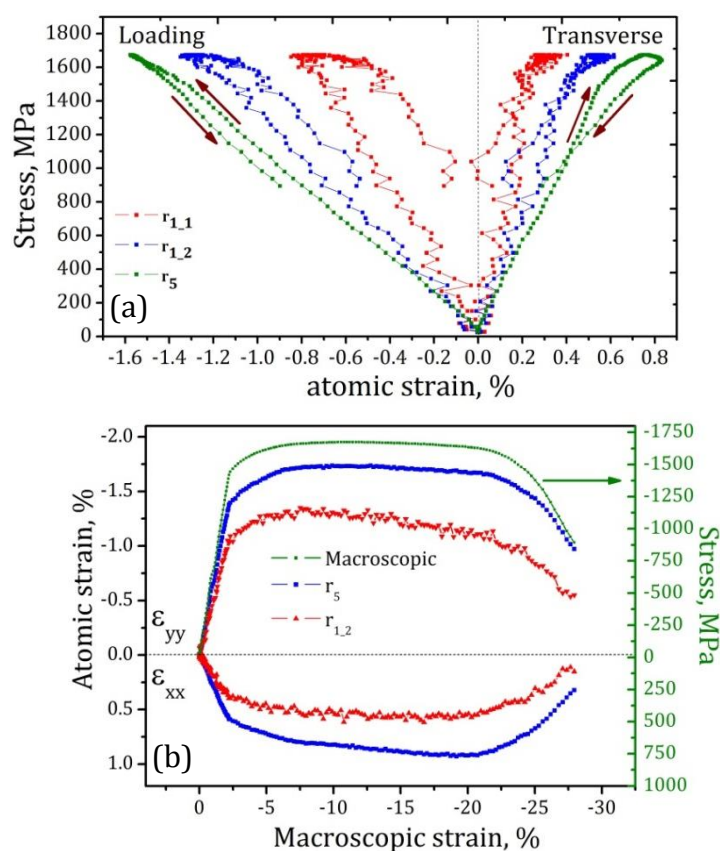


Figure 4-4 (a) loading ϵ_{yy} and transverse ϵ_{xx} strains for the peaks at $r_{1,1}$, $r_{1,2}$ (SRO) and r_5 (MRO) versus macroscopic compressive stress, (b) Macroscopic stress-strain curve and atomic strains versus macroscopic strain in the two directions for SRO and MRO.

4.4.1 Elastic deformation

From Figure 4-4(a), one can observe for both SRO and MRO that in the elastic regime up to ~ 1450 MPa the compressive strain (negative) in the loading direction and tensile strain (positive) in the transverse direction increase linearly with increasing stress. The linear correlation between atomic strain and applied stress for the SRO and MRO is in agreement with the findings of several groups studying the deformation of BMGs via high energy x-ray diffraction [7, 177, 181, 210, 213].

The loading ϵ_{yy} strain at the elastic limit is about -0.7% for $r_{1,1}$ and -1.1%, for $r_{1,2}$. This indicates a higher stiffness of the (Cu,Ni)-Zr and (Cu,Ni)-(Cu,Ni) atomic pairs, resulting in the least contribution to the observed elastic deformation

of the SRO. This is in agreement with the model proposed by Ma et al. [206, 214], where the Zr-(Cu,Ni) pairs are highly rigid against external forces with respect to the more compliant Zr-Zr pairs. The strain value of r_5 at the macroscopic elastic limit is about -1.4%. Similar results are obtained for the other MRO shells, i.e., r_2 , r_3 , r_4 and r_6 (not shown in the figure). The calculated averaged Poisson's ratio of the shells from r_2 to r_6 confirm the rigidity of SRO compared with MRO. The average Poisson's ratio of MRO shells is about 0.42, which is considerably higher than that of the SRO shells (0.36). Furthermore, the average Young's modulus of the MRO is 105 GPa, whereas it is 197 GPa for $r_{1,1}$ and 127 GPa for $r_{1,2}$. These observations clearly indicate that the SRO bonds are much stiffer against external loading compared to MRO. The easier deformation of MRO shells can be attributed to the free volume sites distributed mainly between clusters, while the atomic arrangement inside the clusters is efficiently packed and rigid [214]. Compared to the macroscopic Young's modulus of this BMG, 88 GPa [215], both the SRO and MRO shells are considerably stiffer. Coupled with the observed atomic density variations, such a large discrepancy confirms the point mentioned by other groups [7, 178] that the elastic behavior of BMGs is not only governed by simple compression of the atoms/clusters but also other structural mechanisms like rearrangement of atoms/clusters might contribute to the elastic atomic displacement of the BMGs.

4.4.2 Plastic deformation

The stress-strain correlation of the MRO shells (e.g. r_5) along the loading and transverse directions starts to deviate from linearity at 1.4% (Figure 4-4(a)) which corresponds to the macroscopic elastic limit of this BMG occurring at 2%. This suggests that yielding may be correlated with structural changes involving atomic displacements in the MRO. The non-linear correlation of the atomic strain versus stress beyond the elastic limit has also been reported by other groups [196, 213]; however, so far it has not been addressed in detail. It is known that the main mechanism of plastic deformation in BMGs occurs by propagation of shear bands that have been nucleated from topologically unstable STZs [54]. Such STZs are found mostly in the high free volume regions [216]. Theoretical calculations [75], molecular dynamics simulations [76] as well as experimental nanoindentation test analysis [77, 217] suggest that the size of STZ ranges from tens of atoms to several

hundred atoms. This implies that the STZs may nucleate in both SRO and MRO. In order to interpret the deviations of the MRO strain observed at the macroscopic yielding, one can imagine the arrangement of clusters with a free volume region between them, as illustrated in Figure 4-5(a).

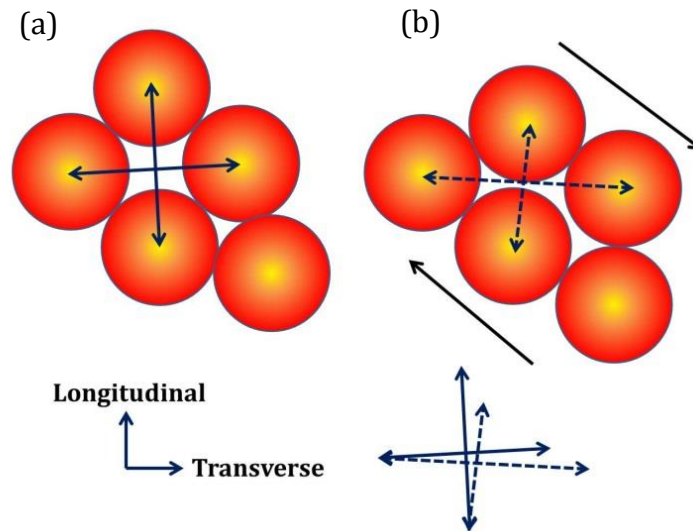


Figure 4-5 Schematic illustration of how the inter-cluster distances are changed when an STZ in the MRO is formed by the induced shear stress.

The MRO spacing in two perpendicular directions have been depicted with arrows between the clusters. As indicated in Figure 4-6(a), with onset of the elastic deformation, the maximum shear strain γ_{\max} starts to increase for all length scales (SRO and MRO). The resolved maximum shear stress/strain acts normally in the plane oriented at 45° with respect to the loading direction [201]. γ_{\max} of the MRO reaches about 0.020 at the yield point and then it saturates at 0.026 (Figure 4-6(a)), which is in very good agreement with the value reported by Johnson and Samwer for the critical value of shear strain for an individual STZ (0.0267 ± 0.0020) [218]. This suggests that a deviation of atomic strain-stress curve from linearity can present a qualitative measure of STZ formation in the beginning of plastic deformation. Nevertheless, the current method averages the information on a scattering volume of $250 \times 250 \mu\text{m}^2$ which is large enough to include thousands of STZs. Thus, extracting the mean size or distance between nucleated STZs requires knowledge on at least the number of activated STZs in the scattering volume.

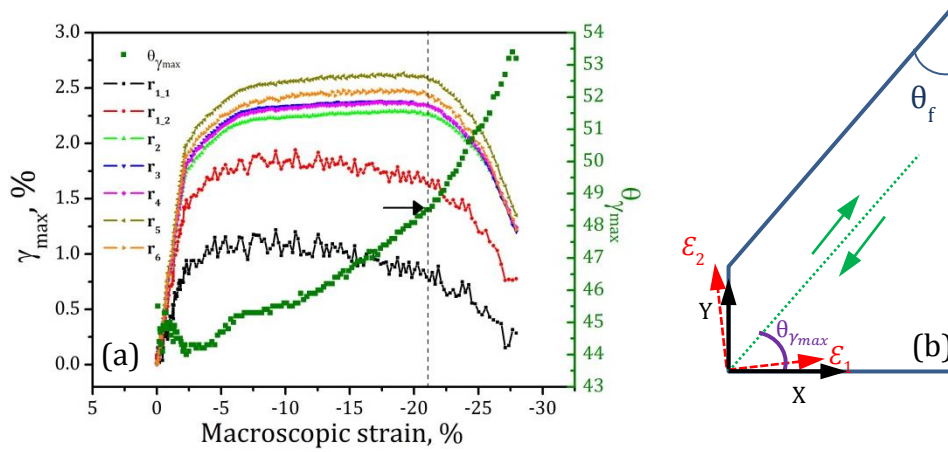


Figure 4-6 (a) variation of γ_{max} and $\theta_{\gamma_{max}}$ at different length scales against macroscopic strain, the dashed line indicates the beginning of macroscopic softening. (b) schematics of $\theta_{\gamma_{max}}$ occurring between two principal strains and is supplementary to the fracture angle, θ_f .

According to Figure 4-5(b), the corresponding shear stress acting in the maximum shear strain plane will rotate and slide a layer of the clusters in this direction to rearrange them from topologically unstable positions into a more stable position with decreased inter-cluster distances in the loading direction and increased in the transverse direction, as illustrated by the length of perpendicular arrows, in agreement with the observations in Figure 4-4(a). The increasing rate of γ_{max} is weaker with increasing stress and becomes almost saturated before softening (Figure 4-6(a)), probably because the STZs are combined to form shear bands acting as a source for triggering next shear bands which will drive further plastic deformation.

Considering the different values of γ_{max} for different coordination shells in the plastic deformation regime, it is clear that γ_{max} of SRO is considerably smaller compared to MRO indicating that SRO has the least contribution to the shear transformation. It is also evident that γ_{max} is significantly smaller for $r_{1,1}$ compared with $r_{1,2}$ (Figure 4-6(a)). Correspondingly, the amount of the deviation of ϵ_{xx} and ϵ_{yy} after elastic limit is considerably smaller for the $r_{1,2}$ than for the $r_{1,1}$ (Figure 4-4(a)). This can be an indication that Zr-Zr pairs have a larger contribution to the shear transformations compared to the Zr-(Cu,Ni) or (Cu,Ni)-(Cu,Ni) pairs. It is also worth

to note that among the all MRO coordination shells, r_5 has the largest γ_{\max} implying that the clusters at this length scale have the largest contribution to the STZs.

In Figure 4-6(a), the change of the angle $\theta_{\gamma_{\max}}$ for the MRO is plotted versus the macroscopic strain. While $\theta_{\gamma_{\max}}$ oscillates around 45° in the elastic regime, it deviates from this value with starting of macroscopic plastic deformation, reaching about 48.5° at the beginning of softening (indicated by an arrow in Figure 4-6(a)), i.e. at the formation of the major shear band. Therefore, according to the schematic representation in Figure 4-6(b) the potential fracture angle (θ_f) deviates from 45° towards smaller angles, reaching a value of $90^\circ - 48.5^\circ = 41.5^\circ$. This value is in very good agreement with the macroscopic observations for the fracture angle of this BMG under uniaxial compression, which occurs at about 42° [219]. It is also worth to note that, the calculated $\theta_{\gamma_{\max}}$ increases also after the beginning of softening up to the fracture. This is due to a higher decreasing rate of ϵ_{xx} (consequently $\epsilon_{xx} - \epsilon_{yy}$) compared to γ_{xy} (Figure 4-4(b), Eq. (6)). However, once γ_{\max} determines the formation of the major shear band at $\theta_{\gamma_{\max}} = 48.5^\circ$, the deformation proceeds along this direction and the $\theta_{\gamma_{\max}}$ cannot alter the direction of the major shear band.

4.4.3 Softening

The beginning of the macroscopic softening of the BMG is due to the formation of one major shear band that localizes the entire macroscopic deformation, reduces the required deformation force, propagates slowly [120] and finally results in the fracture of the BMG. In order to understand the details of the softening, one should consider that the x-ray beam passes from the whole scattering volume of the sample and the diffraction patterns reflect structural information of the volume which includes the major shear band and the two detaching parts. Considering that the thickness of the shear band is negligible compared to the thickness of the detaching parts, the diffraction data include mainly structural information occurring in the two detaching parts. When a major shear band forms, the compressive force is essentially localized by a very thin ($\sim 10\text{nm}$) shearing region and the two detaching parts of the sample experience a decrease of the macroscopically induced load. This means that as the softening continues, these parts may reverse the elastic and anelastic structural changes that have occurred during the preceding deformation.

This is well illustrated in the behavior of the SRO and MRO strains versus macroscopic strain beyond $\sim 22\%$ in Figure 4-4(b), where both ϵ_{xx} and ϵ_{yy} are approaching zero with increase of the macroscopic strain in the softening stage. This phenomenon can be also observed in Figure 4-4(a) where the softening stage in the loading and transverse directions is indicated by downward arrows. In the loading direction, in particular for the MRO, the slope of the stress-strain curve in the softening stage is very similar to that of the elastic loading (indicated with an upward arrow). This suggests that the structure of the detaching parts is not irreversibly altered during plastic deformation of the glass. On the other hand, the rate of softening of the MRO in the transverse direction (Figure 4-4(a)) is much smaller than that of the corresponding elastic loading part. This can be attributed to some irreversible structural changes that have occurred in this direction during deformation, irreversibly altering the structure.

4.5 Length scale dependence of atomic strains

In Figure 4-7(a)-(b), ϵ_{xx} and ϵ_{yy} have been plotted at several values of stress in the elastic and plastic deformation regimes versus the length scale, r . It can be observed that there is a steep increase of atomic strain from SRO to MRO in both elastic and plastic regimes of deformation, in agreement with other reports [21, 173]. In the different MRO shells, the atomic strains are almost similar in the elastic regime. However, at the stress level near the yield strength, (1418 MPa), as well as in the plastic deformation regime, (1671 MPa), one can observe that the strain extracted from r_5 at 12.5 Å is higher compared to the other MRO shells. A characteristic MRO length scale with higher strain was also reported by Hufnagel et al. [173] at 12-13 Å for $Zr_{57}Ti_{15}Cu_{20}Ni_{18}Al_{10}$ BMG under compressive loading and attributed to the reported STZ size of about 10 Å [220]. Our observation in Figure 4-6(a), where the peak of r_5 indicated the largest γ_{max} supports the idea that this length scale has the highest contribution to the shear transformations underlying the main mechanism of plastic deformation of BMGs.

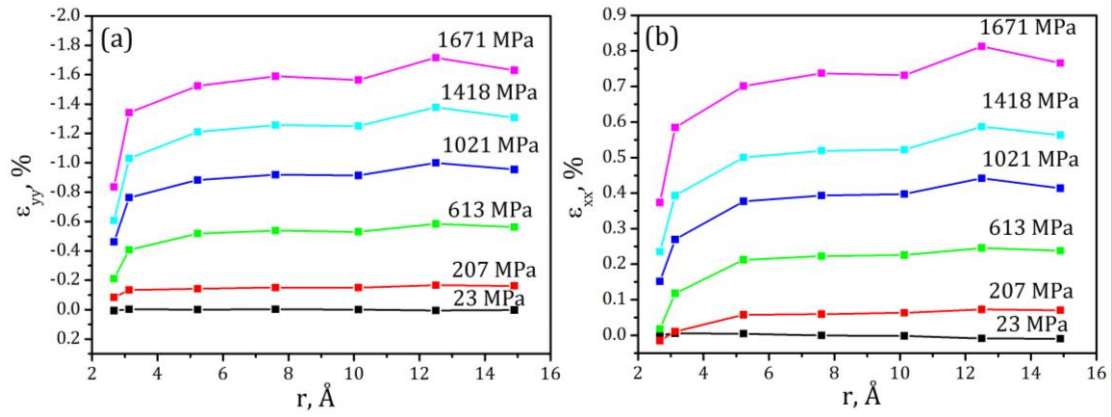


Figure 4-7 (a) ϵ_{yy} and (b) ϵ_{xx} at several stress levels as a function of interatomic distance (r), revealing the length scale dependence of the strain.

4.6 Summary

The results of this chapter can be concluded as follows: In the elastic regime, the atomic distances at SRO vary linearly with macroscopic stress. Analysis of the area under radial distribution function indicates that a small fraction of bonds in the first shell is broken in the loading direction whereas some new bonds are formed in the transverse direction. Atomic bonds at SRO appeared significantly stiffer than the MRO shells. Compared to the macroscopic values of elastic strain, Young's modulus and Poisson's ratio, both SRO and MRO appeared significantly stiffer implying that the elastic behavior of the BMG is not only governed by simple compression of the atoms/clusters but also is aided by rearrangement of atoms/clusters. The deviation of MRO atomic strain-stress correlation from linearity at the onset of plastic deformation was attributed to the activation of irreversible STZs as illustrated by strong shear strain value at the onset of yielding. This value is in a good agreement with reported value of the critical shear strain needed for activation of an irreversible STZ. The length scale of 12.5 Å indicated the largest shear strain and is thought to be the most effective length scale in the formation of STZs. On the other side, the atomic pairs at SRO with smallest shear strain have the least contribution to the STZs. It is also indicated that the typical fracture angle of this BMG can be explained by the orientation of maximum shear strain at the onset of major shear band formation.

5 Strain distribution in mechanically-imprinted BMG

5.1 Microstructural features

The mechanical imprinting of $Zr_{52.5}Ti_5Cu_{18}Ni_{14.5}Al_{10}$ BMG consists of surface plastic deformation carried out through pressing of the sample between two jagged tools as described in detail in chapter 3. This method has been proven to be effective for enhancing the room-temperature tensile ductility of brittle metallic glasses and represents a flexible tool for the generation of designed plastically-deformed regions with optimized length scale [9].

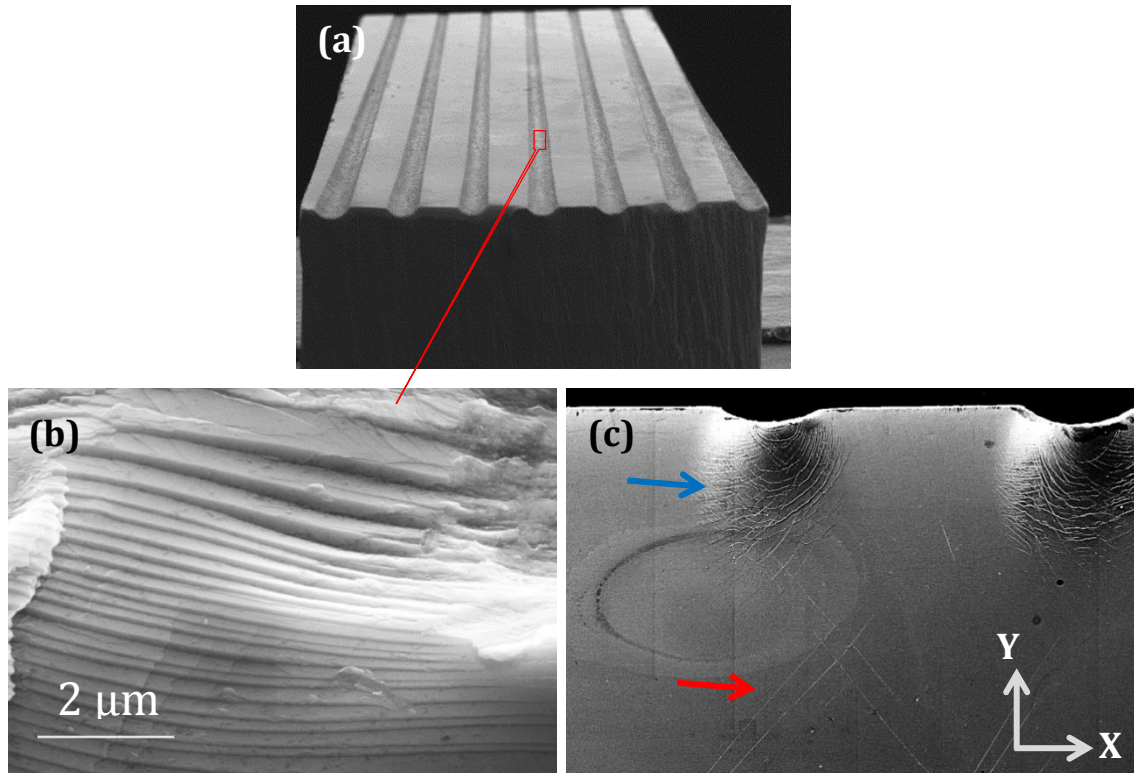


Figure 5-1 a) The SEM image of the $Zr_{52.5}Ti_5Cu_{18}Ni_{14.5}Al_{10}$ BMG sample after imprinting. b) The wrenches in the surface of treated sample include a high density of shear steps. c) The cross section of the imprinted sample including two different types of shear bands

As a result of imprinting, a periodic pattern of linear imprints is created on the surface of the glass (Figure 5-1 (a)). The intensive deformation at imprints in the surface proceeds via a high density of shear steps (Figure 5-1 (b)) created via semi-circular shear bands beneath the imprints (blue arrow in Figure 5-1 (c)). Such kind of shear bands have been already observed during indentation of metallic glasses [221]. In addition, imprinting generates another distinct type of the shear bands on the cross-section of the imprinted samples (i.e. X-Y surface) forming an angle of about 45° with the loading Y-direction (indicated by a red arrow in Figure 5-1 (c)).

5.2 Effect of imprinting on tensile properties

In Figure 5-2, the room temperature true stress-strain curves of the $Zr_{52.5}Ti_5Cu_{18}Ni_{14.5}Al_{10}$ BMG have been plotted for three different cases. The curve for as cast sample (black curve) indicates that the untreated sample displays no plasticity and breaks immediately after the elastic limit at 1746 MPa. The imprinted sample (red curve) indicates 1.5% of plastic deformation after yielding at 1635 MPa. This illustrates the capability of the current mechanical treatment in enhancing the plastic deformation under tensile loading. As illustrated in the blue curve, the observed plasticity vanishes upon annealing of the imprinted sample at 623 K for 10 min. This implies that the structural changes made via mechanical treatment are reversible upon proper heating.

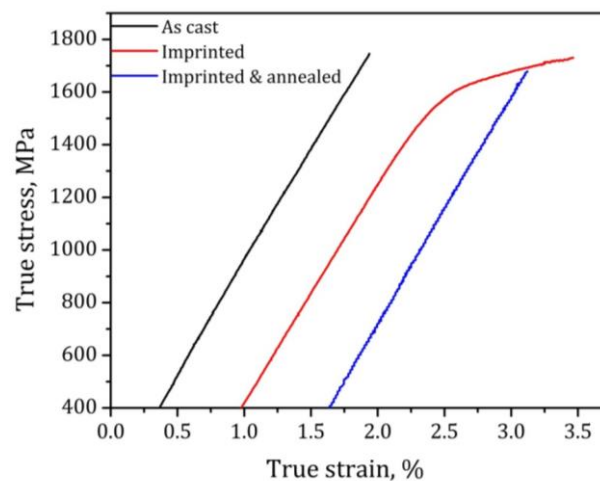


Figure 5-2 True stress-strain curves for as-cast, imprinted, and imprinted and annealed BMG samples

The observed brittle behavior of the current BMG in the as-cast status is typical for BMGs and is one of the most important obstacles for commercializing these novel materials. There has been a few number of reported studies which address treatments to enhance tensile plasticity in monolithic BMGs [165, 222]. Although the observed plasticity is not large enough for practical forming processes, it is indicating that the BMGs can be treated to deform plastically under tensile loading. Moreover, the reversibility of the brittleness upon heat treatment bears a high importance from a metallurgical point of view since it creates an opportunity for making high plastic deformations on BMGs via repeated imprinting and annealing of the structure. In the next sections, the structure of the imprinted BMG sample is studied with high resolution two-dimensional maps of inter-atomic distances, hardness and Young's modulus to find out varying mechanical properties and atomic correlations in the cross section of mechanically-treated BMG.

5.3 Heterogeneous structure characterized by nanoindentation

The nanoindentation test is capable of probing the local elastic and plastic properties of materials with high spatial resolution. Using this technique, in Figure 5-3(a)-(b), the maps of hardness and Young's modulus variation have been obtained and indicated for an area of $450 \times 1250 \mu\text{m}^2$ in the cross section of the imprinted sample. The data points have been obtained with a spatial resolution of $10 \mu\text{m}$ in X direction and $50 \mu\text{m}$ in Y direction. The hardness values represent the local response of the BMG to permanent deformation while the Young's modulus value is correlated with the resistance of atomic bonding to elastically deviate from equilibrium distance [223]. As it is shown in Figure 5-3(a), the hardness values are regularly changing in the cross section under the imprints. The regions between the imprints have higher hardness with respect to the regions beneath them (9.6 GPa versus 7.2 GPa). Compared to the average hardness value of the untreated as-cast sample, 8.2 GPa, it is clear that a regular pattern of hardened and softened regions has been evolved due to the mechanical imprinting. As it was shown in Figure 5-1, the region under the imprint is severely deformed and includes a high density of semi-circular shear bands. The reduced hardness at these regions can be attributed to the strain softening which occurs at shear bands [224]. The increased hardness at

the region between the imprints might be due to compressive residual stresses which have been created due to the compressive state of the stress in these regions, as it was suggested by others [25, 26].

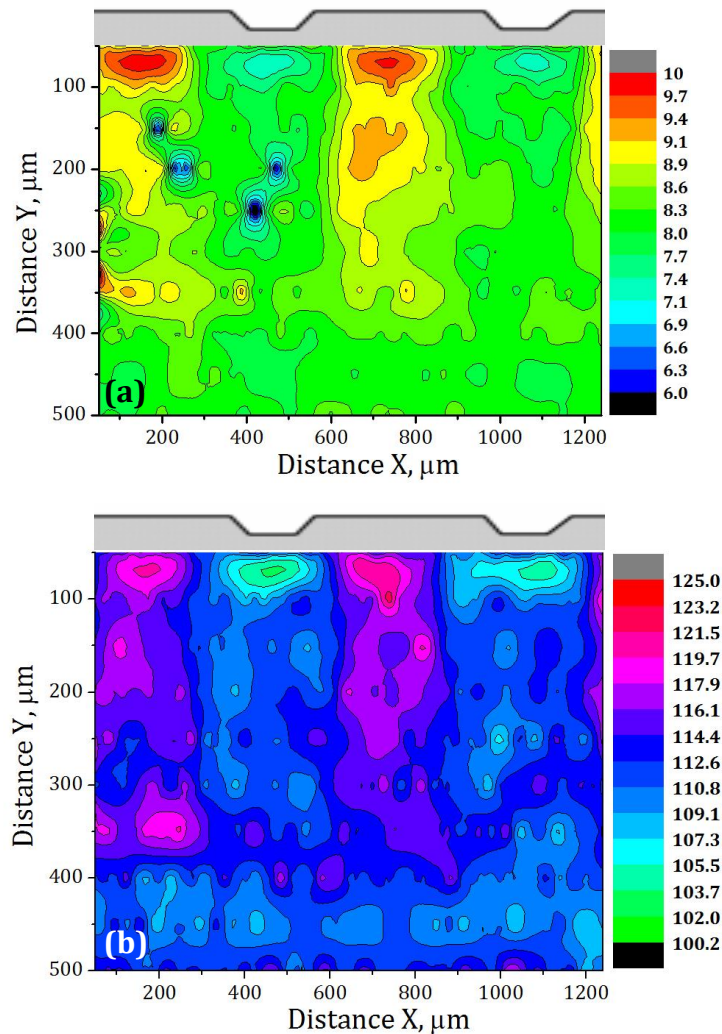


Figure 5-3 Map of variation of a) hardness (GPa) and b) Young's modulus (GPa) in the cross section of mechanical treated sample under the imprints

The map of Young's modulus (E) distribution has been illustrated in Figure 5-3 (b). It is clear that the structure has been altered at least 400 μm beneath the surface. Similar to the map of hardness, oscillating values for regions under and between the imprints can be also observed for E. Compared to the measured average value of E in the undeformed as-cast sample (114.8 GPa), the regions between the imprints are stiffer while the regions under them are softer than the undeformed state. The altered modulus in the imprinted sample suggests that the interatomic distances

might have been changed upon deformation. In other words, there exists a network of residual elastic strains/stresses which affects further the tensile behavior of the BMG. In the next sections, this aspect of the structure, i.e., the altered interatomic distances due to plastic deformation, is studied using maps obtained by high energy x-ray diffraction.

5.4 Detection of heterogeneities via high energy x-ray diffraction

As mentioned in the previous chapters, the first maximum of the x-ray intensity or structure function taken from a metallic glass, and in particular the position of the first peak q_1 , carries significant information on amorphous structure and can be approximately considered as inversely proportional with the interatomic distances [203, 225]. Figure 5-4 (a) illustrates the map of q_1 of the structure function in the cross section of an as-cast Vit105 BMG. It should be noted that reported q_1 values in this figure have been obtained from full integration of the diffraction patterns and represent no preferential directional distances. It is clear that q_1 is distributed nearly homogeneously with the values oscillating at $2.624 \pm 0.003 \text{ \AA}^{-1}$. This suggests that interatomic distances in the as-cast structure are uniformly distributed in the structure. In Figure 5-4 (b), a similar map is shown for the cross section of the imprinted and polished sample. q_1 values under the imprinted surface are significantly larger than the average q_1 in the as-cast sample suggesting that the plastic deformation has resulted in a decrease of the average interatomic distances in these regions. Furthermore, the map in Figure 5-4 (b), in agreement with hardness and modulus maps, shows a very heterogeneous distribution, ranging from 2.643 \AA^{-1} to 2.668 \AA^{-1} . The regions under the imprints indicate the most pronounced changes compared to the regions between the imprints which is simply due to the high degree of deformation in those regions. The change of inter-atomic distances becomes weaker in the regions far from the imprinted surface. Comparing the q_1 values in the regions between the imprints with the region beneath a wrench, one can conclude that interatomic distances beneath the wrench are smaller and may present higher hardness and Young's modulus. This is apparently in contradiction with the observed values for such regions in nanoindentation maps shown in Figure 5-3. However, one should consider that the current experiment, contrary to

the nanoindentation tests, does not probe the structural changes at the direction Z (perpendicular to the cross section). Therefore, it is only possible to report variations in 2-D coordinates. The behavior of material against nanoindentation tip would be affected by structural distances at three directions of which only two directions will be discussed in the next sections.

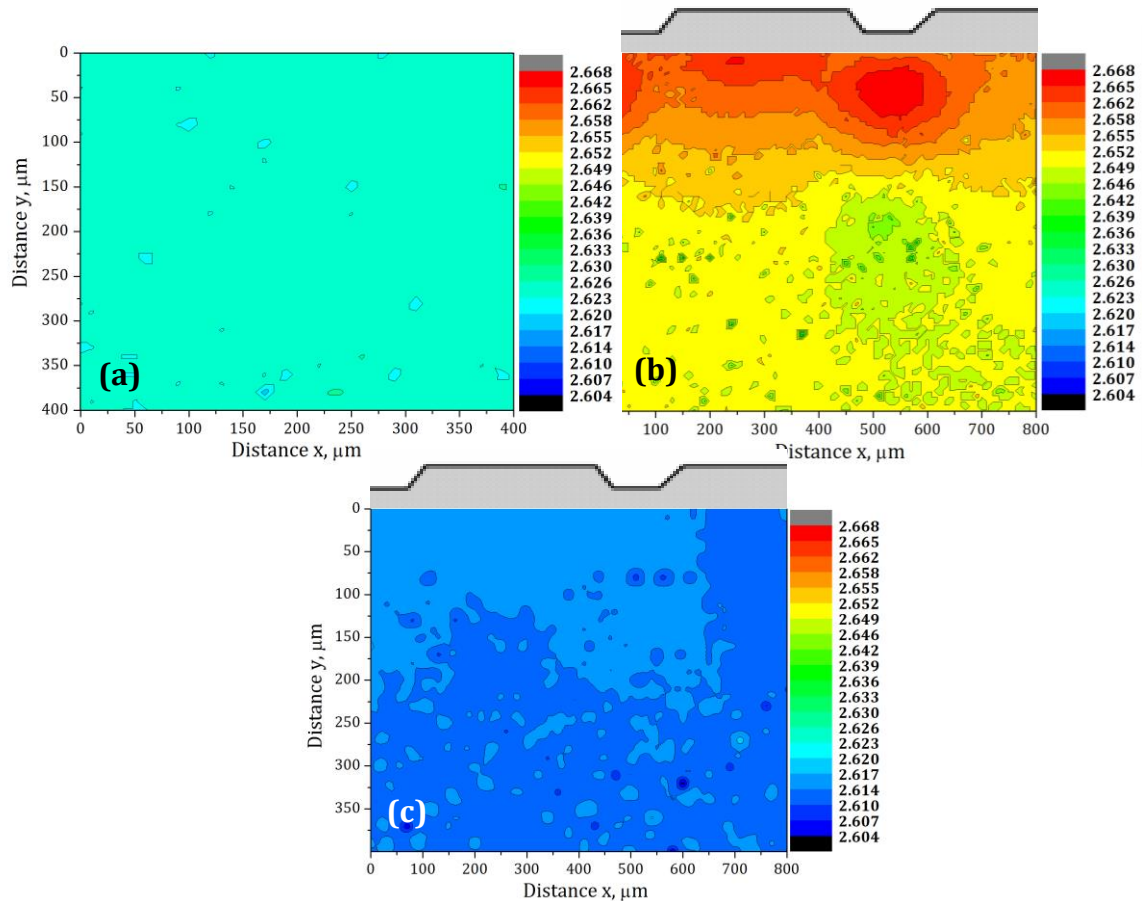


Figure 5-4 Map of variation of $q_1(\text{\AA}^{-1})$ in the structure function as an indication of the MRO in the cross section of the a) as-cast sample, b) imprinted sample, and c) imprinted and heat treated sample

In Figure 5-4 (c), a similar map for the imprinted and heat treated (623 K, 10 min) sample has been indicated. It is clear that the heterogeneous structure has been significantly reduced as a result of heating. The average q_1 value (2.613\AA^{-1}) has been recovered nearly to the average value seen in the as-cast sample (2.624\AA^{-1}), most probably as a result of relaxation of amorphous structure. Considering the stress-strain curves indicated in Figure 5-2, the current maps highlight the critical role of

the generated heterogeneities via imprinting to enable the tensile ductility in the BMG.

5.4.1 Strain tensor based on q_1 variations

Knowing the values of q_1 one can calculate the components of the strain (including ϵ_x , ϵ_y and γ_{xy}) and principal strains (ϵ_1 and ϵ_2), and the maximum shear strain (γ_{max}) in the cross section of the imprinted BMG plate by using the equations mentioned in chapter 3. The distribution map of the strain tensor components at X-Y coordination, corresponding to the loading direction and the transverse direction have been illustrated in Figure 5-5. In Figure 5-5 (a), the strain component at direction X, ϵ_x has been shown. By moving from the surface to the center of the plate, ϵ_x changes from the compressive to tensile mode. This might be due to the restrictive mode of the deformation created via imprinting tool on the surface of the plate while the central part is not restricted and can deform easier in the X direction with respect to the surface regions. In the regions close to the surface, the structure under the imprints exhibits larger compressive strain field (reaching to about 1.5%) compared to the regions between the imprints. In the case of the ϵ_y , the strain component along the loading direction (Figure 5-5 (b)), by moving from the surface to the center of the plate it changes from tensile to compressive mode. The map of shear strain in the X-Y plane displays a mixture of positive and negative shear strains which are mainly beneath the imprints. The regions between the imprints as well as in the middle of the plate represent a negligible amount of shear strain.

In Figure 5-6 (a)-(b), the distribution maps of the principal strains, ϵ_1 and ϵ_2 , have been shown in the cross section of the imprinted BMG plate. The principal strains are defined as strains in the directions in which no shear strain exists. For each point in the map, ϵ_1 and ϵ_2 are the largest and smallest normal strain components, respectively. According to Figure 5-6 (a), ϵ_1 is compressive almost all over the cross section with the largest values close to the imprinted surface which gradually diminishes as it approaches to the center of the plate, reaching to a compressive strain values less than 0.3%.

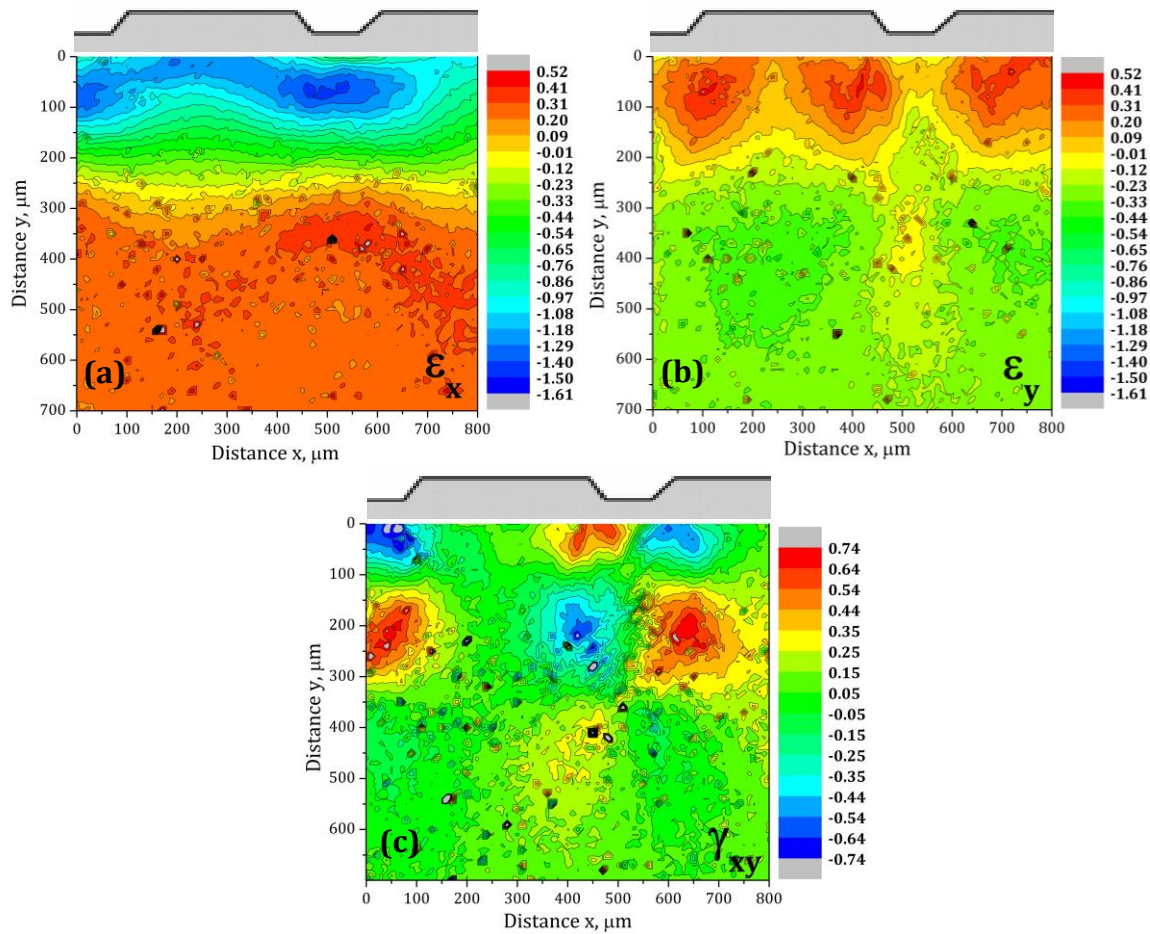


Figure 5-5 The strain map of imprinted BMG extracted from q1 for a) strain at direction X, ϵ_x b) strain at direction Y, ϵ_y c) shear strain, γ_{xy} .

On the other side, as it is shown in Figure 5-6 (b), the other principal strain, ϵ_2 , indicates tensile strain fields of less than 0.3% close to the center of the sample while it includes a sequence of compressive and tensile strain fields close to the imprinted surface. It can be seen in this graph that beneath the imprint at the range of $Y=100-250 \mu\text{m}$ ϵ_2 is in compressive in a relatively large area. The other principal strain, ϵ_1 , is also compressive in the same areas (see Figure 5-6 (a)). Having two compressive principal strains beneath the surface can act very effectively in blocking the propagating shear bands. In Figure 5-6 (c), the distribution map of maximum shear strain has been indicated for the same area in the cross section of imprinted sample. The areas close to the imprinted surface in the corner of imprinted and unimprinted area have the highest residual shear strain reaching to about 1.8%.

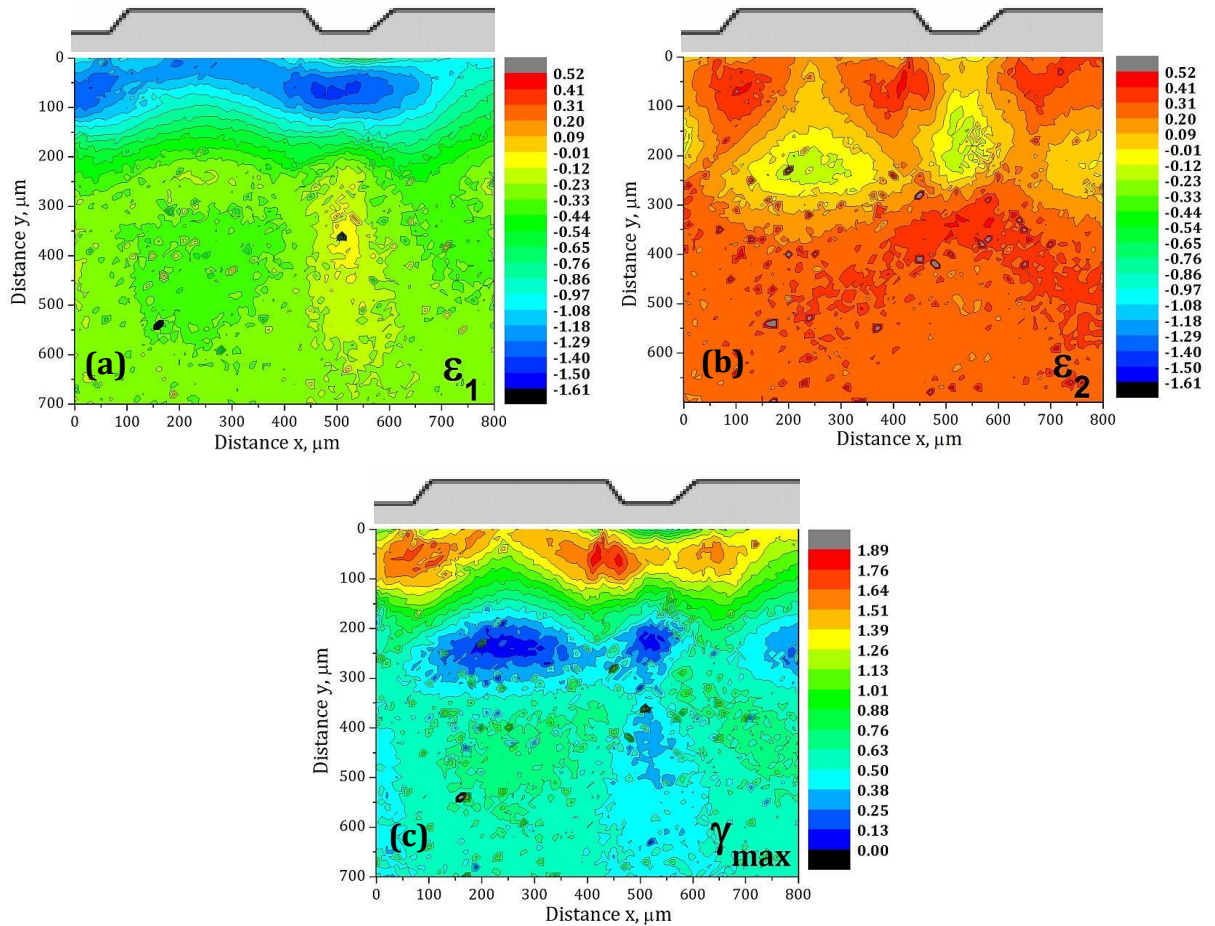


Figure 5-6 Distribution map of principal strains including a) ϵ_1 b) ϵ_2 and c) maximum shear strain, γ_{max} .

As it was mentioned in section 4.4.2, once the maximum shear strain reaches the critical value of shear strain for an individual STZ (0.0267 ± 0.0020) [218], the STZs can coalesce to form shear bands resulting to the plastic deformation of the BMG. The observed residual shear strain is close to the critical value and may act as the potential point of nucleation for shear bands upon deformation. Interestingly, a clear evidence of both above-mentioned phenomena, i.e., the blockage of propagating shear bands at the imprinted region and the propagation of new shear bands from the border of imprinted and un-imprinted region has been illustrated with an SEM image of a BMG plate with 45° imprints subjected to tensile loading at Figure 5-7. The red oval indicates a shear band which has propagated from the tensile sample side and has started to branch once it has reached to the imprint. The observation is in agreement with finding of Scudino et al. for imprinted samples under tensile loading [9]. Moreover, the blue oval illustrates a series of the shear bands which

have nucleated from the corner of imprinted and un-imprinted regions. This finding highlights the significant role of the maximum shear strain characterized from spatial strain maps in nucleation of the shear bands and improvement of the plasticity.

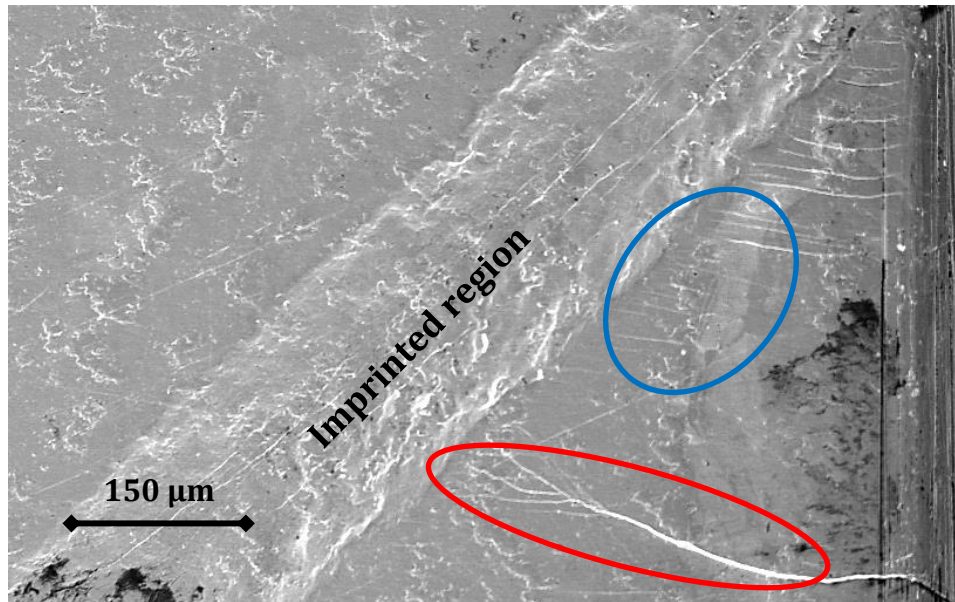


Figure 5-7 An imprinted sample subjected to uniaxial tensile deformation illustrates shear bands nucleated from the interface of imprinted and un-imprinted region (blue oval) and shear bands that are stopped and branched at upon reaching to imprinted area (red oval)

5.5 Summary

The tensile plasticity of the mechanically-imprinted Vit105 BMG plate reveals a clear improvement with respect to the as-cast sample. The proper heat treatment of the heterogeneous structure makes it again brittle in the tensile loading. The hardness and Young's modulus probing of the cross section of the imprinted sample indicated oscillating soft and hard regions have been created beneath the surface due to imprinting. The high energy x-ray scanning of the cross section of the imprinted plate via a nano-size beam revealed a heterogeneous structure in q_1 distribution where there was no significant change of q_1 in the cross section of the as-cast plate. The heat treatment vanishes the heterogeneous structure and rolls it back nearly to the undeformed state. The analysis of the strain tensor components based on q_1

changes, revealed that ϵ_x changes from the compressive to tensile mode going from the surface to the center of the plate. Beneath the surface, ϵ_x reaching to values about 1.5% under the imprints and indicates larger compressive field with respect to the region between the imprints. Close to the imprinted surface, at regions between the imprints ϵ_y is tensile while the structure beneath the imprints and regions far from the sample are in compression mode at Y direction. The distribution of principal strains indicated that both ϵ_1 and ϵ_2 are compressive the imprint which results in blocking/deflecting of the propagating shear bands in agreement with SEM observation of shear banding in tensile samples. Moreover, the region beneath the border of the imprinted and un-imprinted parts has the highest residual shear strain. Microstructural observations indicate that such points nucleate new shear bands upon tensile loading.

6 Residual strain around a single shear band

The obtained spatial strain maps of the heterogeneous structure indicated in the last chapter demonstrated that the plastic deformation via macroscopic shear banding affects both sheared and intact regions. This suggests that the shear banding might affect the distances far from its core. In order to investigate this, a single shear band was chosen in a cold rolled structure in $Zr_{52.5}Ti_5Cu_{18}Ni_{14.5}Al_{10}$ BMG plate. The nano-focused high energy x-ray diffraction was used to map the shear band area to reveal the variation of residual normal and shear strains at SRO and MRO on a nanoscale resolution.

6.1 Microstructure

The rolled sample contains a sequence of parallel shear bands oriented at an angle of $\pm 45^\circ$ with respect to the rolling direction (SEM image in Figure 6-1(a)). In Figure 6-1(b) the area including the single shear band has been illustrated in higher magnification. The scanned area has been marked with a red rectangle with small lines. One of the platinum markers deposited around the shear band is seen at the bottom-right.

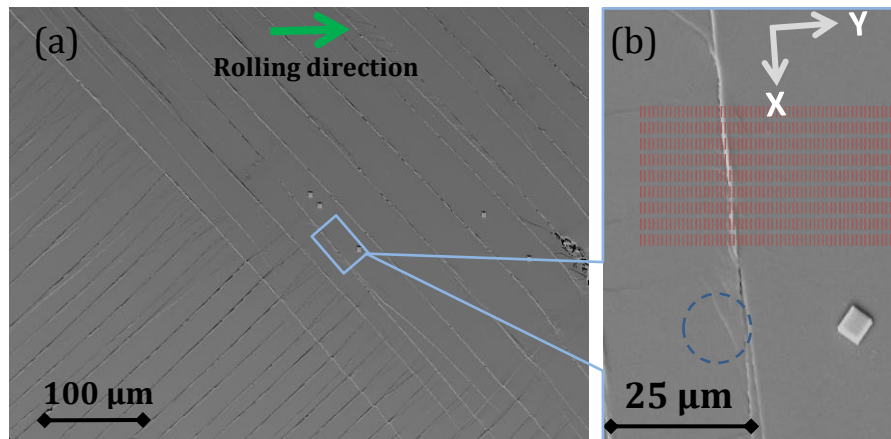


Figure 6-1 (a) Scanning electron microscopy (SEM) image of the cold rolled structure in $Zr_{52.5}Ti_5Cu_{18}Ni_{14.5}Al_{10}$ BMG plate, (b) The studied single shear band; the blue circle marks a secondary shear band while the red rectangle depicts the scanned area. One of the platinum markers deposited around the shear band is seen at the bottom-right.

The so far reported experimental evidences of the shear-induced zone in Zr-based metallic glasses are related to the single shear bands with large shear offsets which are responsible for catastrophic failure of the sample [30, 31]. In contrast, our current observations quantify the diffusive residual strain fields around a non-catastrophic mature shear band with small shear offset, formed during the plastic deformation of the metallic glass.

6.2 Reciprocal space mapping

It is known that the first maximum of the x-ray intensity or structure function taken from a metallic glass, and in particular the position of the first peak q_1 , carries significant information on amorphous structure [226]. Poulsen et al. [5] showed that the components of the strain tensor in uniaxially deformed metallic glass can be determined from the positions of q_1 measured over all azimuthal directions with respect to the incident beam. The x-ray intensities, as illustrated in Figure 6-2, indicate a fully amorphous structure with no trace of crystallinity, implying that the studied region is free from deformation- or heating-induced crystallization.

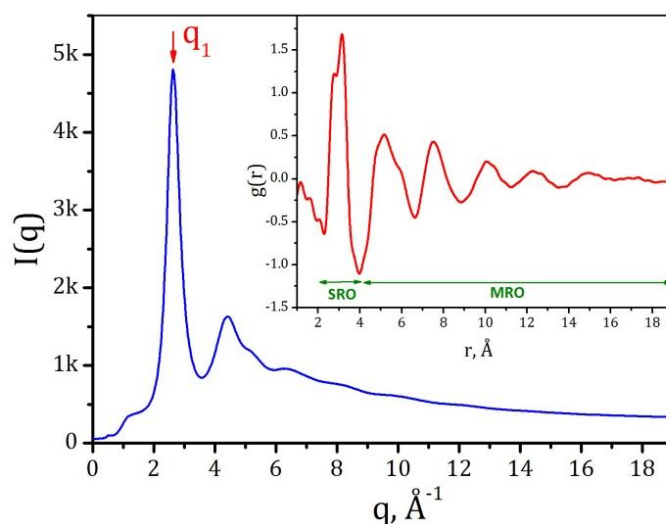


Figure 6-2 Example of the integrated x-ray diffraction intensity versus wave vector (q) and reduced PDF (inset).

The variation of the first peak on the XRD intensities over the whole scanned area across the shear band was determined via fitting. The corresponding maps for the fully integrated diffraction patterns and the XRD intensities measured in the planes

along and perpendicular to the shear band are plotted in Figure 6-3(a). The map of q_1 extracted from the fully integrated patterns reveals an asymmetric gradient with respect to the shear band plane which diversely affects the atomic structure in the area around the shear band.

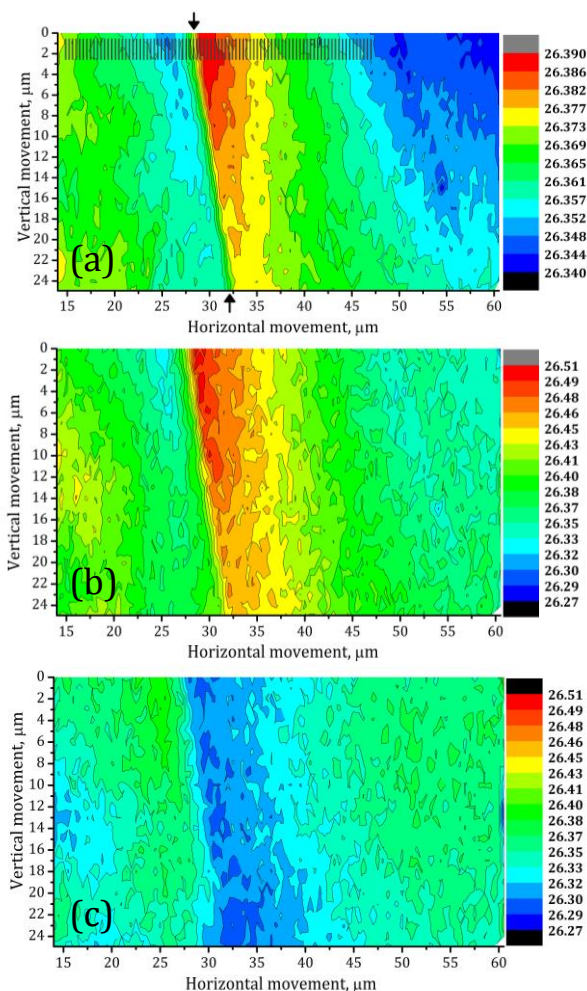


Figure 6-3 Variation of the position of the first maximum of XRD intensities q_1 ($1/\text{nm}$) taken from the area containing a single shear band: (a) fully integrated diffraction patterns; (b) measured along the shear band; (c) measured perpendicular to the shear band. All three maps reveal that the atomic structure is essentially affected over rather large distances from the shear band. The arrows in panel (a) mark the shear band. The vertical lines across the shear band in panel (a) mark the area from which the data plotted in Fig. 3 were extracted.

The maps of q_1 for the diffracted intensities at directions along and across the shear band in Figure 6-3(b) and (c) represent more pronounced variations over the

scanned area. This is a clear indication of a directional heterogeneity of the inter-atomic distances as a result of shear banding.

6.3 Residual strain at SRO and MRO

Analysis of the pair distribution functions (Figure 6-2, inset) was performed along a line crossing the shear band, as indicated in Figure 6-3(a). Figure 6-4(a) and (b) present the profiles for the residual strains, ϵ_x , ϵ_y and γ_{max} determined from the first peak of the reduced PDF at about 2.9 Å, representing the nearest-neighbors shell, and from the fourth peak at about 10.1 Å, representing medium-range order. It is clearly seen that the residual strains spread over distances of more than 15 μm from the shear band. Together with the maps for q_1 in Figure 6-3, this is surprisingly challenging the “localized” nature of the shear strain in a very narrow region (10-20 nm) of the shear band [1, 93, 119].

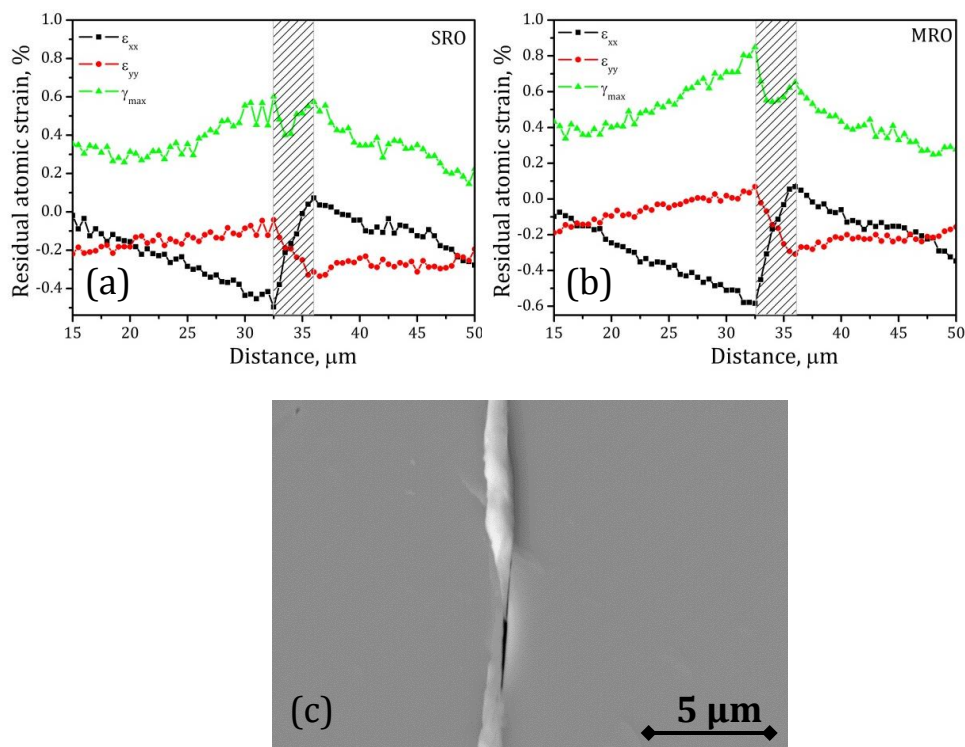


Figure 6-4 Residual normal (ϵ_x and ϵ_y) and shear (γ_{max}) strain profile along the direction crossing the single shear band at (a) SRO, and (b) MRO, (c) The soft sheared material flows out of the shear band in the as-deformed BMG.

The so far reported experimental evidences of the shear-induced zone in Zr-based metallic glasses are related to the single shear bands with large shear offsets which are responsible for catastrophic failure of the sample [30, 31]. In contrast, our current observations quantify the diffusive residual strain fields around a non-catastrophic mature shear band with small shear offset, formed during the plastic deformation of the metallic glass. Similarly to the q_1 maps in Figure 6-3, the normal strains indicate an asymmetric distribution with respect to the shear band line. According to Figure 6-4(a) and (b), in the very vicinity of the shear band, the residual normal strains have opposite signs at the two sides of the shear band and the change from tensile to compressive strain occurs at the core of the shear band. The altered interatomic distances at x and y direction result in a residual shear strain component, γ_{\max} , in the shear band and nearby regions. Contrary to the normal strains, γ_{\max} has a quasi-symmetric distribution with respect to the shear band with a maximum at the shear band and declining at farther distances. Such distribution of the residual shear strain is in good agreement with similar profiles of hardness [30, 31] and elastic modulus [31] across a single shear band in Zr-based BMGs. This suggests that compared to the residual normal strains, the residual shear strain field plays a dominant role in controlling the plastic deformation of the metallic glass.

There is a characteristic core region of about $3.5 \mu\text{m}$ width around the shear band (shaded rectangles in Figure 6-4(a) and (b)) which indicates an abrupt change in the normal strains. Correspondingly, γ_{\max} at both SRO and MRO exhibits a small local minimum in the middle of this region. A closer look at the SEM image with the shear band (Figure 6-4(c)) reveals material which has flown out of the shear band. This suggests that a necessarily soft amorphous region has been formed at the shear band during deformation. Together with the observed characteristic core zone for the residual strain fields, this is believed to represent the liquid-like/hot-zone region in a single shear band proved via melting of a thin tin layer by Lewandowski and Greer [81].

The maximum shear strain during deformation of bulk metallic glass is a crucial parameter in determining the nucleation of irreversible STZs. The critical shear

strain needed to form an irreversible STZ is estimated as $\gamma = 0.0267$ [218]. Obviously, having the largest γ_{\max} at the very vicinity of the main shear band, explains the formation of secondary shear bands from the main shear band as it is seen, for example, in Figure 6-1(b). Comparing the γ_{\max} values for the SRO and MRO (Figure 6-4(a) and (b)) reveals that the residual strain is larger on the MRO distances. This is in agreement with the length scale dependence of the atomic strain in BMGs, as reported previously by others [189, 210, 227].

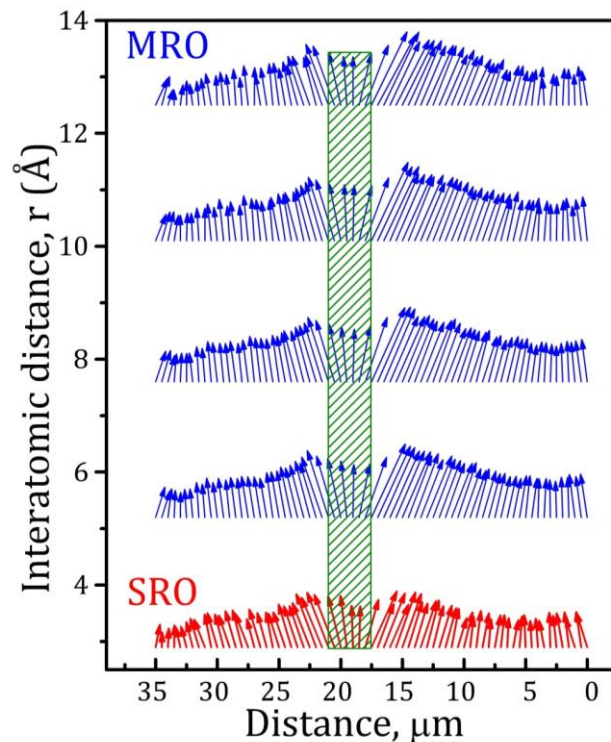


Figure 6-5 Vectors of the residual maximum shear strain, γ_{\max} , in and around a single shear band at different length scales (SRO and MRO) of the deformed BMG along the line crossing the shear band. The length of the vectors represents the relative magnitude of the shear strain.

Figure 6-5 shows the vectors of γ_{\max} calculated along the line crossing the shear band, as indicated in Figure 6-3(a). The magnitude of the vectors is proportional to the absolute values of γ_{\max} while their directions are shown relative to the angle of γ_{\max} . The direction of γ_{\max} in the shear band core (green shaded area) is parallel to the shear band for the short-range and medium-range interatomic distances. It is worth to note that when getting far from the center of the core region, the maximum shear strain direction deviates from the shear band plane and reaches an average

angle of about $\pm 24^\circ$ at the border of the core region where the residual shear strain has its maximum value. This is in very good agreement with the direction of the observed secondary shear bands (Figure 6-1(b)) which nucleate from the main shear band under an angle of $\sim 25^\circ$ with respect to the main shear band. In addition, a similar pattern of displacement vectors, obtained by molecular dynamics simulations, has been recently reported [228]. Overall, this proves the decisive role of the quantified residual shear strain in triggering the further plastic deformation of BMG via nucleation of new shear bands in the shear affected zone around a mature shear band. This presents an atomic scale demonstration to confirm the previous reports which noted an improved tensile and compressive plastic deformability of the cold rolled BMGs [12, 14, 137, 160, 161].

6.4 Summary

The nano-beam high energy synchrotron x-ray diffraction probing of the residual strains distribution around a single shear band in a cold rolled Zr-based BMG revealed interesting structural features at both SRO and MRO length scale. The plastic deformation results in diffusive residual normal and shear strain fields extending over distances more than $15 \mu\text{m}$ away from the shear band. The residual normal strains exhibit an asymmetric distribution whereas the residual shear strain is distributed symmetrically at the sides of the shear band. In agreement with reported distributions of elastic constants and hardness across a shear band, the results highlight the dominant role of the shear strain in governing further plastic deformation at regions near the shear band. This is also proved by the coincidence of the direction of the nucleating secondary shear bands from the main shear band with the orientation of the residual shear strain at the vicinity of the mature shear band.

7 Conclusion and outlook

The aim of this thesis was to investigate the structural features occurring during elasto-plastic as well as after plastic deformation in Vit105 BMG. The most important feature was the atomic-scale strain which was studied in short and medium range order of the structure by using high energy synchrotron x-ray.

The in-situ study of the Vit105 BMG in uniaxial compression revealed that the critical shear strain plays the main role in plastic deformation of current BMG. In the elastic regime, the atomic distances at SRO vary linearly with macroscopic stress. A small fraction of bonds in the SRO is broken in the loading direction whereas some new bonds are formed in the transverse direction. Atomic bonds at SRO appeared significantly stiffer than the MRO shells. Compared with macroscopic elastic response of the BMG, both SRO and MRO appeared significantly stiffer implying that the elastic behavior of the BMG is not only governed by simple compression of the atoms/clusters but also is aided by rearrangement of atoms/clusters. A strong shear strain component was identified at the onset of yielding which is assumed to activate irreversible STZs and cause deviation of MRO atomic strain-stress correlation from linearity at the onset of plastic. The length scale of 12.5 Å indicated the largest shear strain and is thought to be the most effective length scale in the formation of STZs. On the other side, the atomic pairs at SRO with smallest shear strain have the least contribution to the STZs. The identified maximum shear strain at the onset of major shear band formation could predict well the typical fracture angle of this BMG in compression.

The high energy x-ray scanning of the cross section of the mechanically-imprinted Vit105 BMG plate via a nano-size beam provided high resolution spatial maps obtained from the reciprocal space data. These maps revealed a heterogeneous structure which includes residual tensile and compressive strain fields. Accordingly, the spatial maps of the hardness and Young's modulus in the cross section indicated strong heterogeneity (oscillating soft and hard regions) compared to the undeformed sample. The residual strain fields were disappeared upon heat treatment resulting in the brittle behavior of the BMG upon tensile loading. The distribution of

principal strains indicated that both ε_1 and ε_2 are compressive under the imprints which results in blocking of the propagating shear bands in tensile loading. Moreover, the region beneath the corner of the imprinted and un-imprinted regions has the highest residual shear strain which favors nucleation of new shear bands upon tensile loading, in agreement with microstructural observations of evolved shear banding in the tensile loading of imprinted samples.

The probing of the area around a single shear band in cold rolled BMG plate via nano-focused high energy x-ray beam revealed that the plastic deformation results in diffusive residual normal and shear strain fields extending over the distances more than 15 μm away from the shear band. The residual normal strains exhibit an asymmetric distribution whereas the residual shear strain is distributed symmetrically at the sides of the shear band. The results highlight the dominant role of the shear strain in governing further plastic deformation at regions near the shear band. This was also proved by the coincidence of the direction of the nucleating secondary shear bands from the main shear band with the orientation of the residual shear strain at the vicinity of the mature shear band.

Overall, the results of this thesis not only provide a direct experimental evidence of the effects of plastic deformation on the atomic structure of metallic glasses, but also contribute to the understanding of how one can positively influence the formation and propagation of shear bands in order to mitigate the room temperature brittleness of bulk metallic glasses.

In the following, some further ideas to extend the knowledge on the deformation of BMGs are listed:

The understanding of atomic scale structural features during tensile plastic deformation of the BMG is still missing. The main obstacle has been the lack of tensile plasticity in monolithic BMGs. With the aid of treatments like imprinting, and using optimized imprinting parameters, higher amounts of tensile plastic deformation might be reachable. This provides the opportunity for detailed understanding of tensile plastic deformation by performing in-situ tests with high energy x-ray.

The strain analysis on mechanically imprinted BMG plate was done on X-Y plane which was the transverse direction to the imprints. Analysis of strain tensors in X-Z and Y-Z planes which are parallel to the imprint lines can provide a 3D representation of strain in the imprinted sample. This will help to study the strain states for all types of shear bands propagated in different planes in the heterogeneous structure upon tensile loading.

The reported results in this thesis were based on analysis of the high energy x-ray data according to the approach of Poulsen et al. [5] which assumes that BMGs deform isotropically at small strains and provides a quantitative estimate of the atomic strains. Another approach which is developed by Suzuki et al. [189] assumes that the deformation of the BMGs is anisotropic at short length scales and involves non-affine atomic displacements created by strong shear stresses. Analysis of the available data on the plastically deformed BMGs based on the second approach would elaborate the differences between two approaches and would improve the understanding of deformation-induced atomic rearrangements particularly at the short range order.

Acknowledgement

First of all, I would like to express my sincere gratitude to Prof. Jürgen Eckert for providing me a great opportunity to be a part of his research group at IFW Dresden and for his kind support during the last four years. During my doctorate, I learnt from him not only a lot in the research but also a variety of great lessons on generosity and humanity. I also appreciate the very helpful suggestions of Dr. Sergio Scudino in shaping up the present dissertation.

My sincere thanks for the support, encouragement, help as well as the pleasant time during the time of my doctorate to:

Dr. I. Kaban, Dr. M. Stoica, Dr. U. Kühn, B. Escher, Dr. H. Wendrock, Dr. J. Bednarcik, Dr. G. B. M. Vaughan, Dr. S. Menzel, Dr. H. Turnow, M. Frey, S. Donath, B. Bartusch, Dr. U. Rütt, Dr. M. S. Khoshkhoo, F. A. Javid, Dr. K.G. Prashanth, Dr. A. Taghvaei, M. Bönisch, M. Bierdel, Dr. K. Song, Prof. P. Gargarella, K. Kosiba, Dr. J. Hufenbach, Dr. D. Beitelschmidt, Dr. B. Sarac, Dr. C. Soyarslan, D. Lohse, Dr. N. Barekar, Dr. H. Attar, E. Saei Ghareh Naz, F. Ebert, B. Opitz, Dr. J. H. Han, A. Funk, Dr. A. Health, J. Sander, T. Gustmann, J. Zeisig, Dr. J. Wright and Prof. J. Kruzic.

The support from ESRF through the project No. HD/613 ID11, the German Science Foundation (DFG) under the Leibniz Program (grant EC 111/26-1) and Grant PA 2275/2-1, and the European Research Council under the ERC Advanced Grant INTELHYB (grant ERC-2013-ADG-340025) is also gratefully acknowledged.

Finally, I am extremely grateful for the love provided by my family members along with their constant support and care without which this task might have never been done. In particular, I would like to express my heartfelt thanks to my lovely wife, Dr. Zahra Eskandari. During the last years she tolerated long distance relationship and patiently motivated me with her good wishes and kind helps.

Bibliography

1. Greer, A.L., Y.Q. Cheng, and E. Ma, *Shear bands in metallic glasses*. Materials Science & Engineering R-Reports, 2013. **74**(4): p. 71-132.
2. Egelstaff, P.A., *New experimental studies of the structure of fluids*. Advances in Chemical Physics, 1983. **53**: p. 1-60.
3. Marr, G.V., *Handbook on Synchrotron Radiation* Vol. 2. 1987: Elsevier Science Pub. Co. Inc.
4. *Neutrons and Synchrotron Radiation in Engineering Materials Science: From Fundamentals to Material and Component Characterization*. 2008: Wiley-VCH Verlag GmbH & Co.
5. Poulsen, H.F., et al., *Measuring strain distributions in amorphous materials*. Nature Materials, 2005. **4**(1): p. 33-36.
6. Stoica, M., et al., *Strain distribution in $Zr_{64.13}Cu_{15.75}Ni_{10.12}Al_{10}$ bulk metallic glass investigated by in situ tensile tests under synchrotron radiation*. Journal of Applied Physics, 2008. **104**(1).
7. Wang, G., et al., *Atomic structure evolution in bulk metallic glass under compressive stress*. Applied Physics Letters, 2009. **95**(25).
8. Bednarcik, J., et al., *Mapping the Strain Distributions in Deformed Bulk Metallic Glasses Using Hard X-Ray Diffraction*. Metallurgical and Materials Transactions a-Physical Metallurgy and Materials Science, 2012. **43A**(5): p. 1558-1563.
9. Scudino, S., et al., *Ductile bulk metallic glasses produced through designed heterogeneities*. Scripta Materialia, 2011. **65**(9): p. 815-818.
10. Scudino, S., et al., *Effect of cold rolling on compressive and tensile mechanical properties of $Zr_{52.5}Ti_5Cu_{18}Ni_{14.5}Al_{10}$ bulk metallic glass*. Journal of Alloys and Compounds, 2011. **509**: p. S128-S130.
11. Wang, L., et al., *Effect of residual stresses on the onset of yielding in a Zr-based metallic glass*. Acta Materialia, 2011. **59**(20): p. 7627-7633.
12. Lee, M.H., et al., *Improved plasticity of bulk metallic glasses upon cold rolling*. Scripta Materialia, 2010. **62**(9): p. 678-681.
13. Yu, H.B., et al., *Stress-induced structural inhomogeneity and plasticity of bulk metallic glasses*. Scripta Materialia, 2009. **61**(6): p. 640-643.
14. Cao, Q.P., et al., *Effect of pre-existing shear bands on the tensile mechanical properties of a bulk metallic glass*. Acta Materialia, 2010. **58**(4): p. 1276-1292.
15. Shahabi, H.S., et al., *Metallic glass-steel composite with improved compressive plasticity*. Materials & Design, 2014. **59**: p. 241-245.
16. Tong, Y., et al., *Residual elastic strain induced by equal channel angular pressing on bulk metallic glasses*. Acta Materialia, 2013. **61**(4): p. 1204-1209.

17. Scudino, S., et al., *Improved Room Temperature Plasticity of $Zr_{41.2}Ti_{13.8}Cu_{12.5}Ni_{10}Be_{22.5}$ Bulk Metallic Glass by Channel-Die Compression*. *Advanced Engineering Materials*, 2010. **12**(11): p. 1123-1126.
18. Chen, L.Y., et al., *Stress-induced softening and hardening in a bulk metallic glass*. *Scripta Materialia*, 2008. **59**(11): p. 1210-1213.
19. Wang, L., et al., *Effect of residual stresses on the hardness of bulk metallic glasses*. *Acta Materialia*, 2011. **59**(7): p. 2858-2864.
20. Song, K.K., et al., *Significant tensile ductility induced by cold rolling in $Cu(47.5)Zr(47.5)Al(5)$ bulk metallic glass*. *Intermetallics*, 2011. **19**(10): p. 1394-1398.
21. Scudino, S., et al., *Structural features of plastic deformation in bulk metallic glasses*. *Applied Physics Letters*, 2015. **106**(3): p. 031903
22. Yamanaka, S., K. Amiya, and Y. Saotome, *Effects of residual stress on elastic plastic behavior of metallic glass bolts formed by cold thread rolling*. *Journal of Materials Processing Technology*, 2014. **214**(11): p. 2593-2599.
23. Haag, F., et al., *Influences of residual stresses on the serrated flow in bulk metallic glass under elastostatic four-point bending - A nanoindentation and atomic force microscopy study*. *Acta Materialia*, 2014. **70**: p. 188-197.
24. Wang, Q., et al., *Superior Tensile Ductility in Bulk Metallic Glass with Gradient Amorphous Structure*. *Scientific Reports*, 2014. **4**.
25. Zhang, Y., W.H. Wang, and A.L. Greer, *Making metallic glasses plastic by control of residual stress*. *Nature Materials*, 2006. **5**(11): p. 857-860.
26. Mear, F.O., et al., *Residual-stress distribution in shot-peened metallic-glass plate*. *Philosophical Magazine Letters*, 2008. **88**(11): p. 757-766.
27. Hufnagel, T.C., U.K. Vempati, and J.D. Almer, *Crack-Tip Strain Field Mapping and the Toughness of Metallic Glasses*. *Plos One*, 2013. **8**(12).
28. Yavari, A.R., et al., *Excess free volume in metallic glasses measured by X-ray diffraction*. *Acta Materialia*, 2005. **53**(6): p. 1611-1619.
29. Stolpe, M., J.J. Kruzic, and R. Busch, *Evolution of shear bands, free volume and hardness during cold rolling of a Zr-based bulk metallic glass*. *Acta Materialia*, 2014. **64**: p. 231-240.
30. Pan, J., et al., *Softening and dilatation in a single shear band*. *Acta Materialia*, 2011. **59**(13): p. 5146-5158.
31. Maaß, R., et al., *A single shear band in a metallic glass: Local core and wide soft zone*. *Applied Physics Letters*, 2014. **105**(17): p. -.

32. Cheng, Y.Q. and E. Ma, *Atomic-level structure and structure-property relationship in metallic glasses*. Progress in Materials Science, 2011. **56**(4): p. 379-473.
33. Klement, W., R.H. Willens, and P. Duwez, *Non-crystalline structure in solidified gold-silicon alloys*. Nature, 1960. **187**(4740): p. 869-870.
34. Inoue, A., *Stabilization of metallic supercooled liquid and bulk amorphous alloys*. Acta Materialia, 2000. **48**(1): p. 279-306.
35. Bernal, J.D., *Geometry of the structure of monatomic liquids*. Nature, 1960. **185**(4706): p. 68-70.
36. Hirata, A., et al., *Geometric Frustration of Icosahedron in Metallic Glasses*. Science, 2013. **341**(6144): p. 376-379.
37. Miracle, D.B., *A structural model for metallic glasses*. Nature Materials, 2004. **3**(10): p. 697-702.
38. Miracle, D.B., W.S. Sanders, and O.N. Senkov, *The influence of efficient atomic packing on the constitution of metallic glasses*. Philosophical Magazine, 2003. **83**(20): p. 2409-2428.
39. Miracle, D.B., *The efficient cluster packing model - An atomic structural model for metallic glasses*. Acta Materialia, 2006. **54**(16): p. 4317-4336.
40. Mayr, S.G., *Relaxation kinetics and mechanical stability of metallic glasses and supercooled melts*. Physical Review B, 2009. **79**(6).
41. Tsamados, M., et al., *Local elasticity map and plasticity in a model Lennard-Jones glass*. Physical Review E, 2009. **80**(2).
42. Ichitsubo, T., et al., *Nanoscale elastic inhomogeneity of a Pd-based metallic glass: Sound velocity from ultrasonic and inelastic x-ray scattering experiments*. Physical Review B, 2007. **76**(14).
43. Demetriou, M.D., W.L. Johnson, and K. Samwer, *Coarse-grained description of localized inelastic deformation in amorphous metals*. Applied Physics Letters, 2009. **94**(19).
44. Suryanarayana, C. and A. Inoue, *Bulk Metallic Glasses*. 2011, CRC Press (Taylor & Francis Group).
45. Trexler, M.M. and N.N. Thadhani, *Mechanical properties of bulk metallic glasses*. Progress in Materials Science, 2010. **55**(8): p. 759-839.
46. Eckert, J., et al., *Mechanical properties of bulk metallic glasses and composites*. Journal of Materials Research, 2007. **22**(2): p. 285-301.
47. Zhao, J.X., et al., *Fracture mechanism of some brittle metallic glasses*. Journal of Applied Physics, 2009. **105**(10).
48. Schroers, J. and W.L. Johnson, *Ductile bulk metallic glass*. Physical Review Letters, 2004. **93**(25).

49. Chen, M.W., *Mechanical behavior of metallic glasses: Microscopic understanding of strength and ductility*. Annual Review of Materials Research, 2008. **38**: p. 445-469.
50. Cohen, M.H. and D. Turnbull, *Molecular transport in liquids and glasses*. Journal of Chemical Physics, 1959. **31**(5): p. 1164-1169.
51. Turnbull, D. and M.H. Cohen, *Free-volume model of amorphous phase-glass transition*. Journal of Chemical Physics, 1961. **34**(1): p. 120-&.
52. Turnbull, D. and M.H. Cohen, *On free-volume model of liquid-glass transition*. Journal of Chemical Physics, 1970. **52**(6): p. 3038-&.
53. Spaepen, F., *Microscopic mechanism for steady-state inhomogeneous flow in metallic glasses*. Acta Metallurgica, 1977. **25**(4): p. 407-415.
54. Argon, A.S., *Plastic deformation in metallic glasses*. Acta Metallurgica, 1979. **27**(1): p. 47-58.
55. Gilman, J.J., *Mechanical behavior of metallic glasses*. Journal of Applied Physics, 1975. **46**(4): p. 1625-1633.
56. Spaepen, F., *Metallic glasses: Must shear bands be hot?* Nature Materials, 2006. **5**(1): p. 7-8.
57. Chen, H.S. and S.Y. Chuang, *Structure study of a metallic glass using positron-annihilation methods*. Journal of Electronic Materials, 1975. **4**(5): p. 783-789.
58. Kanungo, B.P., et al., *Characterization of free volume changes associated with shear band formation in Zr- and Cu-based bulk metallic glasses*. Intermetallics, 2004. **12**(10-11): p. 1073-1080.
59. Flores, K.M., et al., *Sub-nanometer open volume regions in a bulk metallic glass investigated by positron annihilation*. Acta Materialia, 2007. **55**(10): p. 3403-3411.
60. Flores, K.M., et al., *Characterization of plasticity-induced structural changes in a Zr-based bulk metallic glass using positron annihilation spectroscopy*. Journal of Non-Crystalline Solids, 2007. **353**(11-12): p. 1201-1207.
61. Argon, A.S. and H.Y. Kuo, *Free-energy spectra for inelastic deformation of 5 metallic glass alloys*. Journal of Non-Crystalline Solids, 1980. **37**(2): p. 241-266.
62. Eshelby, J.D., *The determination of the elastic field of an ellipsoidal inclusion, and related problems*. Proceedings of the Royal Society of London Series a-Mathematical and Physical Sciences, 1957. **241**(1226): p. 376-396.
63. Argon, A.S., *Mechanisms of inelastic deformation in metallic glasses*. Journal of Physics and Chemistry of Solids, 1982. **43**(10): p. 945-961.
64. Argon, A.S. and L.T. Shi, *Development of visco-plastic deformation in metallic glasses*. Acta Metallurgica, 1983. **31**(4): p. 499-507.

65. Li, M., et al., *Structural heterogeneity and medium-range order in Zr_xCu_{100-x} metallic glasses*. Physical Review B, 2009. **80**(18).
66. Schuh, C.A. and A.C. Lund, *Atomistic basis for the plastic yield criterion of metallic glass*. Nature Materials, 2003. **2**(7): p. 449-452.
67. Wakeda, M., et al., *Relationship between local geometrical factors and mechanical properties for Cu-Zr amorphous alloys*. Intermetallics, 2007. **15**(2): p. 139-144.
68. Delogu, F., *Identification and characterization of potential shear transformation zones in metallic glasses*. Physical Review Letters, 2008. **100**(25).
69. Srolovitz, D., V. Vitek, and T. Egami, *An atomistic study of deformation of amorphous metals*. Acta Metallurgica, 1983. **31**(2): p. 335-352.
70. Cheng, Y.Q., et al., *Local order influences initiation of plastic flow in metallic glass: Effects of alloy composition and sample cooling history*. Acta Materialia, 2008. **56**(18): p. 5263-5275.
71. Shimizu, F., S. Ogata, and J. Li, *Yield point of metallic glass*. Acta Materialia, 2006. **54**(16): p. 4293-4298.
72. Falk, M.L. and J.S. Langer, *Dynamics of viscoplastic deformation in amorphous solids*. Physical Review E, 1998. **57**(6): p. 7192-7205.
73. Langer, J.S., *Shear-transformation-zone theory of deformation in metallic glasses*. Scripta Materialia, 2006. **54**(3): p. 375-379.
74. Johnson, W.L. and K. Samwer, *A universal criterion for plastic yielding of metallic glasses with a $(T/T_g)^{(2/3)}$ temperature dependence*. Physical Review Letters, 2005. **95**(19).
75. Mayr, S.G., *Activation energy of shear transformation zones: A key for understanding rheology of glasses and liquids*. Physical Review Letters, 2006. **97**(19).
76. Zink, M., et al., *Plastic deformation of metallic glasses: Size of shear transformation zones from molecular dynamics simulations*. Physical Review B, 2006. **73**(17).
77. Pan, D., et al., *Experimental characterization of shear transformation zones for plastic flow of bulk metallic glasses*. Proceedings of the National Academy of Sciences of the United States of America, 2008. **105**(39): p. 14769-14772.
78. Pan, D., et al., *Correlation between structural relaxation and shear transformation zone volume of a bulk metallic glass*. Applied Physics Letters, 2009. **95**(14).
79. Schuh, C.A., T.C. Hufnagel, and U. Ramamurty, *Mechanical behavior of amorphous alloys*. Acta Materialia, 2007. **55**(12): p. 4067-4109.

80. Bei, H., S. Xie, and E.P. George, *Softening caused by profuse shear banding in a bulk metallic glass*. Physical Review Letters, 2006. **96**(10).
81. Lewandowski, J.J. and A.L. Greer, *Temperature rise at shear bands in metallic glasses*. Nature Materials, 2006. **5**(1): p. 15-18.
82. Pekarskaya, E., C.P. Kim, and W.L. Johnson, *In situ transmission electron microscopy studies of shear bands in a bulk metallic glass based composite*. Journal of Materials Research, 2001. **16**(9): p. 2513-2518.
83. Zhang, Y. and A.L. Greer, *Thickness of shear bands in metallic glasses*. Applied Physics Letters, 2006. **89**(7).
84. Li, J., F. Spaepen, and T.C. Hufnagel, *Nanometre-scale defects in shear bands in a metallic glass*. Philosophical Magazine a-Physics of Condensed Matter Structure Defects and Mechanical Properties, 2002. **82**(13): p. 2623-2630.
85. Wright, W.J., T.C. Hufnagel, and W.D. Nix, *Free volume coalescence and void formation in shear bands in metallic glass*. Journal of Applied Physics, 2003. **93**(3): p. 1432-1437.
86. Hufnagel, T.C., et al., *Controlling shear band behavior in metallic glasses through microstructural design*. Intermetallics, 2002. **10**(11-12): p. 1163-1166.
87. Hufnagel, T.C., P. El-Deiry, and R.P. Vinci, *Development of shear band structure during deformation of a $Zr_{57}Ti_5Cu_{20}Ni_8Al_{10}$ bulk metallic glass*. Scripta Materialia, 2000. **43**(12): p. 1071-1075.
88. Yang, Y. and C.T. Liu, *Size effect on stability of shear-band propagation in bulk metallic glasses: an overview*. Journal of Materials Science, 2012. **47**(1): p. 55-67.
89. Harmon, J.S., et al., *Anelastic to plastic transition in metallic glass-forming liquids*. Physical Review Letters, 2007. **99**(13).
90. Yang, B., et al., *Dynamic evolution of nanoscale shear bands in a bulk-metallic glass*. Applied Physics Letters, 2005. **86**(14).
91. Yang, B., et al., *Localized heating and fracture criterion for bulk metallic glasses*. Journal of Materials Research, 2006. **21**(4): p. 915-922.
92. Dai, L.H., *Shear Banding in Bulk Metallic Glasses*, in *Adiabatic Shear Localization*. 2012, Hardbound.
93. Cheng, Y.Q., et al., *Cold versus hot shear banding in bulk metallic glass*. Physical Review B, 2009. **80**(13).
94. Cao, A.J., Y.Q. Cheng, and E. Ma, *Structural processes that initiate shear localization in metallic glass*. Acta Materialia, 2009. **57**(17): p. 5146-5155.

95. Pampillo, C.A., *Localized shear deformation in a glassy metal*. Scripta Metallurgica, 1972. **6**(10): p. 915-918.
96. Chen, H.S., H.J. Leamy, and M.J. O'Brien, *Bending deformation in metallic glasses*. Scripta Metallurgica, 1973. **7**(4): p. 415-419.
97. Pampillo, C.A. and H.S. Chen, *Comprehensive plastic-deformation of a bulk metallic glass*. Materials Science and Engineering, 1974. **13**(2): p. 181-188.
98. Polk, D.E. and D. Turnbull, *Flow of melt and glass forms of metallic alloys*. Acta Metallurgica, 1972. **20**(4): p. 493-498.
99. Packard, C.E. and C.A. Schuh, *Initiation of shear bands near a stress concentration in metallic glass*. Acta Materialia, 2007. **55**(16): p. 5348-5358.
100. Song, S.X., X.L. Wang, and T.G. Nieh, *Capturing shear band propagation in a Zr-based metallic glass using a high-speed camera*. Scripta Materialia, 2010. **62**(11): p. 847-850.
101. Han, Z. and Y. Li, *Cooperative shear and catastrophic fracture of bulk metallic glasses from a shear-band instability perspective*. Journal of Materials Research, 2009. **24**(12): p. 3620-3627.
102. Bruck, H.A., et al., *Quasi-static constitutive behavior of $Zr_{41.25}Ti_{13.75}Ni_{10}Cu_{12.5}Be_{22.5}$ bulk amorphous-alloys*. Scripta Metallurgica Et Materialia, 1994. **30**(4): p. 429-434.
103. Liu, C.T., et al., *Test environments and mechanical properties of Zr-base bulk amorphous alloys*. Metallurgical and Materials Transactions a-Physical Metallurgy and Materials Science, 1998. **29**(7): p. 1811-1820.
104. Gilbert, C.J., et al., *Light emission during fracture of a Zr-Ti-Ni-Cu-Be bulk metallic glass*. Applied Physics Letters, 1999. **74**(25): p. 3809-3811.
105. Yavari, A.R., J.J. Lewandowski, and J. Eckert, *Mechanical properties of bulk metallic glasses*. Mrs Bulletin, 2007. **32**(8): p. 635-638.
106. Hajlaoui, K., et al., *Shear delocalization and crack blunting of a metallic glass containing nanoparticles: In situ deformation in TEM analysis*. Scripta Materialia, 2006. **54**(11): p. 1829-1834.
107. Hajlaoui, K., et al., *Unusual room temperature ductility of glassy copper-zirconium caused by nanoparticle dispersions that grow during shear*. Materials Science and Engineering a-Structural Materials Properties Microstructure and Processing, 2007. **449**: p. 105-110.
108. Qiao, J.W., et al., *Low-temperature shear banding for a Cu-based bulk-metallic glass*. Scripta Materialia, 2010. **63**(8): p. 871-874.
109. Zhang, L.C., et al., *Stable shear of $Cu_{46}Zr_{47}Al_7$ bulk metallic glass alloy by controlling temperature rise*. Materials Science and

- Engineering a-Structural Materials Properties Microstructure and Processing, 2010. **527**(16-17): p. 4122-4127.
110. Flores, K.M. and R.H. Dauskardt, *Local heating associated with crack tip plasticity in Zr-Ti-Ni-Cu-Be bulk amorphous metals*. Journal of Materials Research, 1999. **14**(3): p. 638-643.
 111. Bruck, H.A., A.J. Rosakis, and W.L. Johnson, *The dynamic compressive behavior of beryllium bearing bulk metallic glasses*. Journal of Materials Research, 1996. **11**(2): p. 503-511.
 112. Kim, J.J., et al., *Nanocrystallization during nanoindentation of a bulk amorphous metal alloy at room temperature*. Science, 2002. **295**(5555): p. 654-657.
 113. Wright, W.J., R.B. Schwarz, and W.D. Nix, *Localized heating during serrated plastic flow in bulk metallic glasses*. Materials Science and Engineering a-Structural Materials Properties Microstructure and Processing, 2001. **319**: p. 229-232.
 114. Donovan, P.E., *A yield criterion for Pd₄₀Ni₄₀P₂₀ metallic-glass*. Acta Metallurgica, 1989. **37**(2): p. 445-456.
 115. Yang, B., et al., *In-situ thermographic observation of mechanical damage in bulk-metallic glasses during fatigue and tensile experiments*. Intermetallics, 2004. **12**(10-11): p. 1265-1274.
 116. Jiang, W.H., et al., *Rate-dependent temperature increases in shear bands of a bulk-metallic glass*. Metallurgical and Materials Transactions a-Physical Metallurgy and Materials Science, 2008. **39A**(8): p. 1822-1830.
 117. Donovan, P.E. and W.M. Stobbs, *The structure of shear bands in metallic glasses*. Acta Metallurgica, 1981. **29**(8): p. 1419-1436.
 118. Zhang, Y., et al., *Local temperature rises during mechanical testing of metallic glasses*. Journal of Materials Research, 2007. **22**(2): p. 419-427.
 119. Wright, W.J., et al., *Studies of shear band velocity using spatially and temporally resolved measurements of strain during quasistatic compression of a bulk metallic glass*. Acta Materialia, 2009. **57**(16): p. 4639-4648.
 120. Miracle, D.B., et al., *Shear bands in metallic glasses: Size effects on thermal profiles*. Acta Materialia, 2011. **59**(7): p. 2831-2840.
 121. Georgarakis, K., et al., *Shear band melting and serrated flow in metallic glasses*. Applied Physics Letters, 2008. **93**(3).
 122. Frenkel, J., *Zur Theorie der Elastizitätsgrenze und der Festigkeit kristallinischer Körper*. 1926. **37**(7-8): p. 572-609.
 123. Yang, B., C.T. Liu, and T.G. Nieh, *Unified equation for the strength of bulk metallic glasses*. Applied Physics Letters, 2006. **88**(22).

124. Zhang, Z.F., J. Eckert, and L. Schultz, *Difference in compressive and tensile fracture mechanisms of $Zr_{59}Cu_{20}Al_{10}Ni_8Ti_3$ bulk metallic glass*. Acta Materialia, 2003. **51**(4): p. 1167-1179.
125. He, G., et al., *Fracture morphology and quenched-in precipitates induced embrittlement in a Zr-base bulk glass*. Materials Transactions Jim, 2001. **42**(2): p. 356-364.
126. Lowhaphandu, P., et al., *Deformation and fracture toughness of a bulk amorphous Zr-Ti-Ni-Cu-Be alloy*. Intermetallics, 2000. **8**(5-6): p. 487-492.
127. Qu, R.T., J. Eckert, and Z.F. Zhang, *Tensile fracture criterion of metallic glass*. Journal of Applied Physics, 2011p. **109**(8).
128. Zhang, Z.F. and J. Eckert, *Unified tensile fracture criterion*. Physical Review Letters, 2005p. **94**(9).
129. Qu, R.T. and Z.F. Zhang, *A universal fracture criterion for high-strength materials*. Scientific Reports, 2013. **3**.
130. Zhang, Z.F., et al., *Effect of aspect ratio on the compressive deformation and fracture behaviour of Zr-based bulk metallic glass*. Philosophical Magazine Letters, 2005. **85**(10): p. 513-521.
131. Wu, W.F., Y. Li, and C.A. Schuh, *Strength, plasticity and brittleness of bulk metallic glasses under compression: statistical and geometric effects*. Philosophical Magazine, 2008. **88**(1): p. 71-89.
132. Conner, R.D., et al., *Shear bands and cracking of metallic glass plates in bending*. Journal of Applied Physics, 2003. **94**(2): p. 904-911.
133. Demetriou, M.D., et al., *A damage-tolerant glass*. Nature Materials, 2011. **10**(2): p. 123-128.
134. Ravichandran, G. and A. Molinari, *Analysis of shear banding in metallic glasses under bending*. Acta Materialia, 2005. **53**(15): p. 4087-4095.
135. Bei, H., Z.P. Lu, and E.P. George, *Theoretical strength and the onset of plasticity in bulk metallic glasses investigated by nanoindentation with a spherical indenter*. Physical Review Letters, 2004. **93**(12).
136. Schuh, C.A. and T.G. Nieh, *A survey of instrumented indentation studies on metallic glasses*. Journal of Materials Research, 2004. **19**(1): p. 46-57.
137. Yokoyama, Y., T. Yamasaki, and A. Inoue, *Significant tensile plasticity of cold rolled $Zr_{50}Cu_{30}Ni_{10}Al_{10}$ bulk glassy alloys*. Reviews on Advanced Materials Science, 2008. **18**(2): p. 131-136.
138. Liu, J.W., et al., *Shear band evolution and hardness change in cold-rolled bulk metallic glasses*. Acta Materialia, 2010. **58**(14): p. 4827-4840.

139. Murata, T., T. Masumoto, and M. Sakai. *Slip Deformation and Critical Shear Stress of Amorphous PdSi Alloy*. in *Rapidly Quenched Metals III*. 1978.
140. Han, Z., Y. Li, and H.J. Gao, *Effect of frame stiffness on the deformation behavior of bulk metallic glass*. Journal of Materials Research, 2010. **25**(10): p. 1958-1962.
141. Han, Z., et al., *An instability index of shear band for plasticity in metallic glasses*. Acta Materialia, 2009. **57**(5): p. 1367-1372.
142. Shan, Z.W., et al., *Plastic flow and failure resistance of metallic glass: Insight from in situ compression of nanopillars*. Physical Review B, 2008. **77**(15).
143. Wang, C.C., et al., *Sample size matters for Al₈₈Fe₇Gd₅ metallic glass: Smaller is stronger*. Acta Materialia, 2012. **60**(13-14): p. 5370-5379.
144. Chen, H.S., J.T. Krause, and E. Coleman, *Elastic constants, hardness and their implications to flow properties of metallic glasses*. Journal of Non-Crystalline Solids, 1975. **18**(2): p. 157-171.
145. Pugh, S.F., *Relations between the elastic moduli and the plastic properties of polycrystalline pure metals*. Philosophical Magazine, 1954. **45**(367): p. 823-843.
146. Wei, Y., et al., *Towards more uniform deformation in metallic glasses: The role of Poisson's ratio*. Materials Science and Engineering: A, 2013. **560**(0): p. 510-517.
147. Lewandowski, J.J., W.H. Wang, and A.L. Greer, *Intrinsic plasticity or brittleness of metallic glasses*. Philosophical Magazine Letters, 2005. **85**(2): p. 77-87.
148. Zhang, Y. and A.L. Greer, *Correlations for predicting plasticity or brittleness of metallic glasses*. Journal of Alloys and Compounds, 2007. **434**: p. 2-5.
149. Hofmann, D.C., et al., *Designing metallic glass matrix composites with high toughness and tensile ductility*. Nature, 2008. **451**(7182): p. 1085-U3.
150. Wu, Y.A., et al., *Bulk Metallic Glass Composites with Transformation-Mediated Work-Hardening and Ductility*. Advanced Materials, 2010. **22**(25): p. 2770-+.
151. Song, K.K., et al., *Triple yielding and deformation mechanisms in metastable Cu_{47.5}Zr_{47.5}Al₅ composites*. Acta Materialia, 2012. **60**(17): p. 6000-6012.
152. Lee, K., et al., *Compressive and tensile properties of tungsten-continuous-fiber-reinforced Zr-based amorphous alloy matrix composite fabricated by liquid pressing process*. Metallurgical and Materials Transactions a-Physical Metallurgy and Materials Science, 2008. **39A**(6): p. 1319-1326.

153. Ferry, M., et al., *Recent developments in ductile bulk metallic glass composites*. Mrs Communications, 2013. **3**(1): p. 1-12.
154. Hofmann, D.C., et al., *New processing possibilities for highly toughened metallic glass matrix composites with tensile ductility*. Scripta Materialia, 2008. **59**(7): p. 684-687.
155. Hofmann, D.C., et al., *Development of tough, low-density titanium-based bulk metallic glass matrix composites with tensile ductility*. Proceedings of the National Academy of Sciences of the United States of America, 2008. **105**(51): p. 20136-20140.
156. Szuecs, F., C.P. Kim, and W.L. Johnson, *Mechanical properties of $Zr_{56.2}Ti_{13.8}Nb_{5.0}Cu_{6.9}Ni_{5.6}Be_{12.5}$ ductile phase reinforced bulk metallic glass composite*. Acta Materialia, 2001. **49**(9): p. 1507-1513.
157. Son, C.Y., et al., *Correlation of Microstructure with Mechanical Properties of Zr-Based Amorphous Matrix Composite Reinforced with Tungsten Continuous Fibers and Ductile Dendrites*. Metallurgical and Materials Transactions a-Physical Metallurgy and Materials Science, 2012. **43A**(11): p. 4088-4096.
158. Kim, Y., et al., *Dynamic Deformation Behavior of Zr-Based Amorphous Alloy Matrix Composites Reinforced with STS304 or Tantalum Fibers*. Metallurgical and Materials Transactions a-Physical Metallurgy and Materials Science, 2012. **43A**(9): p. 3023-3033.
159. Scudino, S., et al., *Enhanced plastic deformation of $Zr_{41.2}Ti_{13.8}Cu_{12.5}Ni_{10}Be_{22.5}$ bulk metallic glass by the optimization of frictional boundary restraints*. Scripta Materialia, 2010. **62**(10): p. 750-753.
160. Song, K.K., et al., *Significant tensile ductility induced by cold rolling in $Cu_{47.5}Zr_{47.5}Al_5$ bulk metallic glass*. Intermetallics, 2011. **19**(10): p. 1394-1398.
161. Scudino, S., K.B. Surreddi, and J. Eckert, *Mechanical properties of cold-rolled $Zr_{60}Ti_5Ag_5Cu_{12.5}Ni_{10}Al_{7.5}$ metallic glass*. Physica Status Solidi a-Applications and Materials Science, 2010. **207**(5): p. 1118-1121.
162. Mear, F.O., et al., *Structural effects of shot-peening in bulk metallic glasses*. Journal of Alloys and Compounds, 2009. **483**(1-2): p. 256-259.
163. Tariq, N.H., et al., *Plasticity enhancement in Zr based bulk metallic glass by sand blasting*. Materials Chemistry and Physics, 2011. **126**(1-2): p. 207-211.
164. Chen, B.Q., et al., *Improvement in mechanical properties of a Zr-based bulk metallic glass by laser surface treatment*. Journal of Alloys and Compounds, 2010. **504**: p. S45-S47.

165. Qu, R.T., Q.S. Zhang, and Z.F. Zhang, *Achieving macroscopic tensile plasticity of monolithic bulk metallic glass by surface treatment*. Scripta Materialia, 2013. **68**(11): p. 845-848.
166. Park, K.W., et al., *A methodology of enhancing the plasticity of amorphous alloys: Elastostatic compression at room temperature*. Materials Science and Engineering a-Structural Materials Properties Microstructure and Processing, 2009. **499**(1-2): p. 529-533.
167. Lee, S.C., et al., *Structural disordering process of an amorphous alloy driven by the elastostatic compression at room temperature*. Applied Physics Letters, 2008. **92**(15).
168. Qu, R.T., et al., *Macroscopic tensile plasticity of bulk metallic glass through designed artificial defects*. Materials Science and Engineering a-Structural Materials Properties Microstructure and Processing, 2012. **534**: p. 365-373.
169. Jiang, J.Z., et al., *Origin of nondetectable x-ray diffraction peaks in nanocomposite CuTiZr alloys*. Applied Physics Letters, 2003. **83**(16): p. 3299-3301.
170. Xing, L.Q., et al., *Relation between short-range order and crystallization behavior in Zr-based amorphous alloys*. Applied Physics Letters, 2000. **77**(13): p. 1970-1972.
171. Liss, K.-D., et al., *High-energy X-rays: a tool for advanced bulk investigations in materials science and physics*. Textures and Microstructures, 2003. **35**(3-4): p. 219-252.
172. Miller, M. and P. Liaw, *Bulk Metallic Glasses: An Overview*. 2008, Springer.
173. Hufnagel, T.C., R.T. Ott, and J. Almer, *Structural aspects of elastic deformation of a metallic glass*. Physical Review B, 2006. **73**(6).
174. Ott, R.T., et al., *Synchrotron strain measurements for in situ formed metallic glass matrix composites*, in *Amorphous and Nanocrystalline Metals*, R. Busch, et al., Editors. 2004. p. 361-366.
175. Balch, D.K., E. Ustundag, and D.C. Dunand, *Elasto-plastic load transfer in bulk metallic glass composites containing ductile particles*. Metallurgical and Materials Transactions a-Physical Metallurgy and Materials Science, 2003. **34A**(9): p. 1787-1797.
176. Yavari, A.R., et al., *Quenched-in free volume V_f , deformation-induced free volume, the glass transition T_g and thermal expansion in glassy ZrNbCuNiAl measured by time-resolved diffraction in transmission*, in *Amorphous and Nanocrystalline Metals*, R. Busch, et al., Editors. 2004, Materials Research Society: Warrendale. p. 203-208.
177. Stoica, M., et al., *Mechanical Response of Metallic Glasses: Insights from In-situ High Energy X-ray Diffraction*. Jom, 2010. **62**(2): p. 76-82.

178. Mattern, N., et al., *Structural evolution of Cu-Zr metallic glasses under tension*. Acta Materialia, 2009. **57**(14): p. 4133-4139.
179. Wang, X.D., et al., *Tensile behavior of bulk metallic glasses by in situ x-ray diffraction*. Applied Physics Letters, 2007. **91**(8).
180. Bednarcik, J. and H. Franz, *Deformation of metallic glasses: insight from in-situ high-energy x-ray diffraction*, in *13th International Conference on Rapidly Quenched and Metastable Materials*, L. Schultz, et al., Editors. 2009, Iop Publishing Ltd: Bristol.
181. Huang, Y.J., et al., *In situ study of the evolution of atomic strain of bulk metallic glass and its effects on shear band formation*. Scripta Materialia, 2013. **69**(3): p. 207-210.
182. Das, J., et al., *Plasticity in bulk metallic glasses investigated via the strain distribution*. Physical Review B, 2007. **76**(9).
183. Srolovitz, D., T. Egami, and V. Vitek, *Radial distribution function and structural relaxation in amorphous solids*. Physical Review B, 1981. **24**(12): p. 6936-6944.
184. Egami, T., K. Maeda, and V. Vitek, *Structural defects in amorphous solids - a computer-simulation study*. Philosophical Magazine a-Physics of Condensed Matter Structure Defects and Mechanical Properties, 1980. **41**(6): p. 883-901.
185. Chen, L.Y., et al., *Atomic-scale mechanisms of tension–compression asymmetry in a metallic glass*. Acta Materialia, 2013(0).
186. Wang, X.D., et al., *Local strain behavior of bulk metallic glasses under tension studied by in situ x-ray diffraction*. Applied Physics Letters, 2009. **94**(1).
187. Wilson, T., et al., *In-situ neutron scattering measurement of stress-strain behavior of a bulk metallic glass*. Metallurgical and Materials Transactions a-Physical Metallurgy and Materials Science, 2008. **39A**(8): p. 1942-1946.
188. Vempati, U.K., et al., *Length-scale dependence of elastic strain from scattering measurements in metallic glasses*. Physical Review B, 2012. **85**(21): p. 214201.
189. Suzuki, Y., J. Haimovich, and T. Egami, *Bond-orientational anisotropy in metallic glasses observed by x-ray-diffraction*. Physical Review B, 1987. **35**(5): p. 2162-2168.
190. Dmowski, W. and T. Egami, *Observation of structural anisotropy in metallic glasses induced by mechanical deformation*. Journal of Materials Research, 2007. **22**(2): p. 412-418.
191. Yan, X., T. Egami, and E.E. Marinero, *bond-orientational anisotropy and anelastic deformation in sputter-deposited amorphous TBFECO films*. Journal of Applied Physics, 1991. **69**(8): p. 5448-5450.

192. Yan, X., et al., *Direct observation of anelastic bond-orientational anisotropy in amorphous Tb₂₆Fe₆₂Co₁₂ thin-films by X-ray-diffraction*. Physical Review B, 1991. **43**(11): p. 9300-9303.
193. Egami, T., et al., *deformation-induced bond-orientational order in metallic glasses*. Journal of Non-Crystalline Solids, 1995. **193**: p. 591-594.
194. Ma, D., A.D. Stoica, and X.L. Wang, *Power-law scaling and fractal nature of medium-range order in metallic glasses*. Nature Materials, 2009. **8**(1): p. 30-34.
195. Wang, G., et al., *Correlation between elastic structural behavior and yield strength of metallic glasses*. Acta Materialia, 2012. **60**(6-7): p. 3074-3083.
196. Qu, D.D., et al., *Structural origins for the high plasticity of a Zr-Cu-Ni-Al bulk metallic glass*. Acta Materialia, 2013. **61**(1): p. 321-330.
197. Oliver, W.C. and G.M. Pharr, *An improved technique for determining hardness and elastic modulus using load and displacement sensing indentation experiments*. Journal of Materials Research, 1992. **7**(06): p. 1564-1583.
198. Hammersley, A.P., et al., *Two-dimensional detector software: From real detector to idealised image or two-theta scan*. High Pressure Research, 1996. **14**(4-6): p. 235-248.
199. Juhas, P., et al., *PDFgetX3: a rapid and highly automatable program for processing powder diffraction data into total scattering pair distribution functions*. Journal of Applied Crystallography, 2013. **46**: p. 560-566.
200. Billinge, S.J.L. and C.L. Farrow, *Towards a robust ad hoc data correction approach that yields reliable atomic pair distribution functions from powder diffraction data*. Journal of Physics-Condensed Matter, 2013. **25**(45).
201. Ellwood Dieter, G., *Mechanical metallurgy*. 1976: McGraw-Hill.
202. Timoshenko, S. and J.M. Gere, *Mechanics of materials*. 1972: Van Nostrand Reinhold Co.
203. Egami, T. and S.J.L. Billinge, *Underneath the Bragg peaks; Structural Analysis of Complex Materials*. 2003: PERGAMON.
204. Saida, J., M. Matsushita, and A. Inoue, *Direct observation of icosahedral cluster in Zr₇₀Pd₃₀ binary glassy alloy*. Applied Physics Letters, 2001. **79**(3): p. 412-414.
205. Hui, X.D., et al., *Atomic structures of Zr-based metallic glasses*. Science in China Series G-Physics Mechanics & Astronomy, 2008. **51**(4): p. 400-413.

206. Ma, D., et al., *Nearest-neighbor coordination and chemical ordering in multicomponent bulk metallic glasses*. Applied Physics Letters, 2007. **90**(21): p. 211908.
207. Cheng, Y.Q., E. Ma, and H.W. Sheng, *Atomic Level Structure in Multicomponent Bulk Metallic Glass*. Physical Review Letters, 2009. **102**(24).
208. Hwang, J., et al., *Nanoscale Structure and Structural Relaxation in $Zr_{50}Cu_{45}Al_5$ Bulk Metallic Glass*. Physical Review Letters, 2012. **108**(19).
209. Mattern, N., et al., *Short-range order of $Zr_{62-x}Ti_xAl_{10}Cu_{20}Ni_8$ bulk metallic glasses*. Acta Materialia, 2002. **50**(2): p. 305-314.
210. Hufnagel, T.C., R.T. Ott, and J. Almer, *Structural aspects of elastic deformation of a metallic glass*. Physical Review B, 2006. **73**(6): p. 064204.
211. Peter, W.H., et al., *Fatigue behavior of $Zr_{52.5}Al_{10}Ti_5Cu_{17.9}Ni_{14.6}$ bulk metallic glass*. Intermetallics, 2002. **10**(11-12): p. 1125-1129.
212. Cullity, B.D., *Elements of X-ray Diffraction*. 1956: ADDISON-WESLEY.
213. Das, J., et al., *Plasticity in bulk metallic glasses investigated via the strain distribution*. Physical Review B, 2007. **76**(9): p. 092203.
214. Ma, D., et al., *Elastic Moduli Inheritance and the Weakest Link in Bulk Metallic Glasses*. Physical Review Letters, 2012. **108**(8): p. 085501.
215. Zhang, Z.Y., et al., *Elastic properties of Zr-based bulk metallic glasses studied by resonant ultrasound spectroscopy*. Journal of Materials Research, 2007. **22**(2): p. 364-367.
216. Delogu, F., *Identification and characterization of potential shear transformation zones in metallic glasses*. Physical Review Letters, 2008. **100**(25): p. 255901.
217. Choi, I.-C., et al., *Estimation of the shear transformation zone size in a bulk metallic glass through statistical analysis of the first pop-in stresses during spherical nanoindentation*. Scripta Materialia, 2012. **66**(11): p. 923-926.
218. Johnson, W.L. and K. Samwer, *A universal criterion for plastic yielding of metallic glasses with a $(T/T_g)^{(2/3)}$ temperature dependence*. Physical Review Letters, 2005. **95**(19): p. 195501.
219. Zhang, Z.F., et al., *Fracture mechanisms in bulk metallic glassy materials*. Physical Review Letters, 2003. **91**(4): p. 045505.
220. Schuh, C.A., A.C. Lund, and T.G. Nieh, *New regime of homogeneous flow in the deformation map of metallic glasses: elevated temperature nanoindentation experiments and mechanistic modeling*. Acta Materialia, 2004. **52**(20): p. 5879-5891.

221. Xie, S. and E.P. George, *Hardness and shear band evolution in bulk metallic glasses after plastic deformation and annealing*. Acta Materialia, 2008. **56**(18): p. 5202-5213.
222. Sarac, B. and J. Schroers, *Designing tensile ductility in metallic glasses*. Nat Commun, 2013. **4**.
223. Askeland, D., P. Fulay, and W. Wright, *The science and engineering of materials*. sixth edition ed. 2010: Cengage Learning, Inc.
224. Ketov, S.V. and D.V. Louzguine-Luzgin, *Localized shear deformation and softening of bulk metallic glass: stress or temperature driven?* Scientific Reports, 2013. **3**.
225. James, R. and R. W. James, *Optical Principles of the Diffraction of X-Rays*. 1948: Macmillan.
226. Warren, B.E., *X-ray Diffraction*. 1990, New York: Dover Publications Inc.
227. Shahabi, H.S., et al., *Structural aspects of elasto-plastic deformation of a Zr-based bulk metallic glass under uniaxial compression*. Acta Materialia, 2015. **95**: p. 30-36.
228. Feng, S., et al., *Atomic structure of shear bands in $\text{Cu}_{64}\text{Zr}_{36}$ metallic glasses studied by molecular dynamics simulations*. Acta Materialia, 2015. **95**(0): p. 236-243.